ACCELERATED KINETICS AND MECHANISM OF GROWTH OF BORIDE LAYERS ON TITANIUM UNDER ISOTHERMAL AND CYCLIC DIFFUSION

by

Biplab Sarma

A dissertation submitted to the faculty of
The University of Utah
in partial fulfillment of the requirements for the degree of

Doctor of Philosophy

Department of Metallurgical Engineering

University of Utah

May 2011

The University of Utah Graduate School

STATEMENT OF DISSERTATION APPROVAL

The dissertation of **Biplab Sarma**

has been approved by the following supervisory committee members:

Ravi Chandran	, Chair	**1/7/2011** Date Approved
Sivaraman Guruswamy	, Member	**1/7/2011** Date Approved
Zhigang Zak Fang	, Member	**1/7/2011** Date Approved
Michael L. Free	, Member	**1/7/2011** Date Approved
Anthony Sanders	, Member	**1/7/2011** Date Approved

and by **Jan D. Miller** , Chair of the Department of **Metallurgical Engineering**

and by Charles A. Wight, Dean of The Graduate School.

ABSTRACT

The tendency of titanium (Ti) and its alloys to wear, gall and seize during high contact stresses between sliding surfaces severely limits their applications in bearings, gears etc. One way to mitigate these problems is to modify their surfaces by applying hard and wear resistant surface coatings. Boriding, which involves solid state diffusion of boron (B) into Ti, thereby forming hard surface layers consisting of TiB_2 and TiB compounds has been shown to produce extremely high wear resistant surfaces in Ti and its alloys. The growth kinetics of these layers are, however, limited by the low diffusivities of B in the high melting TiB_2 and TiB compounds.

On the basis of the fact that HCP metals such as Ti show enhanced (anomalous) self-diffusion near the phase transition temperature, the first hypothesis of this work has been that the diffusivity enhancement should cause rapid ingress of B atoms, thereby accelerating the growth of the hard boride layers. Isothermal boriding experiments were performed close to phase transition temperature (890, 910, and 915˚C) for time periods ranging from 3 to 24 hours. It was found that indeed a much deeper growth of TiB into the Ti substrate (~75 μm) occurred at temperatures very close to the transition temperature (910˚C), compared to that obtained at 1050˚C. A diffusion model based on error-function solutions of Fick's second law was developed to quantitatively illustrate the combined effects of the normal B diffusion in the TiB phase and the anomalous B diffusion in Ti phase in accelerating TiB layer growth. Furthermore, isothermal boriding

experiments close to transition temperature (900˚C) for a period of 71 hours resulted in coating thickness well above 100 μm, while at 1050˚C, the layer growth saturated after about 24 hours of treatment time.

In the second part of this work, a novel approach named "cyclic-phase-change-diffusion, (CPCD)," to create deeper TiB_2 and TiB coating layers on CP-Ti by cyclic thermal processing, has been investigated. It was found that thermal cyclic B diffusion in Ti across the alpha(α)-beta(β) phase transition temperature led to highly hardened surface layers enriched with TiB whiskers that grow to depths exceeding 120 μm. By solving the transient heat transport problem for cyclic changes in surface temperatures, it was found that there is a "heat-packet" that travels back and forth from the surface to the interior of the material. This heat-packet appears to transport B dissolved in β-Ti into interior causing increased coating depths.

CONTENTS

LIST OF TABLES

LIST OF FIGURES

No. **Page**

No. **Page**

No. **Page**

No. **Page**

ACKNOWLEDGMENTS

I would like to express my sincere gratitude towards Dr. K.S. Ravi Chandran for providing me an opportunity to work on this project and for his patient instruction and guidance and in aiding me to grow as a researcher and a writer. I am also grateful to Mr. Anthony Sanders for his advice, help and useful discussions during the course of the work.

I am also thankful to Dr. Zhigang Z. Fang, Dr. Michael L. Free and Dr. Sivaraman Guruswamy for serving on my supervisory committee. Special thanks should be given to my friend and colleague Dr. Nishant Tikekar for useful discussions and training me with various equipments in the initial phase of my work. My lab mates, Curtis Lee, Shawn Madtha, Madhu and Paul Chang also deserve a special mention for their constant help in my work. I would also like to thank Karen Haynes and Kay Argyle for administrative support. This work was completed under the financial support provided by the National Science Foundation and Ortho Development Corporation.

Finally, I am extremely grateful to my parents for their continued faith in my abilities and all forms of support, of which I have been the fortunate recipient throughout my life.

CHAPTER 1

INTRODUCTION

1.1 Background

Surface modification techniques are commonly employed to engineering components to enhance surface properties such as hardness, wear resistance, oxidation and corrosion resistance. Many engineering materials are coated to improve their performance in mechanical and biomedical applications.[1, 2] By appropriate coating processes, surface properties can be modified to suit a given application while preserving the properties of the core. Coating concepts such as high conductive coating for electrical applications, noncorrosive coatings for corrosion resistance, and wear resistance coating to resist abrasion are now common.[3-7]

Diffusion surface hardening of metals has emerged as one of the commonly used techniques to create a hard surface layer on metals like steel, aluminum etc.[8-11] This is performed by the diffusion of elements such as carbon, nitrogen, oxygen, chromium, aluminum, or boron, and the respective processes are termed as carburizing, nitriding, oxidizing, chromizing, aluminizing, and boronizing/boriding. The substrate to be hardened is surrounded by a source containing the element to be diffused and heated to high temperature (generally > 0.5 T_m of the substrate). The coating thickness obtained is generally determined by diffusivity of the element in the substrate at that temperature.

Titanium (Ti) and its alloys have been used extensively in aerospace, chemical and biomedical industries owing to its low density, high stiffness, and excellent corrosion/oxidation resistance. However, its performance in mechanical/contact applications involving wear is poor because of its low strength, low thermal conductivity and high work hardening rate. One way to improve its wear resistance is by the application of a wear resistant coating.[12-13] Physical vapor deposition (PVD)[14], chemical vapor deposition (CVD)[15], ion implantation[16] and laser and electron beam treatments[17] are some of the techniques that have been pursued to increase the wear resistance of titanium and its alloys. However, the coating thicknesses obtained by these above mentioned processes are relatively small. For example, titanium nitride (TiN) coatings deposited by PVD are about 10μm thick and hence it is difficult to use in heavy duty applications such as gears, ball bearings, cams and orthopedic implants.[18] Given that these applications are demanding and that PVD/CVD processes are expensive, there is a general need to develop simpler and more cost effective coating processes.

Diffusion-based processes such as carburizing of steel and nitriding of titanium are relatively more attractive because of the process simplicity, low cost, and applicability to complex component shapes. Phase diagrams of different titanium systems such as Ti-C, Ti-N, Ti-O and Ti-B reveal that hard compounds like TiC, TiN, TiO_2 and TiB_2 can be formed on the surface of titanium by high temperature diffusion. Among these, Ti-B system is very attractive because of the possibility to form a double layer of titanium diboride (TiB_2) and titanium monoboride (TiB).[19] Different techniques can be employed for boriding titanium, but solid state boriding, also known as pack boriding, is one of the simplest and most cost effective methods. In our laboratory, pack boriding of

titanium and its alloys have been studied extensively and boride coating layer of about 50 μm have been obtained on the surface of Ti.[20] In most component finishing and polishing processes after surface treatment, a substantial amount of the hardened surface layer needs to be removed to provide a good surface finish. This necessitates coating depths in excess of 50 μm such that a significant amount of the hardened layer is left to protect the substrate after finishing. New methods that can provide deeper boride layers need to be developed.

A unique characteristic of Group IV HCP transition metals like titanium is that they show anomalous diffusion characteristics near the phase transition temperature.[21, 22] The phase transition involves transformation from low temperature closed packed hexagonal (HCP) phase to high temperature body centered cubic (BCC) phase. In these metals, near the phase transition temperature, the self diffusivities are anomalous in the sense that they are relatively higher than at other temperatures and thus do not conform to the usual descriptions based on Arrhenius law of diffusion. The Arrhenius plots for these metals are characterized by an upward curvature near the phase transition, although the degree of this curvature or deviation seems to vary between metals.

On this basis that Ti shows enhanced (anomalous) self-diffusion near the phase transition temperature, one of the hypotheses of this work is that the diffusivity enhancement should cause rapid ingress of B atoms into Ti, thereby accelerating the growth kinetics of the hard boride surface layers. A theoretical model based on error-function solutions of Fick's second law of diffusion needs to be developed to quantitatively illustrate the combined effects of the normal B diffusion in the TiB phase and the anomalous B diffusion in Ti phase in accelerating TiB layer growth.

The second objective of this research is to demonstrate the feasibility of accelerating the boride layer growth in Ti by the application of a novel process called "cyclic-phase-change-diffusion (CPCD)." The hypothesis is that if reversible phase transformations were induced in titanium surface layers during B diffusion, the transformation could effectively "pump" more B into subsurface layers and can lead to increased coating thickness. This should be encouraged by the low solubility of boron in α phase compared to that in β phase of titanium.[23] Therefore, cyclic thermal boron diffusion across the phase transition temperature and its effectiveness in accelerating the boride coating growth is also investigated in this work.

CHAPTER 2

LITERATURE REVIEW

2.1 Structure and properties of titanium

At room temperature the thermodynamically stable structure of titanium is alpha (α) phase which is HCP as shown in Figure 2.1. The measured lattice parameters *c* and *a* are 0.466 nm and 0.295 nm, respectively, and the c/a ratio (1.59) is a little less than the ideal value for HCP metals (1.66), thus pure titanium has high room temperature ductility.[24] Titanium undergoes polymorphic transformation from HCP (α) phase to BCC (β) phase upon heating through 882.5 °C.[25-26] The high temperature BCC phase of titanium is characterized by the lattice parameter '*a*' (0.332 nm at 900 ˚C).

The structure and properties of titanium and its alloys are significantly influenced by the presence of interstitial elements C, O, N and B. These interstitial elements increase the strength and decrease the ductility of titanium even at low concentrations, as shown in Figure 2.2. The strongest effect on yield strength is caused by the presence of oxygen–an increase in O from 0.18 wt.% to 0.4 wt. % increases the yield strength from about 170 MPa to about 480 MPa. As shown in Figures 2.3-2.5,[27] presence of O, N and C in titanium also increases the α to β phase transition temperature. In particular, a small increase in O and N can impart a noticeable increase in transition temperature,

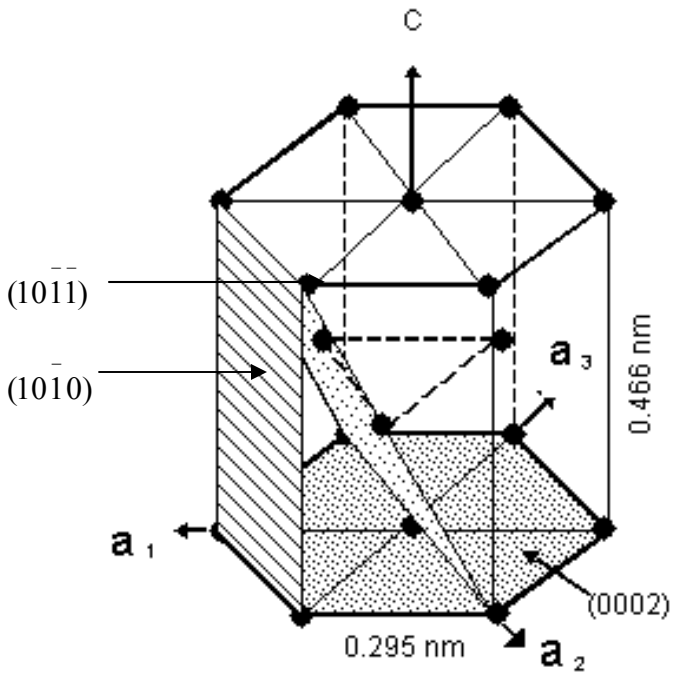

Figure 2.1 HCP crystal structure of Ti

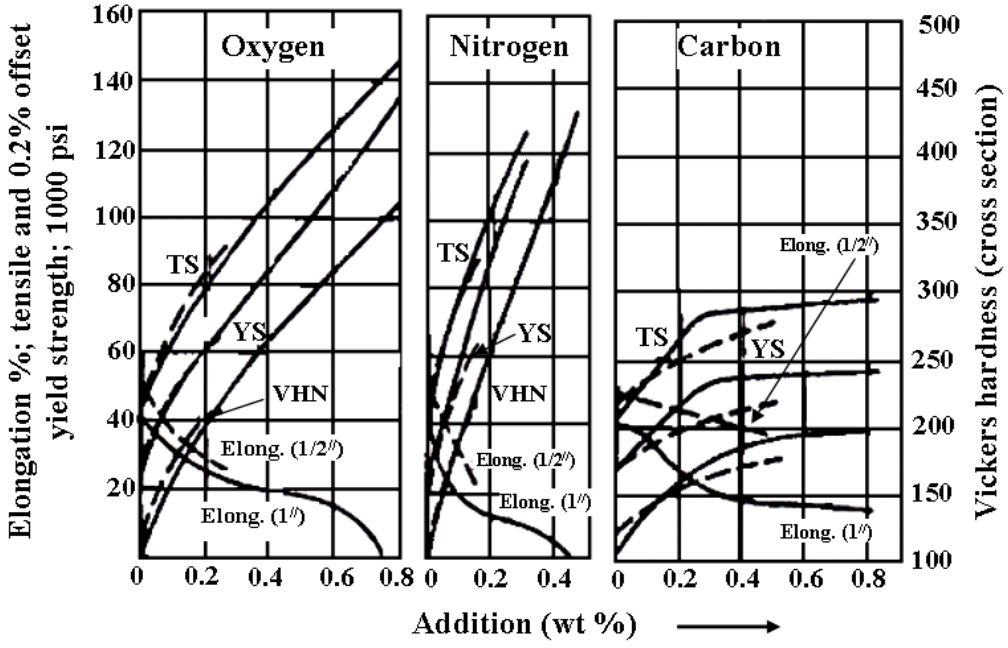

Figure 2.2 Variations in tensile properties of CP-titanium with increasing O, N and C content (Adapted from [27]).

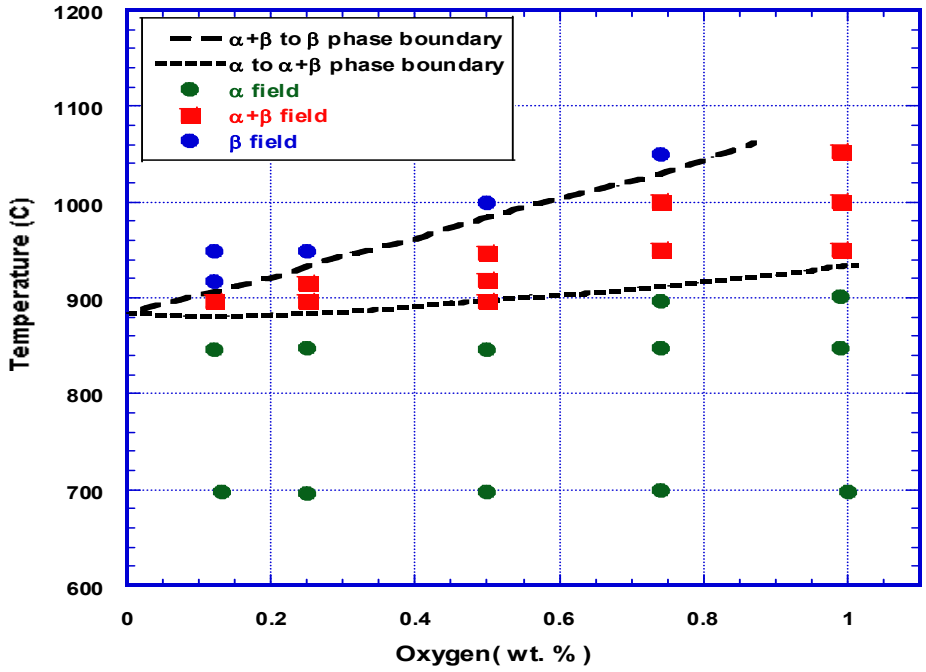

Figure 2.3 The α and β phase fields of Ti as affected by the O content (Adapted from [27])

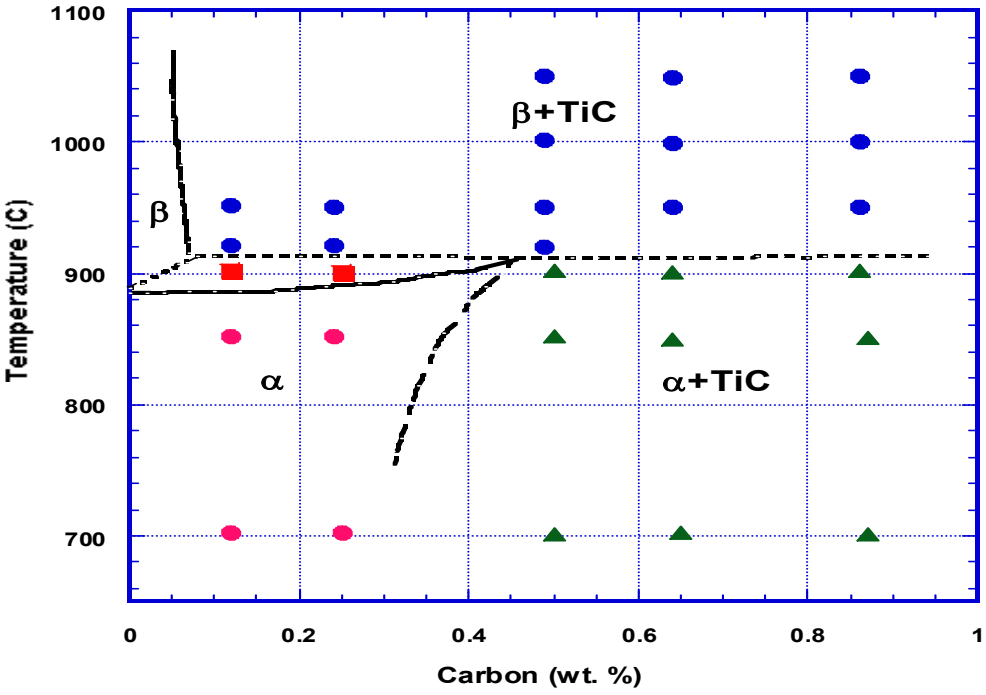

Figure 2.4 The α and β phase fields of Ti as affected by the C content (Adapted from [27])

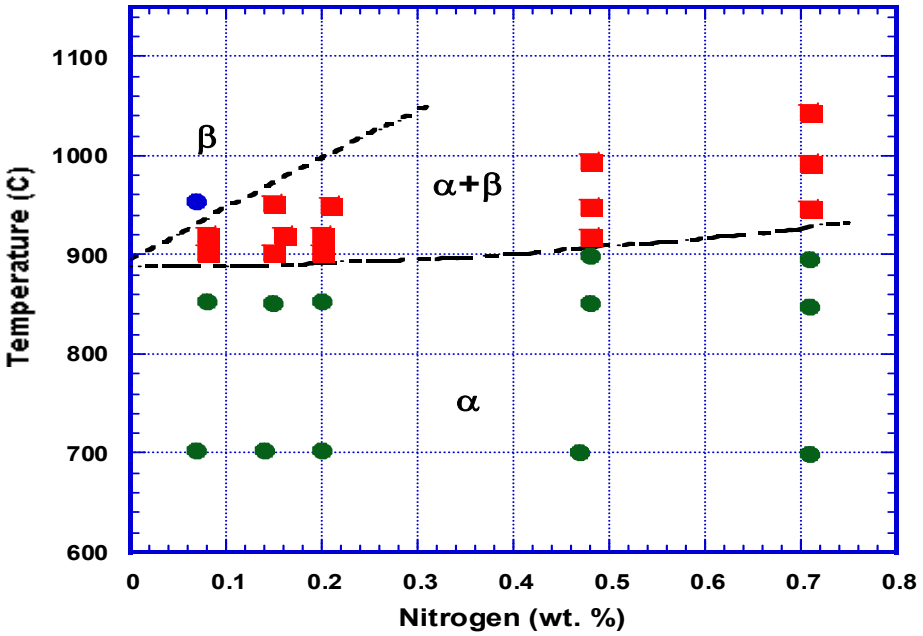

Figure 2.5 The α and β phase fields of Ti as affected by the N content (Adapted from [27])

broadening the α + β phase field. The phase diagrams shown indicate this broadening in terms of two solvus lines. The transition from the complete α phase to the α + β phase field is demarcated by the α → α + β solvus line and the subsequent transition from the α + β phase to complete β phase is marked by the α + β→ β solvus line.

In addition to the interstitial alloying elements discussed above, many alloying elements form substitutional alloys with titanium. Depending on the alloying element added, it can either increase or decrease the α/β phase transition temperature. Elements such as Sn, Al and O increase the transformation temperature and hence are known as α-stabilizers.[25, 28] On the other hand elements such as Fe, Mo, V decrease the transition temperature and hence are known as β-stabilizers.[29] Depending on the elements added, commercially available titanium and its alloys are classified as α, β and α + β alloys. A brief discussion of these different types of Ti-alloys is presented below.

2.1.1 α-alloys

Unalloyed as well as alloys of titanium which retain the HCP structure at room temperature are called α alloys. These alloys can contain substitutional elements like Al, Sn, and interstitial elements like O, C and N. These alloying elements are soluble in the α-matrix and stabilize the HCP phase. The strength and ductility of these alloys are influenced by grain size, interstitial contents and any dislocation state caused by hot/cold working.

2.1.2 β-alloys

Upon addition of transition elements like Fe, Mo, V, Nb, Ta etc., the BCC phase of Ti is either partially or fully stabilized at room temperature depending on the total amount of β-stabilizing elements. These alloys can be further classified into two categories: metastable β-alloys and stable β-alloys. In metastable β-alloys, alloying additions do not stabilize the β-phase completely in the matrix at the room temperature. In stable β-alloys, the microstructure is completely stabilized with β phase at room temperature.

2.1.3 α + β alloys

Most of the commercial alloys of titanium have alloying elements that stabilize both α and β phases, with the relative proportions of the phases being determined by the total content of each group of α or β-stabilizing elements. Further, there are two subdivisions of these α + β alloys, near α alloys and near β alloys. In near α alloys, a relatively higher amount of α-stabilizing alloying elements is present and the microstructure is predominantly α phase with negligible or very small amount of β phase.

In the case of near β alloys, the microstructure is made of mostly β phase due to a relatively higher amount of β- stabilizing alloying elements.

2.2 Surface performance of titanium

It is well known that titanium and its alloys undergo severe wear and surface degradation under contact and/or sliding conditions. In tribology, there are specific terms for each surface degradation process and they include wear, fretting, gouging/galling and seizure. Wear is more of a generic term that refers to removal of material from either surfaces when the surfaces are in contact.[30] The ASTM definition[31] of galling is " a form of surface damage arising between sliding solids, distinguished by macroscopic, usually localized, roughening and creation of protrusions above the original surface. It often includes plastic flow, material transfer, or both." Care is required to discriminate whether a material has undergone normal wear, galling or seizure.[32] Figure 2.6 shows schematically some of the differences among these phenomena.[32] Galling is characterized by the formation of excrescence. When the running clearance for the material outgrowth is limited, these excrescences rise above the surface of the materials causing seizure as shown in Figure 2.6.

The process and the factors influencing galling have been documented in the literature.[33-35] Galling primarily depends on the frictional forces between the surfaces in contact. Low frictional forces between the sliding surfaces lead to lesser galling. In counterformal contact conditions, flow of materials in lateral directions also leads to lesser galling. Other important factors that reduce galling are rapid work hardening,[36] high hardness[37-39] and low surface energy.[40] It has also been witnessed that galling in

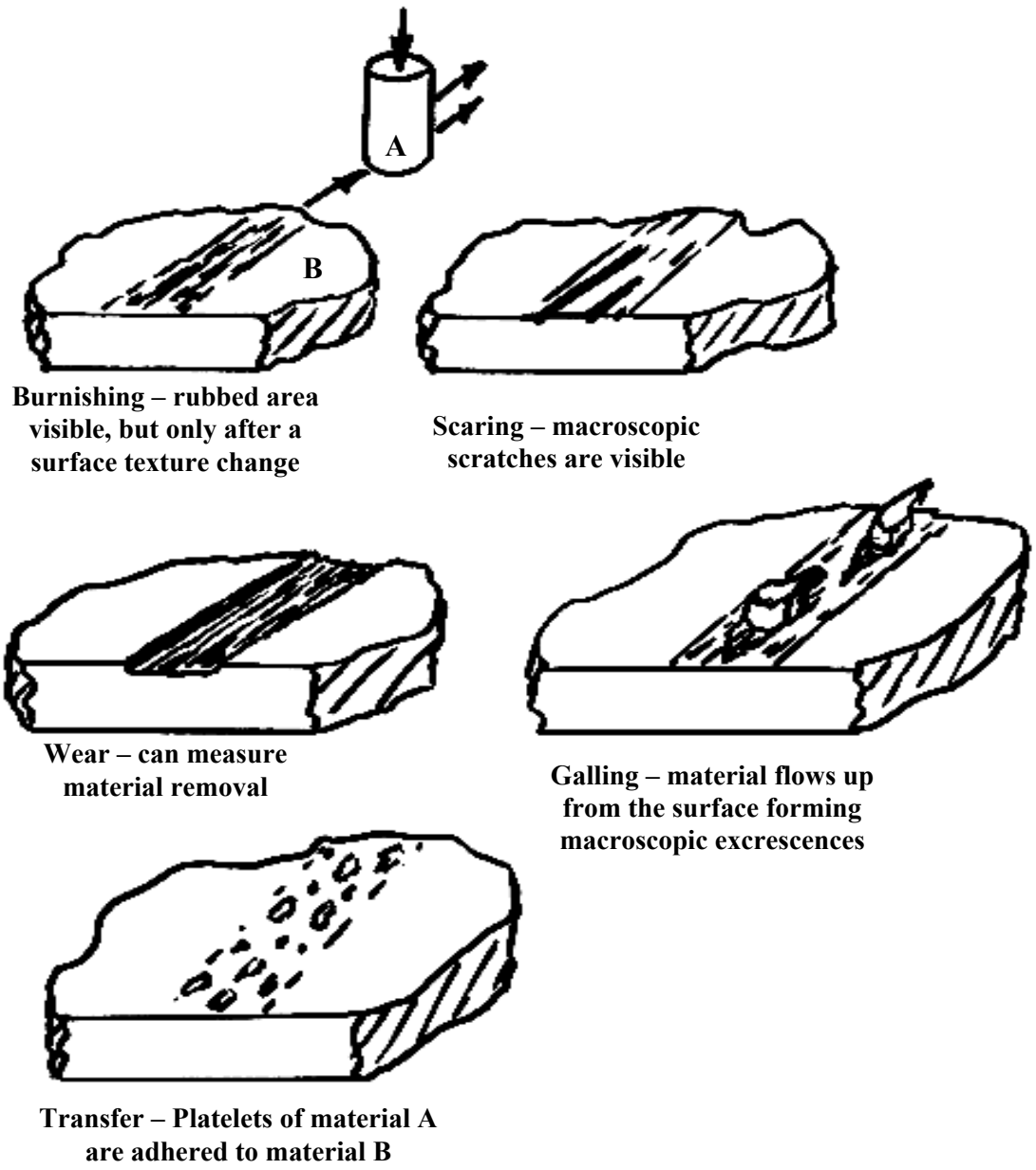

Figure 2.6 Various types of wear upon rubbing a flat ended pin on solid surface (Adapted from [32])

high hardness[37-39] and low surface energy.[40] It has also been witnessed that galling in pure metals can occur at low contact stresses.[41] Seizure is defined as the sticking of two surfaces upon sliding against each other, due to relative motion between them, under load.[42] The relative motion causes interfacial adhesion between the surfaces. Seizure in Ti can cause damage to a component in service in two ways.[42] The first one is called the fretting-fatigue where the sliding motions between the surfaces introduce crack nucleation and subsequent crack growth causing failure. The second type of seizure is known as the fretting-wear. It involves loss of material from the sliding surfaces under the influence of external vibrations. Table 2.1 listed some values of the coefficient of friction and the degree of wearing when titanium is in contact with itself and with other metals.

2.2.1 Coatings on titanium

Surface modification of Ti and its alloys is often performed to improve their performance during service.[43] One such surface modification technique is the creation of some hard, adherent and wear resistant surface coatings by diffusion. This is done by diffusing interstitial elements like O, C, N, or B into the surface of Ti.[44] These interstitial

Table 2.1 Friction and wear data for various metals in contact (Adapted from [30])

Metals in contact	Coefficient of friction	Wear (g/cm of wear track)
Titanium on titanium	0.47	2.5 E-6
Mild steel on mild steel	0.53	7.5 E-6
Stainless steel on stainless steel	-	2.5 E-6
Copper on copper	1.1	10 E-6
Titanium on mild steel	0.25	10 E-7
Titanium on copper	-	6 E-7

elements, O, C, N or B react with Ti to form oxide, carbide, nitride, or boride layers, respectively, on the surface of Ti.[44] These surface layers are hard and impart improved wear resistance. Some of the coating technologies as employed to Ti will be discussed briefly here.

2.2.2 Titanium nitride coatings

The Ti-N binary phase diagram is shown in Figure 2.7.[45] Nitrogen has ~ 8 % solid solubility in α- titanium at 1050 ˚C and it enables the formation of nitride layers on the surface to improve its hardness and wear resistance significantly. Hence, nitriding is used often in industry to coat titanium and steel surfaces for various applications needing improved wear resistance.[46-49] Some of the major nitriding techniques as applied to titanium are elucidated below.

2.2.2.1 Plasma nitriding. Plasma nitriding is a research and development type process often studied to coat titanium surfaces.[47, 48] It is mainly done by submerging the substrate in a bath of nitrogen ions generated by radio-frequency plasma. When a very high negative potential is applied to the substrate, these ions are accelerated towards the target from the plasma. These ions then react with titanium to form the nitrided layers at the surface. It is generally done in a temperature range between 400 to 950 ˚C and for time periods of a few minutes to several hours. The plasma nitriding process in Ti-6Al-4V alloy can create a compound layer of about 50 μm in depth with microhardness values in the range of 600-2000 HV. [44]

2.2.2.2 Ion-beam nitriding. Ion beam nitriding process involves accelerating nitrogen ions to a very high velocity. The high kinetic energy of the ions enables them to penetrate deeper into the titanium substrate. The process is performed in a temperature

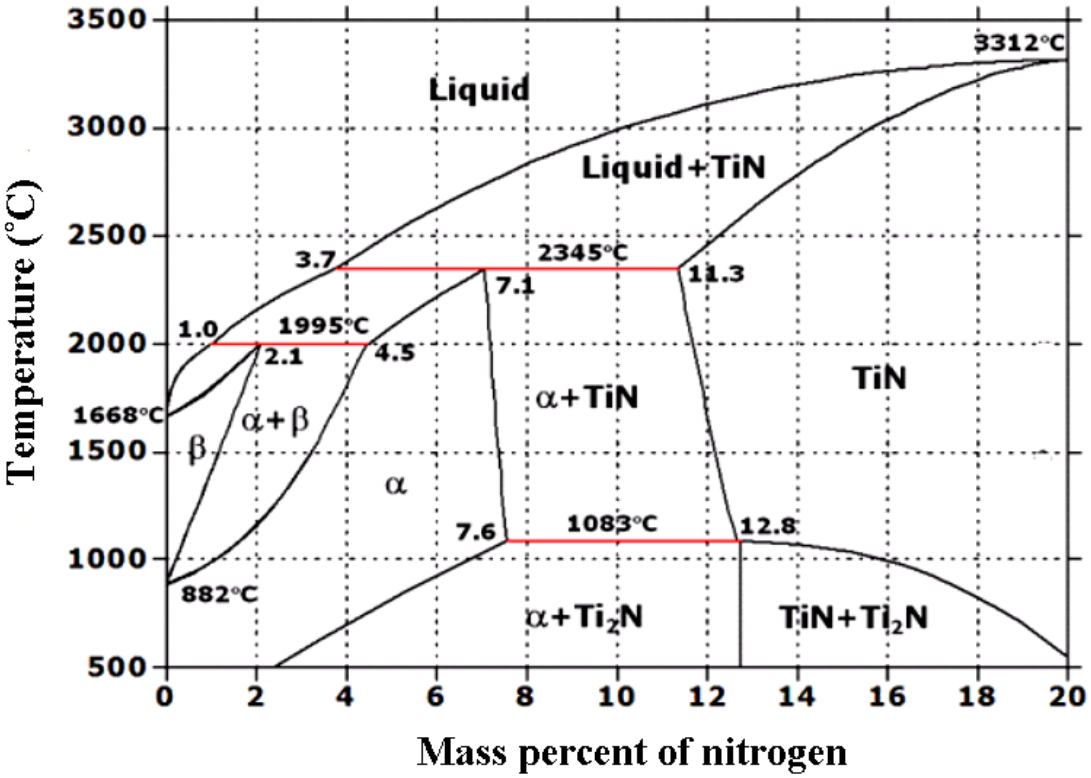

Figure 2.7 Ti-N phase diagram (Adapted from [45])

range of 500 to 900 ˚C for 30 minutes to 20 hours in an Ar atmosphere. A compound titanium nitride layer of about 5-8 µm in thickness and having microhardness values in the range of 800-1200 HV was achieved in Ti-6Al-4V alloy.[50-52]

2.2.2.3 Laser nitriding. A very high energy focused laser beam is used to melt the surface of the titanium substrate. The molten depth can range from 1-1.5 µm,[53-56] to as high as 400 µm[44] in order to obtain thick hardened layer for applications needing improved wear resistance. When the melted layer is exposed to a nitrogen gas environment, titanium nitride compound layers are formed with a very good metallurgical bond between the layer and the substrate. Microhardness values in the range of 900-1300

HV have been obtained on Ti-6Al-4V alloy. However, this process is expensive and restricted to limited substrate geometries.

2.2.2.4 Gas nitriding. Gas niriding is a relatively easy process to implement, and it is well suited for complicated geometries. Titanium is nitrided with nitrogen gas or a mixture of nitrogen and hydrogen/argon in a vacuum chamber. Hardened coatings of thickness of about 2-15 μm and with microhardness values in the range of 450-1800 HV have been obtained on Ti-6Al-4V alloy. A disadvantage associated with this process is that it reduces the fatigue life of the substrate.[49, 57]

2.2.2.5 Microstructure of nitrided layers. The ingress of nitrogen in α-Ti substrate leads to the formation of an interstitial solid solution. Diffusion of nitrogen into the Ti leads to the formation of compounds such as Ti_2N and TiN. Ti-N phase diagram (Figure 2.7) reveals that above 12.7 wt% N and below 1100 ˚C, Ti_2N is predominantly formed. However, as the N content increases, TiN starts forming. Thus, nitriding of titanium produces a thin layer of TiN on the surface. Below the TiN layer, a thicker compound layer of Ti_2N is formed and below which a diffusion zone of nitrogen-strengthened titanium exists. Figures 2.8(a) and (b)[49, 57-59] show these layers of TiN, Ti_2N and diffusion hardened layer in α-titanium. The coating layer thickness (total added thicknesses of TiN and Ti_2N) varies between 1 to 50 μm while the diffusion hardened zone can be up to hundreds of micrometers.

2.2.3 Modeling of kinetics of titanium nitride coatings

Several successful attempts have been made to model the growth kinetics of nitride layers in Ti and its alloys.[47-49, 60] These models are formulated to extract anyone of the two types of specific information: i) With the known diffusivities of the diffusing

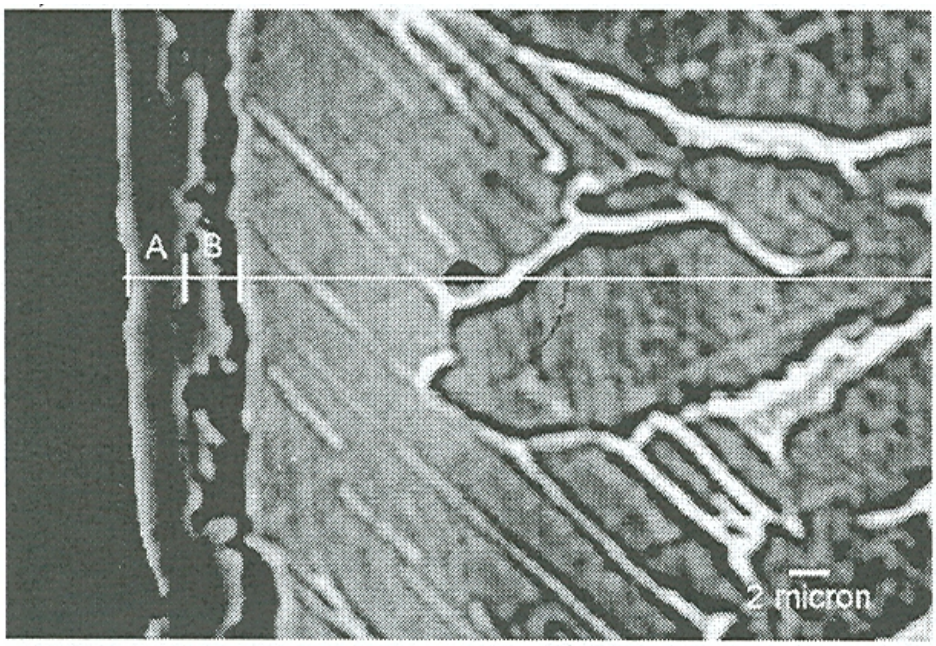

(a)

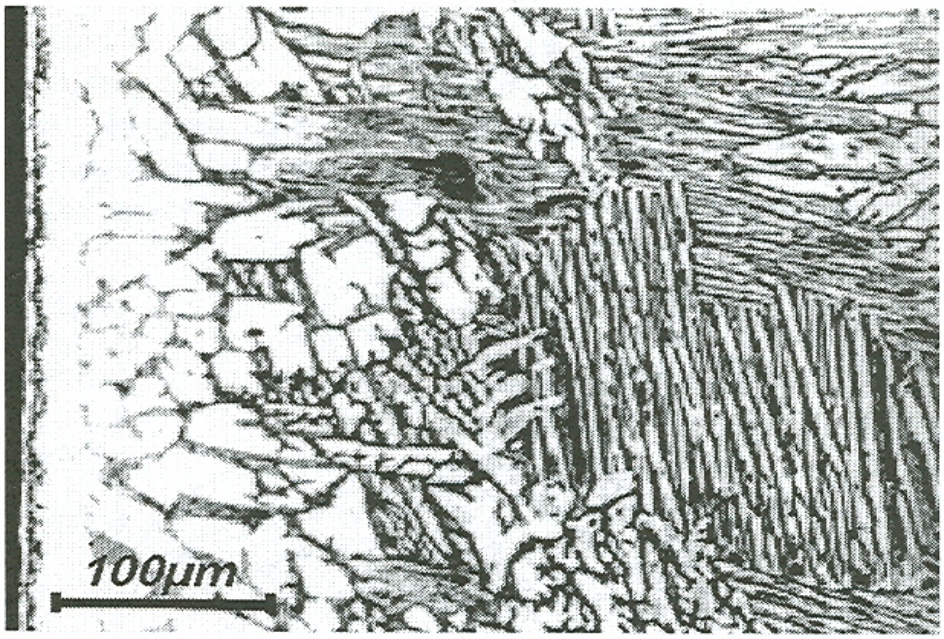

(b)

Figure 2.8 SEM micrographs of Ti-6Al-4V, plasma nitrided at (a) 900 ˚C for 6 hours and (b) 900 ˚C for 14 hours (Adapted from [49])

species in different phases, estimation of coating layer thickness for a fixed treatment temperature and time or ii) estimation of diffusivities of the diffusing species in different phases knowing the coating layer thickness at a fixed temperature and time. The basis of one such model will be briefly described in this section.

Taktak et al.[60] studied the diffusion kinetics of plasma nitriding in Ti-6Al-4V alloy and modeled the nitride layer growth kinetics using semi-infinite, multiphase, volume diffusion characteristics. Figure 2.9 illustrates the partial Ti-N phase diagram along with the nitrided layers formed; δ and ε represent the TiN and Ti_2N layers, respectively, followed by the α and β matrix of titanium. The corresponding nitrogen concentrations at the interfaces are also indicated in the figure. The change in nitrogen concentration with time is given by Fick's second law as,

$$\frac{\partial C}{\partial t} = \frac{\partial}{\partial x}\left(D\frac{\partial C}{\partial x} \right) \tag{2.1}$$

where C is the concentration at distance x from the surface and D is the diffusion coefficient. From Fick's first law, diffusion fluxes at each phase boundary are given as:
For the δ/ε interface,

$$J_{\delta\varepsilon}^{-} = -D_{\delta}\left(\frac{\partial C_{\delta}}{\partial x} \right)_{x=k_{\delta\varepsilon}} \tag{2.2}$$

For the ε/α interface,

$$J_{\varepsilon\alpha}^{-} = -D_{\varepsilon}\left(\frac{\partial C_{\varepsilon}}{\partial x} \right)_{x=k_{\varepsilon\alpha}} \tag{2.3}$$

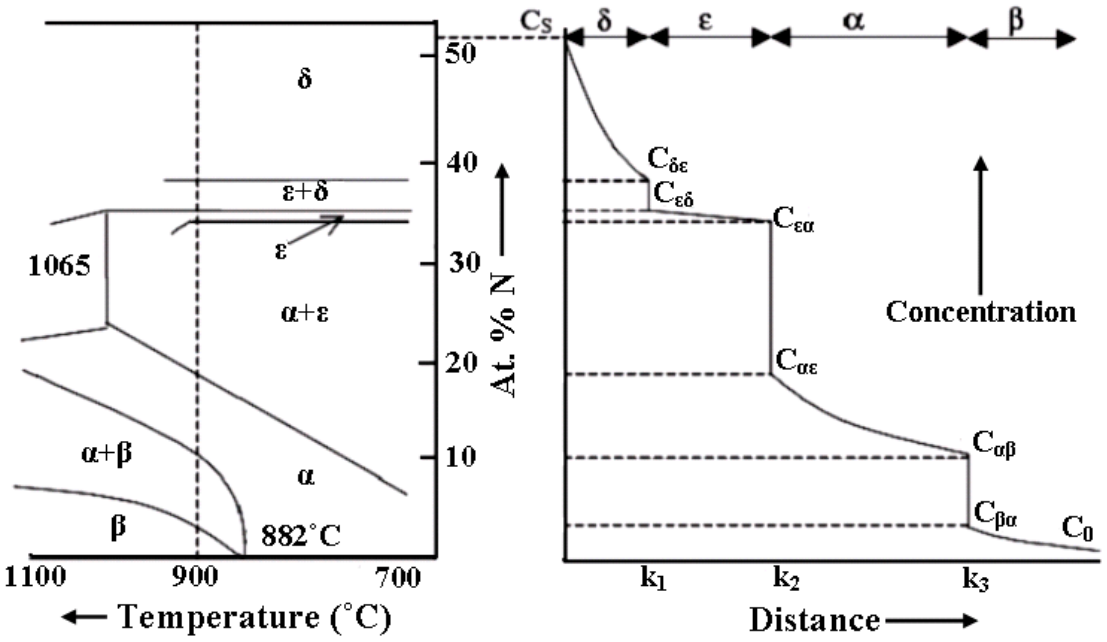

Figure 2.9 The schematic representation of the partial Ti-N phase diagram and the associated diffusion layers formation in Ti-6Al-4V alloy (Adapted from [60]).

$$J^{+}_{\alpha\varepsilon} = -D_{\alpha}\left(\frac{\partial C_{\alpha}}{\partial x}\right)_{x=k_{\alpha\varepsilon}} \tag{2.4}$$

For the α/β interface,

$$J^{-}_{\alpha\beta} = -D_{\alpha}\left(\frac{\partial C_{\alpha}}{\partial x}\right)_{x=k_{\alpha\beta}} \tag{2.5}$$

$$J^{+}_{\beta\alpha} = -D_{\beta}\left(\frac{\partial C_{\beta}}{\partial x}\right)_{x=k_{\beta\alpha}} \tag{2.6}$$

Here D_δ, D_ε, D_α and D_β are the respective diffusion coefficients of nitrogen in TiN, Ti_2N, α and β phases. J^- and J^+ are the fluxes from the negative and positive sides of a particular interface. C is the concentration of a particular phase. In general, the solution of Fick's second law, satisfying Eqn. (2.1) is,

$$C(x,t) = A_i + B_j erf\left(\frac{x}{\sqrt{Dt}}\right) \tag{2.7}$$

Here A_i and B_j are constant associated with each phase. From Figure 2.9, the values of A_i and B_j are as follows,

$$A_\delta = C_S, \quad B_\delta = C_S - C_{\delta\varepsilon} \tag{2.8}$$

$$A_\varepsilon = C_{\varepsilon\delta}, \quad B_\varepsilon = C_{\varepsilon\delta} - C_{\varepsilon\alpha} \tag{2.9}$$

$$A_\alpha = C_{\alpha\varepsilon}, \quad B_\alpha = C_{\alpha\varepsilon} - C_{\varepsilon\beta} \tag{2.10}$$

$$A_\beta = C_{\beta\alpha}, \quad B_\beta = C_{\beta\alpha} - C_O \tag{2.11}$$

Incorporating these boundary conditions as well as the flux equations, the solution for Fick's second law can be modified to get the interface velocities for each interface. The δ/ε interface velocity equation, as derived by the author, is,

$$\left(\frac{B_\delta}{\sqrt{\pi}Z_{\delta\varepsilon}}\right)\frac{\exp\left[-\left(\frac{k_{\delta\varepsilon}}{2\sqrt{D_\delta t}}\right)^2\right]}{\frac{k_{\delta\varepsilon}}{2\sqrt{D_\delta t}}erf\left(\frac{k_{\delta\varepsilon}}{2\sqrt{D_\delta t}}\right)}=\left(\frac{\sqrt{D_\varepsilon}B_\varepsilon}{\sqrt{D_\delta\pi}Z_{\delta\varepsilon}}\right)\frac{\exp\left[-\left(\frac{k_{\varepsilon\alpha}}{2\sqrt{D_\varepsilon t}}\right)^2\right]}{\frac{k_{\delta\varepsilon}}{2\sqrt{D_\delta t}}\left[erf\left(\frac{k_{\varepsilon\alpha}}{2\sqrt{D_\varepsilon t}}\right)-erf\left(\frac{k_{\varepsilon\delta}}{2\sqrt{D_\varepsilon t}}\right)\right]} \tag{2.12}$$

where, $Z_{\delta\varepsilon}=C_{\delta\varepsilon}-C_{\varepsilon\delta}$

Similar equations were derived for the ε/α and α/β interfaces. These equations were numerically solved to estimate the diffusivities of nitrogen in TiN, Ti_2N and α phases. Also the activation energies for nitrogen diffusion in TiN and Ti_2N were determined through this modeling work. The estimated diffusivities of nitrogen agree reasonably well with the experimentally measured diffusivities in the respective phases.

2.2.4 Titanium oxide coatings

Titanium has the general tendency to form an oxide layer at surface, even at room temperature.[61] Although an oxide layer in titanium imparts improved tribological properties,[44] it makes it more difficult to create titanium coatings with other elements such as nitrogen or boron. In the bulk, oxygen increases the strength level of α-titanium by solid solution strengthening. The oxidation kinetics have been extensively studied in the past.[61-69] It was reported that oxidation of titanium below the phase transition temperature, i.e., in the α field, produced very limited coating growth. When oxidation was done in the β field, noticeable hardening and coating growth were observed. However, the high temperature in the β field also caused severe embrittlement of the oxide layer. Hence, the challenge has always been to form an appreciable oxide coating

on the surface without causing embrittlement and degradation of the oxide layer.

Ti-O phase diagram indicates about 3.5% solid solubility of oxygen in α-titanium at 400˚C as shown in Figure 2.10.[70] Oxygen atoms occupy the interstitial sites in α-titanium. However, upon exposure to high temperature, the titanium surface will form a porous, poorly adherent and thick oxide scale with a solution hardened diffused layer below the oxide layer. Generally, oxide coatings in titanium surface are grown in the temperature range of 850-1000 ˚C in air at a pressure range of 10^{-3} to 10^{-2} mm of Hg.[63] At such high process temperature, a hardened surface layer is formed together with a considerable amount of scaling.[63] The scale reduces the coefficient of friction.[63] To avoid

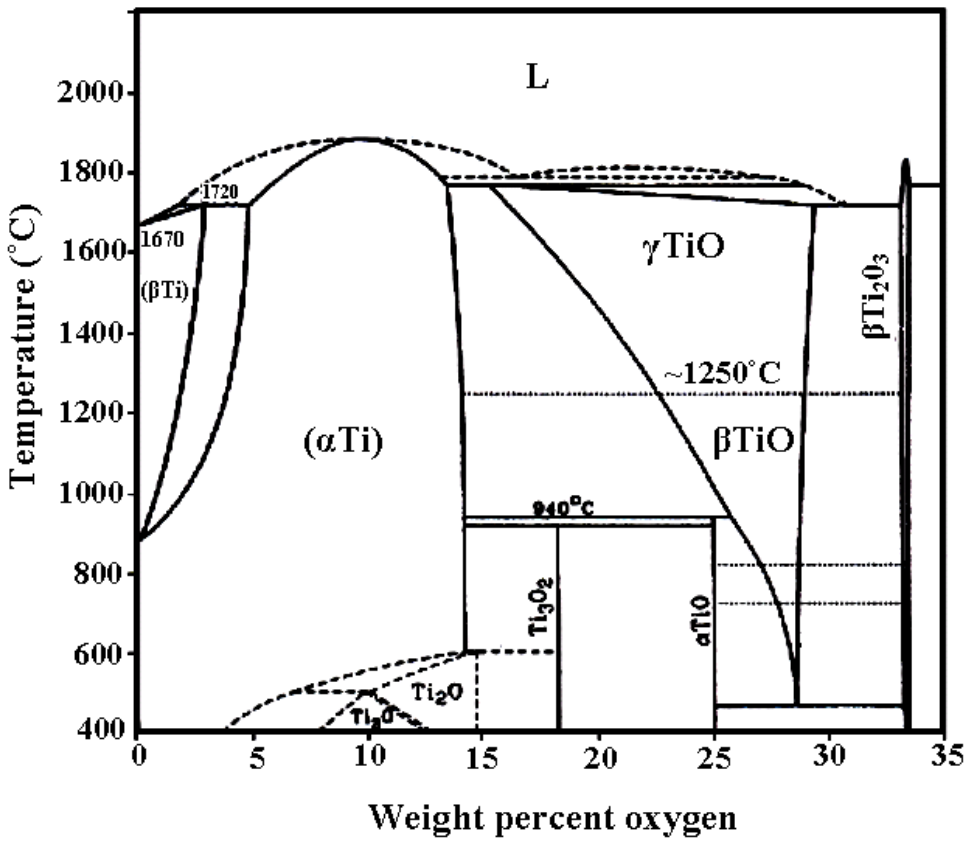

Figure 2.10 Ti-O phase diagram (Adapted from [70])

severe scaling, controlled oxidation of Ti in molten salts was attempted at a lower temperature range.[44] For example, titanium pistons are oxidized in controlled, molten salt atmosphere and in a temperature range of 600-900 ˚C for 2 to 4 hours to avoid excessive oxide layer formation.[68] Several other α-Ti, α + β-Ti and β-Ti alloys had been oxidized and tested for wear and biomedical applications.[61-69] Ti-22V-4Al alloy, upon oxidation, produced better wear resistant coating than nitriding or carburizing.[67] Oxidation of Ti-6Al-7Nb alloys resulted in maximum surface hardness of 900 HV with hardened subsurface layer up to 50 μm in depth.[44] A novel gas based technique developed for treating Ti-6Al-4V alloys is the tifran* process.[66] Reduction in the wear rate in gears treated with this process has been reported.[66] However, the maximum hardness obtainable through titanium oxide coatings (1000 HV) is significantly less than the maximum hardness achievable in titanium nitride (Ti_2N) coatings (1500 HV).[44]

2.3 Boriding of metals

Conventional surface hardening treatments where elements are diffused atomistically into a substrate, for example carburizing, nitriding, or carbo-nitriding usually result in a surface hardness level of 800–1100 HK in steels. However, applications requiring very hard surfaces demand hardness as high as 1800–2000 HK. Boride layers can yield hardness levels of this order.[71-75] Boron can readily diffuse in metals such as iron/steel and nickel and can produce a much harder surface than that of a carburized surface. In steels, however, thick boride layers are not reliable as the diffused

* Tifran is a gaseous oxidation process employed to Ti and its alloys at a temperature in the range of 500 to 725˚C for 0.5 to 100 hours of treatment time. The treatment temperature and time are adjusted to get an adherent surface compound layer of atleast 50% by weight of oxides of Ti to a depth of about 0.2 to 2 μm on a solid solution strengthened diffused zone of diffusing element oxygen penetrating to a depth of 5 to 50 μm. This is a patented process and the brief detail obtained from the website : http://www.freepatentsonline.com/6210807.html

coating layer of FeB formed during boriding has a different coefficient of thermal expansion from that of the Fe substrate which can eventually lead to cracking of the coating. When controlled boriding is performed, hard and durable Fe_2B layers of about 100 μm in thickness can be created.

Boriding can be done in gas phase, molten salt, or solid state pack medium. Gaseous boriding agents like KBF, NaB, $Na_2B_4O_7$, B_2H_6, and BCl_3 are commonly employed for boriding.[76] In these processes, the boron source gas is mixed with some reducing agents to use as a boriding medium. Gas boriding produces a very uniform boride layer on the substrate in relatively lesser time. The boriding agents are, however, hazardous and expensive.

Liquid phase boriding is done normally in $Na_2B_4O_7$, HBO_2 and $NaBF_4$ salts. In a study by Belyaeva et al.,[77] liquid phase boriding on steel was done in a liquid melt containing 60-80% borax and a 20-40% boron containing substance like boron carbide, ferroboron, or calcium hexaboride. It was found that a liquid melt containing 70% borax and 30% boron carbide produces a boride coating of about 150 μm deep into a steel substrate at 1000˚ C for 6 hours. Liquid phase boriding can be beneficial over solid state because of the higher chemical activity of the boron source in the liquid melt.[78] But the main disadvantages associated with these processes are to achieve good fluidity in the liquid bath and very high operating cost.[78]

The solid state boriding substances include amorphous boron, ferroboron, and B_4C with theoretical boron content 95–97 wt%, 17–19 wt% and 77.28 wt%, respectively. Amorphous boron proves to be a more effective boriding medium than crystalline boron.[79] This may be due to the greater surface area of amorphous boron as determined

by Haag,[80] and listed in Table 2.2. Generally, solid state boriding is relatively easy to implement and somewhat less expensive.

Solid state boriding had been performed in vacuum as well as inert atmosphere. Minkevic[81] argued that such atmosphere is necessary for boriding, but this suggestion was disputed by Kunst and Schaaber (quoted in [82]). The authors reported higher coating thicknesses of the boride layers when boriding was done with amorphous boron in the absence of vacuum. For example, boriding of Armco iron at 1000 ˚C for 3 hours resulted in a coating thickness of about 200 μm at atmospheric pressure, whereas at a vacuum of 10^{-5} Torr, the coating thickness was limited to 30–40 μm. A great variation in coating thicknesses has also been observed with varying compositions of the powder mixture employed in solid state boriding.[75] A mixture of 33% amorphous boron, 65% Al_2O_3, and 2% NH_4Cl resulted in layer thickness of about one–fourth of the thickness obtained by pure amorphous boron. Optimized power composition is necessary for enhanced coating growth in solid state boriding.

Table 2.2 List of boron powders and their respective surface areas

Powder	**Purity (%)**	**Surface area (m^2/g)**
Crystalline boron	99	< 1
Amorphous boron	95-97	12-15
Amorphous boron	99.9	24

2.3.1 Structure of boride layers on iron/steel

When steel is borided, it forms a whisker layer of Fe_2B on the surface. FeB, although a thermodynamically feasible phase, has the tendency to crack because of thermal coefficient mismatch. Diffusion of B in steels exhibits a parabolic relationship with time suggesting that it is diffusion controlled process.[75] Figure 2.11 (a) and (b) shows the microstructures of steels borided at different temperature and time.

The effect of alloying elements on the thickness of boride layers on steel has been studied.[75] It has been found that steels having a smaller amount of alloying elements exhibit a relatively higher coating thickness.[75] Figure 2.12 shows the effect of different alloying elements on the boride coating thicknesses in steel. It is evident from the figure that as the alloying content increases the coating thicknesses of the boride layers decreases. There are some exceptions to this general trend, for example, up to around 7% addition of Mn in steel did not affect the coating thickness.[83] Blanter and Basedin[84] did boriding experiments in alloyed steels in a mixture of 60% borax and 40% boron carbide for 5 hours at 1100 ˚C. The authors reported relatively lesser boride coating thicknesses in alloyed steel compared to that of unalloyed steels. Lachtin and Peelkina[83] reported that high alloyed steel borided in a diborane hydrogen mixture in a ratio of 1:25 imparted a lesser coating thickness with small amount of Cr (2%) and Ni (2%) whereas chrome steel exhibited increased boride layer thickness even after addition of 2.2% W. So, boride coating thickness level achievable in steel surface depends on type of alloying elements present as well as the quantities of such elements.

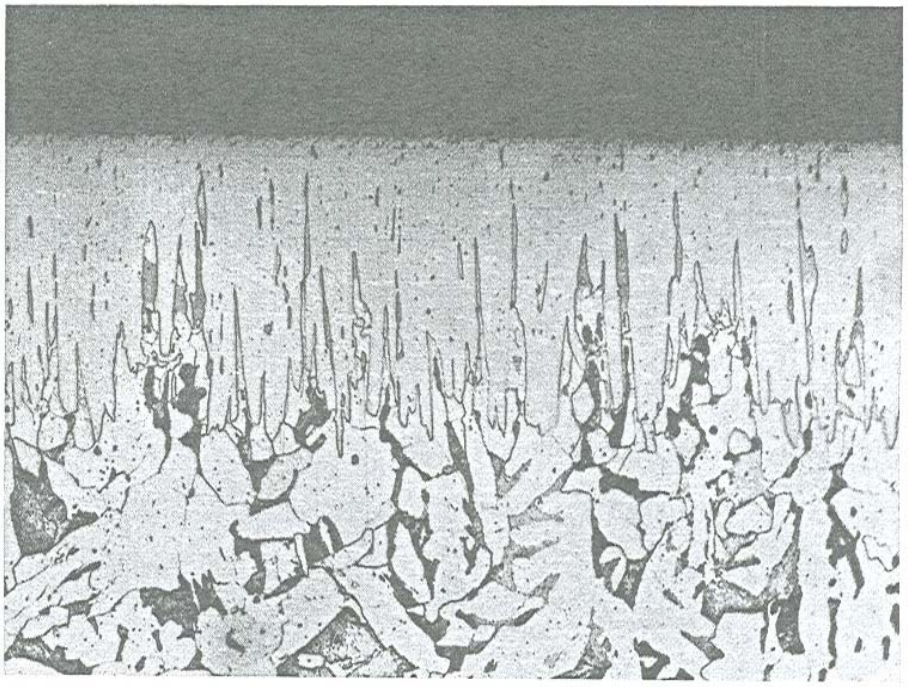

(a)

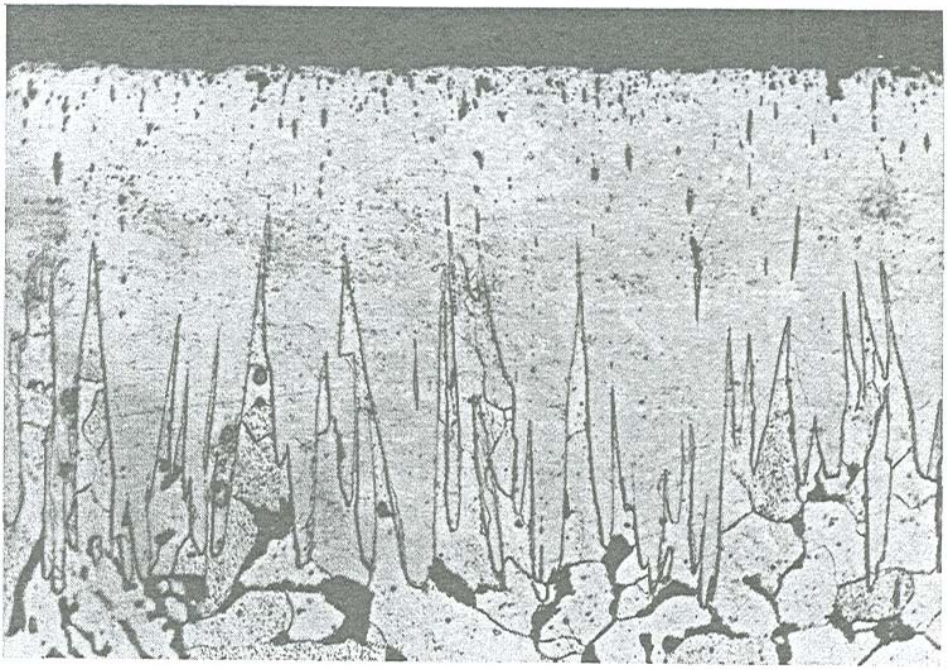

(b)

Figure 2.11 Microstructure of steels boronized at 900 °C (200X) (a) Steel St 37 boronized in Ekabor for 10 hours (200X), (b) Steel C15 boronized in Ekabor for 4 hours (Adapted from [75])

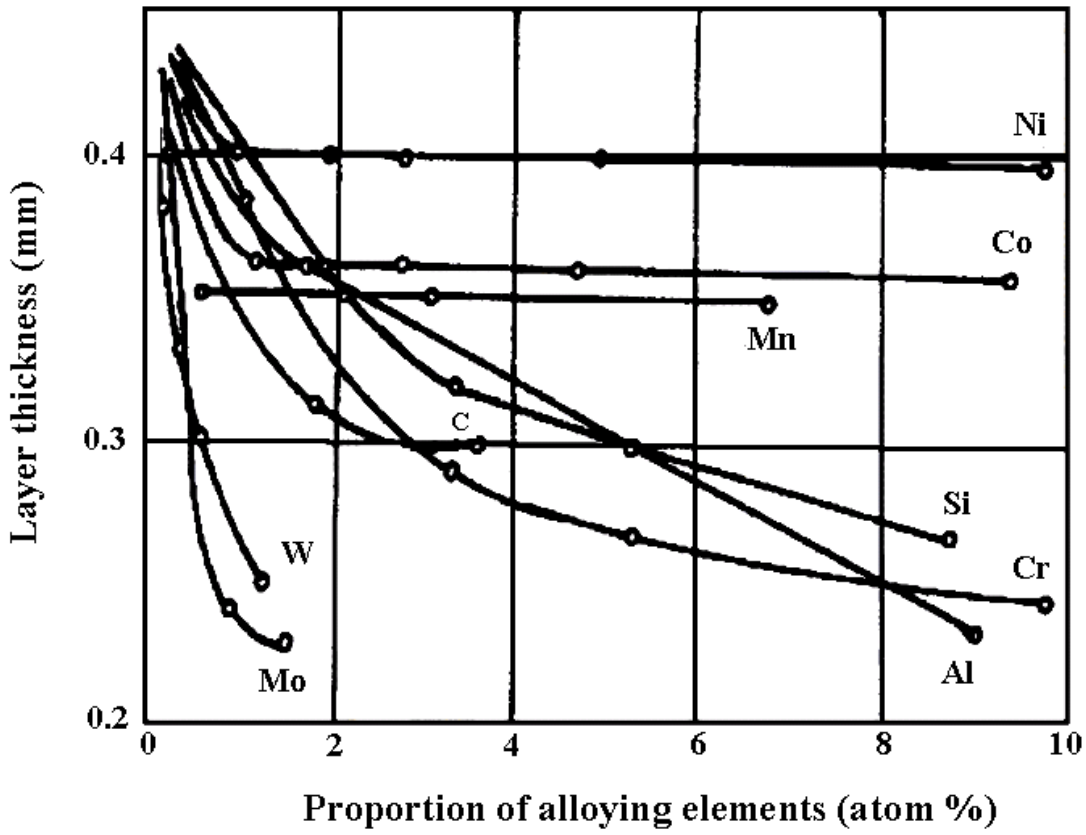

Figure 2.12 Variation of boride coating thicknesses obtained in the iron substrate with different proportions of alloying elements (Adapted from [75]).

2.3.2 Modeling of boride growth in iron/steel

The FeB/Fe_2B layer growth kinetics during boriding of Fe or steel has been modeled in a number of studies.[85, 86] In one such study by Yu et al.,[85] the dual boride layer formation in mild steel was modeled based on six elementary physico-chemical processes:

1. B (free)→ B (adsorption)
2. B (adsorption) + Fe → FeB if C_{ads}^{B} >0.5

   B (adsorption) + 2Fe → Fe_2B if 0.33< C_{ads}^{B} <0.5

B/ Fe_2B interface;

3. B atoms jump through FeB or Fe_2B lattice from high to low chemical potential side
4. $Fe_2B + B \rightarrow 2FeB$ at FeB/ Fe_2B interface;
5. $2Fe + B \rightarrow Fe_2B$ at Fe_2B/Fe interface;
6. $2FeB \rightarrow Fe_2B + B$ phase transformation.

For boride layer growth, one or several of these above mentioned steps can be the rate-determining steps. In this model, however, the growth simulation was done with the following assumptions: (i) the interface reactions are sufficiently fast so that the B diffusion in step 3 is the rate determining one, (ii) concentration of B in steel matrix is negligible, and (iii) the B diffusion co-efficient is constant within the diffusion layer. The total boride layer growth is dominated by the B diffusion through three phases: FeB phase, Fe_2B phase and the Fe phase. In general, Fick's second law can be applied for the diffusion of B through these phases as,

$$\frac{\partial C}{\partial t} = D_i \frac{\partial^2 C}{\partial x^2} \qquad (i = 1 \text{ for } 0<x<u \text{ and } i = 2 \text{ for } u<x<v) \tag{2.13}$$

where D_1 and D_2 are the diffusion coefficients of B in FeB and Fe_2B phases. The variables u and v are the locations of the FeB/Fe_2B and Fe_2B/Fe interfaces. Before the start of boriding,

$$C_{Fe_2B} = 0,\ C_{FeB} = 0 \text{ at x = 0 and t < 0.} \tag{2.14}$$

The B concentration profile from the surface to the depth of the steel sample is illustrated in Figure 2.13. The upper and lower limit of B concentrations in FeB and Fe_2B phases are

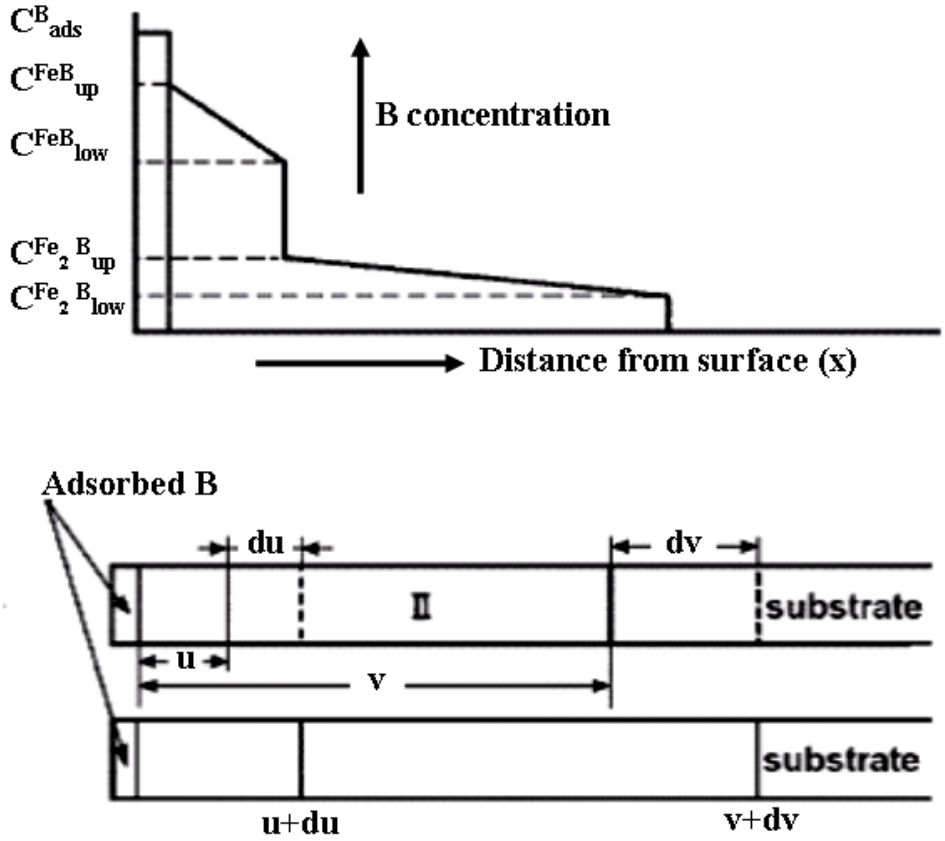

Figure 2.13 B concentration profile used for the modeling (Adapted from [85])

designated as C_{up}^{FeB}, C_{low}^{FeB}, $C_{up}^{Fe_2B}$ and $C_{low}^{Fe_2B}$ respectively. From Figure 2.13, the boundary conditions are as follows,

$C = C_{up}^{FeB}$ for C_{ads}^{B} >0.5 at x = 0, (2.15)

$C = C_{low}^{FeB}$ for C_{ads}^{B} >0.5 and with FeB phase at x = u - 0, (2.16)

$C = C_{up}^{Fe_2B}$ for 0.33< C_{ads}^{B} <0.5 and without FeB phase at x = u + 0, (2.17)

$$C = C_{low}^{Fe_2B} \text{ for } C_{ads}^{B} < 0.33 \text{ at } x = v - 0, \tag{2.18}$$

$$C = 0 \qquad \text{at } x = v + 0 \tag{2.19}$$

In an infinitesimally small time interval 'dt', the growth of FeB and Fe_2B layers will occur by simultaneous consumption of Fe_2B and Fe at FeB/Fe_2B and Fe_2B/Fe interfaces, respectively. Considering that 'du' and 'dv' are the respective extensions of FeB and Fe_2B layers in time interval 'dt' and since B should be conserved at the FeB/Fe_2B and Fe_2B/Fe interfaces,

$$(C_{low}^{FeB} - C_{up}^{Fe_2B})\, du = \left[-D_1 \left(\frac{\partial C}{\partial x} \right)_{u-\varepsilon} + D_2 \left(\frac{\partial C}{\partial x} \right)_{u+\varepsilon} \right] dt, \tag{2.20}$$

$$C_{low}^{Fe_2B}\, dv = \left[-D_2 \left(\frac{\partial C}{\partial x} \right)_{v-\delta} \right] dt \tag{2.21}$$

Numerically solving Eqns. (2.20) and (2.21), the depth to which coating layers, FeB/Fe_2B, penetrated were calculated. Numerically calculated values were in reasonable agreement with the experimentally found ones.

2.3.3 Boriding of titanium

Boriding of titanium and its alloys has been studied in our research group for the last couple of years [87-89] in an effort to create hard TiB_2/TiB layers on the surface of Ti. According to the Ti-B phase diagram[90] shown in Figure 2.14, three hard compounds exist: TiB at 18-18.5 wt%, Ti_3B_4 at 22.4 wt% and TiB_2 at 30.1-31.1 wt% boron compositions. These compounds are characterized by very high hardness (>20 GPa in

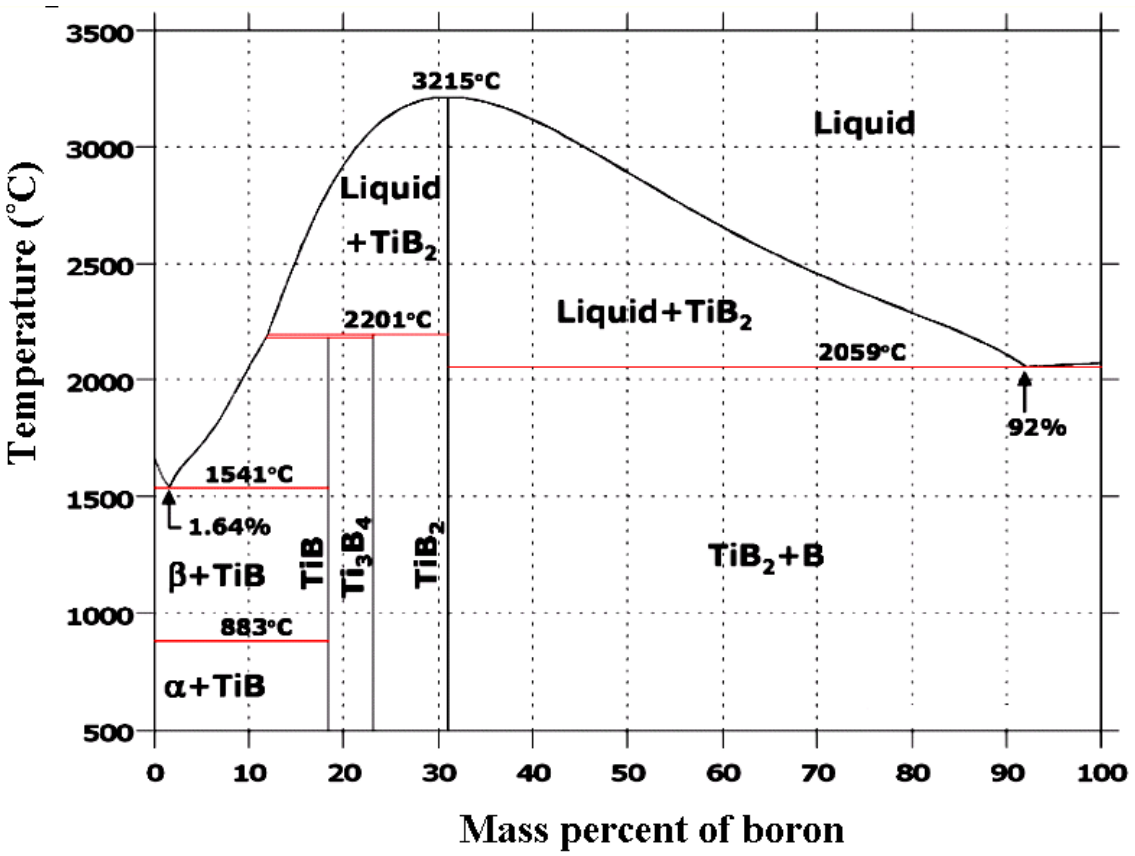

Figure 2.14 Ti-B phase diagram (Adapted from ASM International [90])

HV for TiB and >30 GPa in HV for TiB_2) and their crystal structures are B27, D7b, and C32, respectively.[91] The Ti-B phase diagram also reveals that TiB forms by peritectiod reaction, TiB_2 by congruent melting, and Ti_3B_4 by peritectic reaction.

A substantial amount of research has been performed to study the morphologies, crystallographic structures, and mechanical properties of these borides.[92-95] Sahay et al.[92] studied the formation and morphology of TiB whiskers that are formed by hot iso-static pressing of different proportions of Ti and TiB_2 powders. It was found that at low volume fraction of TiB (0.3), the whiskers are randomly oriented thin needle shaped ones with high aspect ratios. As the volume fractions are increased (0.92), the TiB whiskers became

even finer with whisker diameters approaching 10 nm.

The crystal structures of the two titanium borides, TiB and TiB_2, are based on the same building block which is a trigonal prism.[91] A boron atom lies at the center of the trigonal prism having six titanium atoms at the corners, as shown in Figure 2.15 (a). The B27 structure of TiB consists of columnar arrays of triangular prisms sharing only two of their three rectangular faces with the neighboring prisms, as illustrated in Figure 2.15 (c). This stacking leads to the formation of a zig-zag chain of boron atoms along the [010] direction as shown in the Figure 2.15 (c). The rhomboid shaped cross sectional area in the figure is the boron-free pipe of titanium formed when these prisms of TiB are connected at the edges. The projection of TiB structure on the (010) plane is shown in Figure 2.15 (e). On the other hand, the C32 structure of TiB_2 is formed by the vertical stacking of prisms in a closed packed array. Here the alternate planes of Ti and B are formed by stacking the trigonal prism in such a way that the prisms are sharing all their faces with the neighboring prisms as depicted in Figure 2.15 (b). The (0001) projection of the C32 structure is shown in Figure 2.15 (d). Table 2.3 summarizes the crystal structures, lattice parameters and fractional co-ordinates of atoms in TiB and TiB_2.

Previous research has documented the orientation relationship between TiB and α-Ti, β-Ti and TiB_2. Hyman et al.[96] reported the following two orientation relationships between TiB and α-Ti,

$$(010)_{TiB} \| \{1\bar{2}10\}_{\alpha} \quad ; \quad \langle 001 \rangle_{TiB} \| [10\bar{1}\bar{1}]_{\alpha}$$

$$(010)_{TiB} \| \{11\bar{2}0\}_{\alpha} \quad ; \quad \langle 001 \rangle_{TiB} \| [0001]_{\alpha}$$

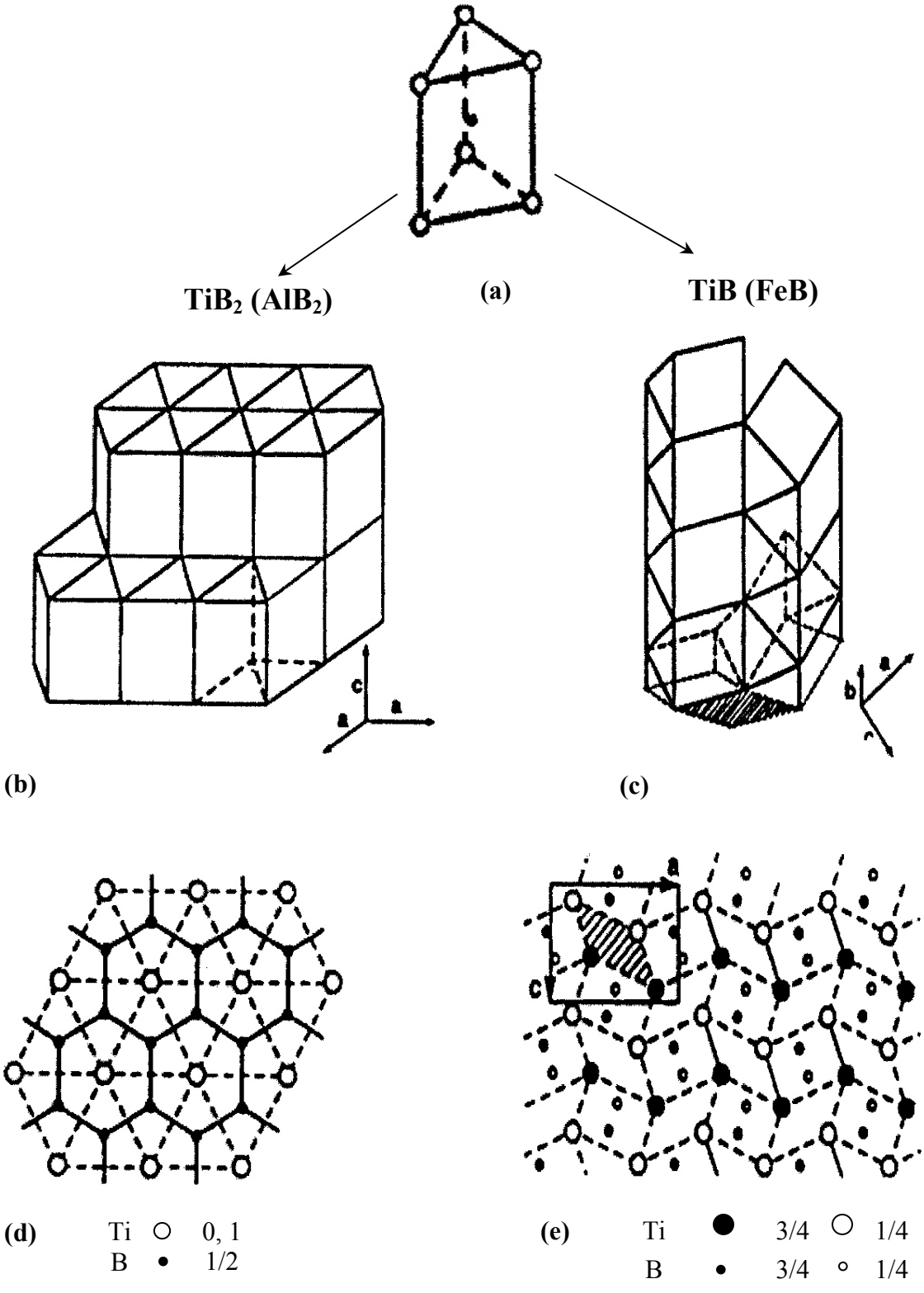

Figure 2.15 Crystal structures of TiB_2 and TiB (Adapted from [91])

Table 2.3 Crystal structure, lattice parameter and fractional coordinates in TiB and TiB_2 (Adapted from [91])

Phase	Structure / Space group	Unit Cell	Atomic positions
TiB	Orthorhombic / P_{nma}	a = 6.12, b = 3.06, c = 4.56	Ti: 4c,m, x = 0.177, y = 1/4, z = 0.123 B: 4c,m, x = 0.029, y = ¼, z = 0.603
TiB_2	Hexagonal / $P_{6/mmm}$	a = 3.03, c = 3.23	Ti:1a, 6/mmm, x = 0, y = 0, z = 0 B: 2d, 6m2, x = 1/3, y = 2/3, z = 1/2

Fan et al.[97] also reported that the same orientation relationship exists between TiB and α-Ti. The direction of the TiB whisker along the B-chain, [010], is always parallel to the closed-packed direction of α-Ti, $\langle 11\bar{2}0\rangle_\alpha$, in the basal plane. However, the TiB whisker can grow parallel to any of the three $\langle 11\bar{2}0\rangle_\alpha$ directions, thereby giving rise to three possible variant directions of TiB in α-Ti matrix. The orientation relationships between TiB and β-Ti are,[94]

$$(100)_{TiB} \parallel (100)_{\beta\text{-}Ti;} \qquad [010]_{TiB} \parallel [010]_{\beta\text{-}Ti}$$

$$(100)_{TiB} \parallel (110)_{\beta\text{-}Ti;} \qquad [010]_{TiB} \parallel [001]_{\beta\text{-}Ti}$$

$$(100)_{TiB} \parallel (112)_{\beta\text{–}Ti;} \qquad [010]_{TiB} \parallel [111]_{\beta\text{-}Ti}$$

TiB exhibits three specific orientation relationships with β-Ti. Li et al.[98] showed that the TiB/β-Ti interface along $[010]_{TiB} \parallel [111]_{\beta\text{-}Ti}$ is parallel to $(100)_{TiB} \parallel (112)_{\beta\text{-}Ti}$. The

TiB/β-Ti interface is smooth, sharp, and free from any interfacial phase. Prangnell et al.[99] reported orientation relationships between TiB and TiB_2 as:

$$[001]_{TiB} \left\| \left\langle 11\bar{2}0 \right\rangle_{TiB_2} \right. \quad \text{and} \quad [100]_{TiB} \left\| [0001]_{TiB_2} \right.$$

The long, needle shaped morphology of TiB whiskers is considered to be the result of B diffusion along the $[010]_{TiB}$ direction.[97] The relatively faster diffusion along the $[010]_{TiB}$ direction is attributed to the continuous B-B bond in this direction. It has also been reported that the diffusion along the [010] longitudinal direction of TiB is about 10 times higher than the other transverse direction leading to a needle shaped morphology of the TiB whiskers.[97] Although no detailed B diffusion studies have been performed in TiB, Schmidt et al.[100] have performed isotropic diffusion studies using ^{10}B isotope in TiB_2. They reported that the B self-diffusivities in TiB_2 were of the order of $10^{-19} - 10^{-23}$ m^2/s in the temperature range 800–1200 ˚C. The author also pointed out the possibility of large error (60-80%) associated with the B diffusivities in this study which may be for two reasons. First, a relatively rough incoherent surface makes it difficult to make precise diffusivity measurements. Second, because of the small penetration depth of the diffusion profile (<500 nm), large error might have resulted in the diffusivity calculations when the diffusion profile is compared with the tracer isotope distribution prior to the diffusion anneal. From the perspective of boride coatings growth on titanium, diffusivities of B in TiB and TiB_2 at a particular temperature would determine the overall coating thickness obtainable at that temperature. Fan et al.[97] reported the approximate diffusion coefficients of B in TiB and TiB_2 at 870 °C and 970 °C as 87.59×10^{-16} m^2/s, 438.8×10^{-16} m^2/s and

1.91×10^{-16} m^2/s, 9.31×10^{-16} m^2/s, respectively. B diffusivities in TiB_2, reported by Fan et al., are a few orders of magnitude higher than those reported by Schmidt et al. This may be due to the error associated with the diffusivity calculations by Schmidt, as pointed out by the author.

2.3.4 Titanium boride coatings on titanium

Several techniques such as high energy electron beam irradiation, laser boriding, and pack cementation have been used to create boride layers on titanium. Kwangjun et al.[101] used high energy electron beam irradiation to create TiB rich surface layers on Ti-6Al-4V alloy using MoB and TiB_2 powders. Laser boronizing technique has also been used to modify the surface layers of CP-Ti, Ti-6Al-4V and Ti-4Al-2Sn-4Mo substrates.[102] The author performed both laser and pack boriding experiments on the above mentioned alloys for comparison of these two processes. The laser boriding in these alloys produced TiB_2 layer thickness in excess of 150 μm while pack boriding created only about 70 μm of boride layer thickness. There are some interesting observations that can be made from this research. It was reported that the laser boriding of Ti alloys produced only the TiB_2 layer, and no TiB layer formation was observed. But the conventional pack boriding process generally produces a dual layer consisting of TiB_2 and TiB or a single layer of TiB depending on the powder composition. Also the existence of TiN layer next to the TiB_2 layer was also witnessed in this research. Generally, laser boriding is associated with high capital cost requiring sophisticated equipment compared to that of pack boriding where capital investment is minimal.

Aich et al.[103] performed experiments to grow titanium boride coatings on titanium using the pack cementation method. The coating formed was mainly of TiB; no TiB_2 was

observed. The powder mixture used consisted of boron, sodium carbonate, and carbon. In this study, the TiB coating thickness obtained was ~30 μm for 24 hours treatment time at 800 ˚C. Tikekar et al.[104] used similar pack cementation method for boriding CP-Ti and Ti-6Al-4V alloy, but with a different composition of the powder mixture involving boron, sodium borate, and calcium powders. The results obtained are different from that of Aich et al. in the sense that a dual layer of TiB and TiB_2 formed on the titanium substrate. Boriding was done in both α-phase field (850 ˚C) and β-phase field (950 and 1050 ˚C). It was reported that when borided in β-phase field, the TiB_2 coating thickness (≈ 6.4 μm at 950 ˚C and 17 μm at 1050 ˚C) was more than that in the α-phase field (≈ 3.9 μm at 850 ˚C). The total coating thickness (TiB + TiB_2) obtained was maximum at 1050 ˚C when borided for 24 hours (≈ 54 μm). A very interesting observation was that upon boriding titanium very close to the α to β transition temperature (900 ˚C) for 24 hours, the coating thickness obtained was the highest (≈ 60μm) relative to all other treatment conditions. This suggested that the diffusion of boron in titanium at temperatures close to the transition temperature may help to increase the depth of penetration of TiB whiskers. Theoretically, CP-Ti (grade-2) undergoes α to β phase transition at around 913 ˚C. It is intriguing if there is an enhancement of boron diffusion in titanium or in TiB near the transition temperature akin to the enhancement of Ti self-diffusion near the phase transition temperature. If so, then this could be useful in maximizing the coating thickness. One of the major objectives of this research is to see if we can obtain a deeper boride coating in titanium on the basis of this unusual self-diffusion in titanium.

2.4 Cyclic thermal treatments on metals

Cyclic thermal treatment (CTT), Chemicothermocycling treatments (CTCT) and Thermo mechanical treatments (TMT) are some unusual treatments that have been employed to alter the microstructure and enhance the mechanical properties of various metals and alloys. All such processes are termed *nonisothermal* processes because the treatment temperature varies with time. The variation of temperatures with time is mostly periodic. A nonisothermal process is characterized by four important parameters: i) the choice of upper and lower hold temperature (generally termed as terminal temperatures), ii) hold times at the terminal temperatures, iii) the heating and cooling rates during cycling, and iv) the total exposure time. Each of these parameters has a key role in achieving the final properties in the material. In the following, a brief account of the applicability of the nonisothermal processes as employed in various fields of metallurgy as well as the role of phase transformation on such processes is presented.

2.4.1 Cyclic surface treatment

CTT processes are employed in metals and alloys to alter both surface and bulk properties. Previous research demonstrated that compared to isothermal processes, cyclic thermal processes are much faster.[105, 106] For example, Gyulikhandanov et al.[105] performed cyclic as well as isothermal carburizing experiments on steels and reported that the thickness of the carburized layer achieved by cycling is more than twice that achieved by isothermal treatment for the same saturation time. It was also reported that the growth kinetics of the carburized layer during the cyclic treatment was enhanced by increasing the hold time at the upper terminal temperature of the thermal cycle and the number of thermal cycles. A long duration hold at the lower terminal temperature of the

cycle did not bring about any appreciable increase in coating growth. This may be partly due to higher solubility of carbon in γ-iron than in α-iron.

Nesbitt et al.[106] studied diffusional transport of aluminum during cyclic oxidation of Ni-Cr-Al alloy. The author reported a higher oxidation rate in this alloy during cyclic oxidation, forming a protective Al_2O_3 coating. Rolinski [107] conducted cyclic plasma nitriding in titanium alloys across 930 and 730 ˚C with a hold time of 1 hour at both terminal temperatures for a total exposure time of 9 hours. Isothermal nitriding treatments were also done at 730 and 930 ˚C for 9 hours to compare with the results of the cyclic thermal treatments. The nitride coating thicknesses in isothermal hold at 730 and 930 ˚C were about 1 and 5 μm, respectively. The cyclic treatments resulted in coating thickness of 3-4 μm, slightly lesser than that of isothermal condition at 930 ˚C. The reason for obtaining lesser coating thickness during cyclic nitriding may be because of the choice of the upper terminal temperature. The upper limit temperature (930 °C) lies in the α+β phase field for the alloys that were used for this study. Hence, a hold at this temperature does not ensure complete phase reversal upon thermal cycling which seems to be important for such processes. Solubility of interstitial elements like N is more in β-Ti than in α-Ti.[108] So, ingress of N will be more in β-Ti phase at the upper terminal temperature and the dissolved N will precipitate out and will form nitride compound (TiN or Ti_2N) during cooling to the α-Ti phase due to the solubility difference. Haanappel et al.[109] conducted cyclic oxidation experiments on Ti-48Al-2Cr alloy and reported a faster oxidation rate in cyclic conditions compared to the isothermal one.

2.4.2 Cyclic heat treatment for microstructure refinement

Cyclic heat treatments have also been explored in other areas of materials science, for example to accelerate sintering of powders or to refine grain size in metals and alloys. Grain size refinements by cyclic heat treatments have been reported in a number of research studies.[110-112] Prior austenitic grain size was refined by cycle heating treatment across austenite and martensite phase fields in Fe-15Ni-5-30Cr-5-10Mo-0-2Ti alloy.[113] Reduction of grain size from 1 mm to about 50 μm was achieved by thermal cycling across the austenite and ferrite phase fields. Ramesh et al.[114] carried out cyclic grain refinement treatments in Fe-0.2C-10Cr-1Mn alloy steel and reported the average grain size as 80 μm after cycling compared to the 150 μm grain size before cycling. When this alloy was subjected to thermo-mechanical treatments at or slightly above recrystallization temperature, dynamic recrystallization brought about a substantial refinement in grain size to about 48 μm. Wang et al.[115] showed that a very coarse lamellar structure (1-3 mm) in Ti-Al alloys can be reduced to a fine one (10-20 μm) by cyclic heat treatment.

2.4.3 Role of phase transformation in cyclic thermal treatment

Solid state phase transformation is commonly exploited to control the microstructural and mechanical properties of metals and alloys. Solid state transformations during CCT have shown improved kinetics in many metallurgical processes, like recrystallization, grain growth, and grain refinement[116-119] over isothermal conditions. Sista et al.[119] investigated the effect of cyclic processing on austempering kinetics of 1080 steel as against the conventional (isothermal) processing. It was reported that when the isothermal austempering was done at 260 and 300 ˚C, it took 160 and 140 minutes, respectively, for complete bainitic transformations. But when austempering was

done cyclically between 260 and 300 ˚C, the bainitic transformation was completed in 32 ± 4 minutes. Sahay et al.[116] observed accelerated grain growth during cyclic annealing of cold rolled steel (0.05% C, 0.05% Al, 45ppm N, Al-killed). The average grain size of this steel obtained when cyclically annealed between 650 and 725 ˚C for a total of 6 hours (~19 μm) was larger than that obtained by isothermal holds at both the terminal temperatures (~14 μm at 650 ˚C and ~16 μm at 725 ˚C) for the same amount of hold time. The authors suggested that the enhanced grain growth kinetics in cyclic treatment is due to reduction of the activation energy for atom movements. Nonisothermal excitation increases the free energy of the atoms in the grains and thus reduces the activation barrier increasing the probability of atomic jumps.

A significant increase in the densification rate in metal powders was achieved by cyclic phase transformations.[117, 120-123] Schuh et al.[117] conducted experiments on compaction of zinc powders, under both isothermal and cyclic thermal conditions. The densification during cycling occurred much more rapidly than during the isothermal process, despite the fact that the average temperature during cycling was almost 150 ˚C lower than that of the isothermal treatment. Hausner[120] found that when electrolytic iron powder is cyclically sintered through the α-γ phase transition temperature, there was a considerable shrinkage in the diameter of the material. Choi et al.[121] also reported an enhanced sintering rate of Fe-Ni alloy powder when cycled through the α-γ phase transformation temperature. Kohara[122] investigated sintering of iron powder under repeated allotropic transformation through α-γ phase under small compressive load and reported substantial improvement in the sintering rate. Misra et al.[123] also witnessed an activated sintering rate in aluminum powder under thermal cycling conditions. It was

observed that cyclic sintering of aluminum powder in vacuum ($3-5\times10^{-3}$ Torr) between 600-660 ˚C with a cycle period of 3 minutes resulted in complete densification within 1 hour of treatment. On the other hand, isothermal sintering at 660 ˚C took more than 1 hour for partial sintering of powders.

2.5 Diffusion and phase transformation in titanium

Group IV transition metals, specifically Ti, Zr and Hf, have been found to exhibit anomalous diffusion behavior.[21, 22] The "anomalous" diffusion here refers to elevated diffusion rates, relative to the normal Arrhenius type behavior. The elevated diffusion rates have been found to occur within a few tens of degrees above the phase transition temperature (β-transus) of HCP metals. Generally, the self diffusion in metals is described by the simple Arrhenius type relationship:

$$D(T) = D_0 \exp(-Q/RT) \tag{2.22}$$

where, the pre-exponential factor D_0 and activation energy Q are assumed to be independent of temperature. R, T are the gas constant and the absolute temperature respectively.[21] In general, for metals, the value of D_0 is between 0.05 and 5 cm^2/s. The magnitude of Q is generally found [21] to be proportional to the melting point of the metal as,

$$Q = 34\ T_m \tag{2.23}$$

Since the late 1950s, the existence of anomalous diffusion behavior in some metals, characterized by a strong curvature in their Arrhenius plots (ln D vs 1/T), has

been found.[21] In particular, Group IV transition metals, specifically Ti, Zr and Hf, have been found to exhibit the anomalous diffusion behavior. For example, Ti shows normal Arrhenius type temperature dependent diffusion behavior at high temperature, but as the temperature approaches the β to α phase transition temperature, it shows anomalously high self-diffusivity. This is illustrated qualitatively in Figure 2.16 (a), showing the upward curvature of the diffusivity curve as the phase transition temperature is approached.[124] Figure 2.16 (b) shows the experimentally measured self-diffusivities in some of the BCC metals plotted as a function of the reduced temperature along with some of the transition metals.[125] The figure clearly shows that in Ti, near the phase transition temperature, the self-diffusivities are about three orders of magnitude higher than in normal BCC metals.

It is to be noted that all metals that show anomalous diffusion behavior also present allotropic phase transformation.[126] The anomalous diffusion behavior is also reported to be exhibited by BCC Hafnium,[127] γ-uranium,[128] ε-plutonium,[129] and rare-earth elements like δ-cerium,[130] γ-ytterbium,[131] and γ-lanthanum.[132]

Several researchers have tried to explain the anomalous behavior. Claire [21] cited that there could be two or more diffusion mechanisms operating in the anomalous regime (quoted in [21]). Accordingly, the anomalous diffusion behavior was suggested to be of the form:

$$D = A_1 \exp(-Q_1/RT) + A_2 \exp(-Q_2/RT) \qquad (2.24)$$

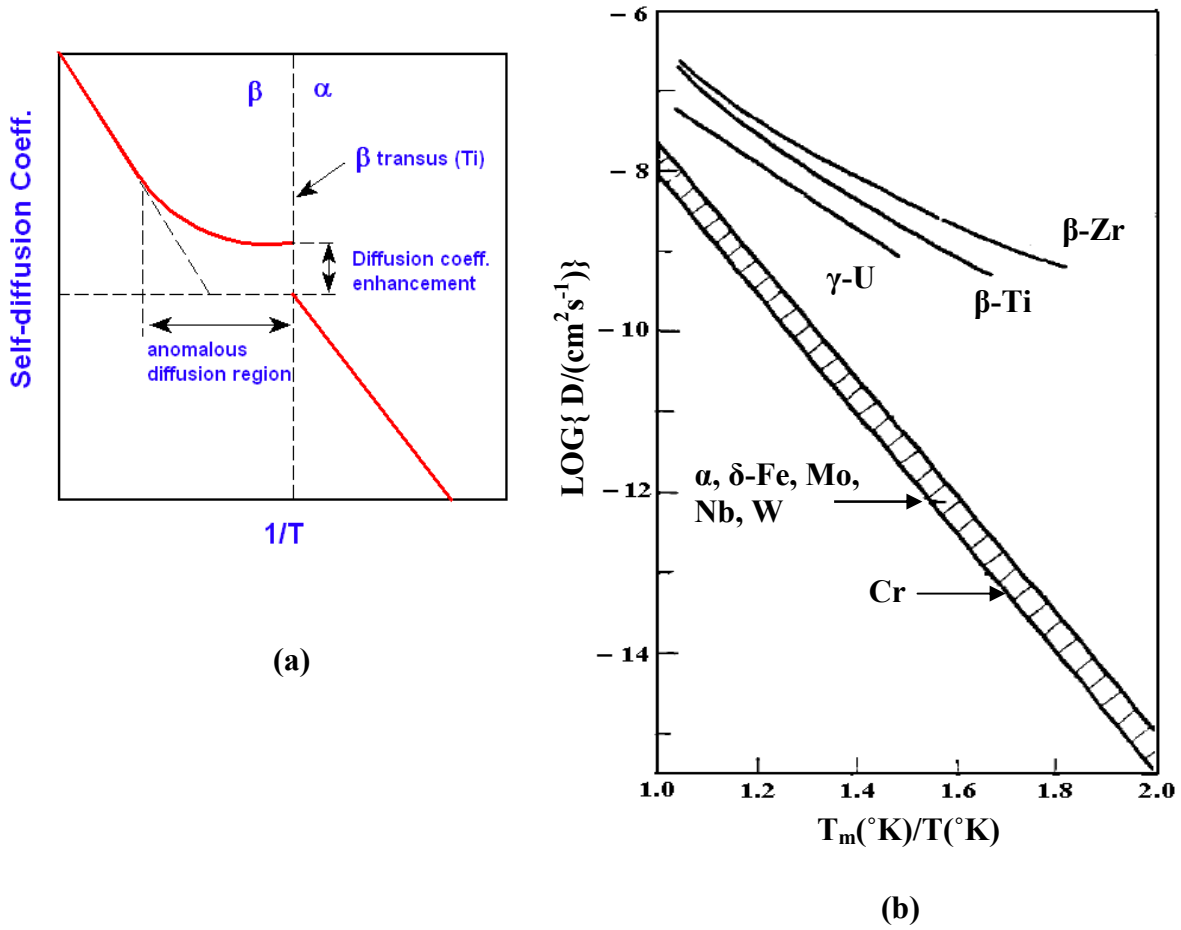

Figure 2.16 Arrhenius plot **(a)** of self-diffusivity for CP-Ti showing upward curvature as the transition temperature is approached [124]. Comparison of experimentally measured self-diffusivities **(b)** of various normal BCC metals and anomalous metals like Ti, Zr etc. [125].

The first term in the right hand side of the Eqn. (2.24) refers to the regular self-diffusion mechanism away from the phase transition temperature. The experimentally determined values for A_1, Q_1, A_2 and Q_2 for β-Zr, β-Ti and some Ti-alloys are tabulated in Table 2.4. The A_1 values for self diffusion in β-Zr and β-Ti are well inside the commonly encountered range, and the activation energies, Q_1 values are also within the limits of melting point correlation. The second term in the right hand side of the equation corresponds to the contribution from the other possible diffusion mechanisms that might be operating in these metals near the phase transformation temperature. The diffusion coefficient arising from this second term is characterized by an activation energy (Q_2) that is half of that of the bulk diffusion (Q_1) and pre-exponential factor (A_2) about two orders of magnitude smaller than that of bulk diffusion (A_1). This trend is observed for all the metals listed in Table 2.4.

Table 2.4 Activation energy and pre-exponential factor for pure Zr, Ti and Ti-alloys (Adapted from [21])

Metal	**A_1 (cm^2/sec)**	**Q_1 (Kcal/mol)**	**A_2 (cm^2/sec)**	**Q_2 (Kcal/mol)**
β-Zr	1.34	65.2	8.5×10^{-5}	27.7
β-Ti	1.09	60.0	3.58×10^{-4}	31.2
Cb in Ti	20	73	5×10^{-3}	39.3
Mo in Ti	20	73	8×10^{-3}	43.0
Cr in Ti	4.9	61	5×10^{-3}	35.3
Mn in Ti	4.3	58	6.1×10^{-3}	33.7
Fe in Ti	2.7	55	7.8×10^{-3}	31.6
Co in Ti	2.0	52.5	1.2×10^{-3}	30.6
Ni in Ti	2.0	52.5	9.2×10^{-3}	29.6

Several possibilities have been put forwarded to help explain the second term in Eqn. 2.24,

1. The second term may result from some intrinsic, lattice diffusion mechanisms operating in these metals, such as interstitial diffusion or may be divacancies or some unrecognized mechanisms.[22] But this theory was refuted on the grounds that a very small pre-exponential factor was obtained which corresponds to negative activation entropies. Table 2.4 lists those extremely small values of the pre-exponential factor, A_2. Normally, diffusion studies in all materials show relatively higher pre-exponential factor corresponding to positive entropy.[120]
2. The second term may come as a contribution from the grain boundary diffusion. But this hypothesis was rejected on the basis that experiments with these metals were done in polycrystalline samples with fairly large grains. With lesser grain boundary areas, the probability that the contribution to the enhanced diffusivity coming from such diffusivity paths was negligible, as suggested by these authors.[133, 134]
3. Another possibility is that the second term contribution may come from diffusion through dislocation. However, to justify the anomalous diffusion data, an unrealistic amount of dislocations ($10^{10}/cm^2$) needed to be present in the material. Given that the diffusion experiments were done in well annealed samples, the possibility can be easily ruled out.[126]
4. Kidson[135] proposed anomalous diffusion as an extrinsically-enhanced self diffusion mechanism brought about by impurities. The argument is based on the association

of vacancies with some impurities such as O or N present in the metal. At a relatively low temperature, there would be excess vacancy concentrations due to the rapidly diffusing interstitial species bringing about appreciable enhancement in self-diffusion. A high binding energy of the order of 30 Kcal/mol in the impurity-vacancy complex is needed to support this hypothesis.

The anomalous diffusion behavior can also be examined from the phase transformation point of view. The significantly low activation energy for diffusion in the HCP metals may arise from the polymorphic transition.[22, 136] Group IV transition metals undergo phase transformation from high temperature BCC phase to low temperature HCP phase during cooling. The fact that an anomalous diffusion mechanism is operative in the proximity of the phase transition temperature suggests some influence of phase transformation on diffusion may exist. Also, it is known that there is the formation of a metastable hexagonal (not closed packed) phase, known as ω-phase in Ti, Zr and Hf upon alloying[137] or under pressure.[138] It is important to note that these ω-structures are observed at room temperature only in alloys of Ti, Zr and Hf, but not in the pure form of these elements. On the other hand, ω-structural fluctuations appeared in Zr-Nb alloy over 1000 ˚C near the β→α transition temperature where the anomalous diffusion is operative.[136, 139, 140] One of the reasons for not being able to observe the ω-phase in pure Ti, Zr and Hf, as argued by the authors, [126] may be the absence of any BCC (β) phase-stabilizing element. It might be necessary to have some β stabilizing element to suppress the HCP (α) phase field to detect the ω-phase fluctuations near the polymorphic transformation temperature by conventional diffraction techniques.

2.5.1 Mechanism of anomalous diffusion

Sanchez et al.[126, 141] proposed a phenomenological model for anomalous diffusion in ω-forming systems. This model is based on the formation of localized ω-like structural fluctuations, near (and above) the transformation temperature. The phenomenological model distinguishes the mechanism of formation of these ω-embryos from those of the activated complexes for diffusion, although the final structures for both are the same. The ω-embryos are formed when two neighboring (111) planes in the BCC lattice collapse to the intermediate position leaving every third (111) plane unaltered. The formation of the ω-embryo involves the co-operative movements of atoms whereas an activated complex does not do so. This can be illustrated with the help of Figure 2.17. The activated complex will form upon displacement of the central atom at O by a distance of $a/2\sqrt{3}$ ('a' being the lattice parameter) along the <111> direction of the BCC lattice as shown in Figure 2.17 (a). This displacement will lead to the collapse of the central atom to the nearest (111) BCC plane as indicated by the ABC triad in Figure 2.17 (a). Figure 2.17 (b) shows the structure thus formed by this collapse where the central atom forms trigonal bonding with its neighboring atoms in the collapsed plane. On the other hand, the ω-embryo is formed inside a BCC lattice upon displacing the atom at O by $a/4\sqrt{3}$ in the <111> direction towards the ABC plane, while the atoms at ABC planes are displaced by the same distance, $a/4\sqrt{3}$, but in the opposite direction. Such displacements lead to the collapse of those planes into a single plane at the intermediate position of those two planes along the <111> direction. It can be noted that the final structure formed in the collapse plane will be the same as that of the activated complex shown in Figure 2.17(b).

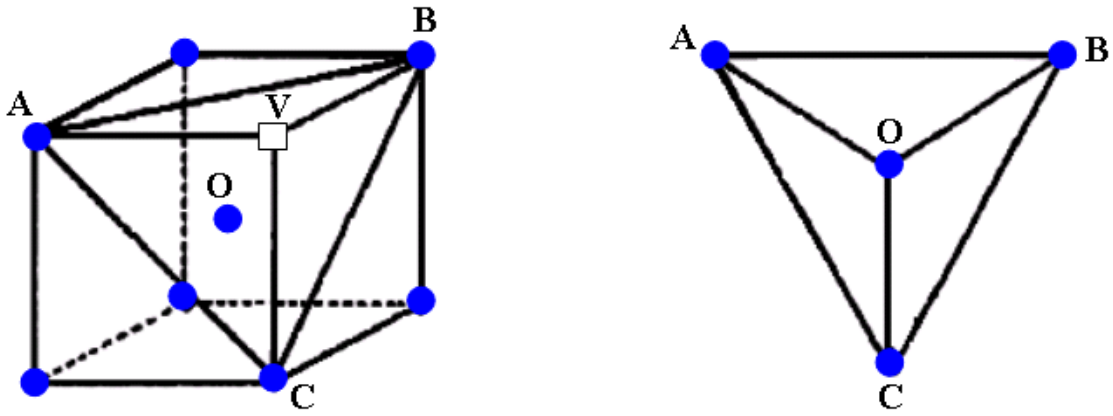

(a) **(b)**

Figure 2.17 BCC lattice **(a)** showing the ABC(111) plane with the body-centered atom at O and vacancy at V. Atom at O collapsed at ABC triangle **(b)** thereby forming ω-embryo or activated complex (Adapted from [126]).

The distinguishing factor between these two structures is the mechanism by which they form. The collapse plane will have the hexagonal (but not closed pack) symmetry and will represent the basal plane for the ω-embryo. When each lattice point of the BCC (β) crystal is displaced by a magnitude either 0, $a/4\sqrt{3}$ or $-a/4\sqrt{3}$ ('a' being the lattice parameter) along a given <111> direction, ω-phase is formed inside the lattice. Since there are three different variants of (111) planes of α, β and γ stacking sequence of BCC lattice, three variants of ω-structure can be obtained.[126] The authors pointed out that the collapse of <111> planes to form the ω-structure decreases the free energy of the system and helps the atom in the BCC lattice to migrate to the nearest neighbor vacancy with least expense of energy as illustrated in Figure 2.17 (a). When an atom at O tries to migrate to a neighboring vacancy at V, it has to overcome two successive saddle point configurations. These triangular saddle points are located at one-third and two-thirds of

the jumping distance along <111> direction of the BCC lattice. Upon the formation of the ω-embryo by the collapse of the two neighboring (111) planes, i.e., planes through the atom at O and the ABC triad, the diffusing atom O is already at the first saddle point. Hence the probability of the atom at O to complete the jump to the vacant site increases. As the transition temperature is approached, the concentrations of these ω-embryos increase, resulting in an appreciable increase in diffusion coefficient. On the other hand, when the temperature is increased further, random thermal vibrations tend to destroy these ω-embryos and thus diffusion behavior becomes normal as that in other metals. Following an approximate expression incorporating the configuration energy and entropy of BCC system, originally derived by Kikuchi,[142] Sanchez [126] showed that the free energy of the system goes down due to the formation of ω-phase close to the transition temperature.

Following the Sanchez formulation, the total diffusion coefficient is given by,

$$D = D_N + D_\omega \tag{2.25}$$

where, D = total diffusion coefficient, D_N = diffusivity arising from the normal activated complexes, D_ω = diffusivity arising from the ω-embryos. The first term on the right hand side of the above equation can be written as,

$$D_N = D_0 \exp\left(\frac{-Q}{RT}\right), \tag{2.26}$$

where, D_0 = pre-exponential factor, Q = activation energy, T = temperature and R= gas constant. The contribution to the total self-diffusivity arising from the ω-embryos can be written as,

$$D_\omega = \gamma a^2 c_v \Gamma_\omega \tag{2.27}$$

where, γ = numerical constant close to unity, a =BCC lattice parameter, c_v = equilibrium concentration of vacancies and Γ_ω = jump frequency. Γ_ω is defined as,

$$\Gamma_\omega = \upsilon_0 c_\omega \tag{2.28}$$

where υ_0 is the Debye frequency of vibration of atoms (~ 10^{13} for most metals) and c_ω is the concentration of ω-embryos. The concentration of vacancies can be written in terms of the corresponding enthalpy (ΔH_f) and entropy (ΔS_f) of formation. Also noting that υ_0 is the same for both ω-embryos and the normal activated complex,[126] the overall diffusivity in equation 4 can be written as,

$$D = D_0 \exp(\frac{-Q}{RT}) + D_0 \exp(\frac{-\Delta S_m}{R}) c_\omega \exp(\frac{-\Delta H_f}{RT}) \tag{2.29}$$

where, D_0 and Q are given by,

$$D_0 = \gamma a^2 \upsilon_0 \exp\left[\frac{(\Delta S_m + \Delta S_f)}{R}\right] \tag{2.30}$$

$$Q = \Delta H_m + \Delta H_f \tag{2.31}$$

In Eqns. (2.30) and (2.31), ΔH_m and ΔS_m are the enthalpy and entropy of vacancy motion, respectively. All other terms except c_ω, in Eqn. (2.29), are classical quantities and hence can be determined independently or obtained from the literature. The pre-exponential term, D_0, always appeared to lie between 0.05 to 5 cm^2/sec, and the activation energy is correlated to the melting point (Eqn. 2.23) rather in a straightforward manner.[21] The enthalpies of vacancy formation (ΔH_f) and vacancy motion (ΔH_m) are of the order of one half of Q.[21] ΔS_f and ΔS_m are the respective vacancy formation and migration entropies. For most normal metals, ($\Delta S_m/R$) is a positive quantity that lies between 1 and 5.[21] Sanchez[126] formulated the temperature dependence of this non-classical term, $C_{w,}$ based on the cluster variation (CV) approximation method and thereby predicted the total self-diffusivities of zirconium. A reasonable agreement between the experimental and the predicted values was obtained. Figure 2.18 shows the increase in concentrations of ω-embryos as $\beta \rightarrow \omega$ transition temperature is reached.

It is quite likely that anomalous diffusion behavior in Ti will influence B diffusion in Ti, especially at temperatures very close to the phase transition temperature. If this anomalous diffusion can be exploited to obtain a much deeper coating in titanium, then this would be a very interesting development. Further, any understanding that can be gained with respect to anomalous diffusion near the phase transition temperature can help with respect to thermal cycling of metals and coatings.

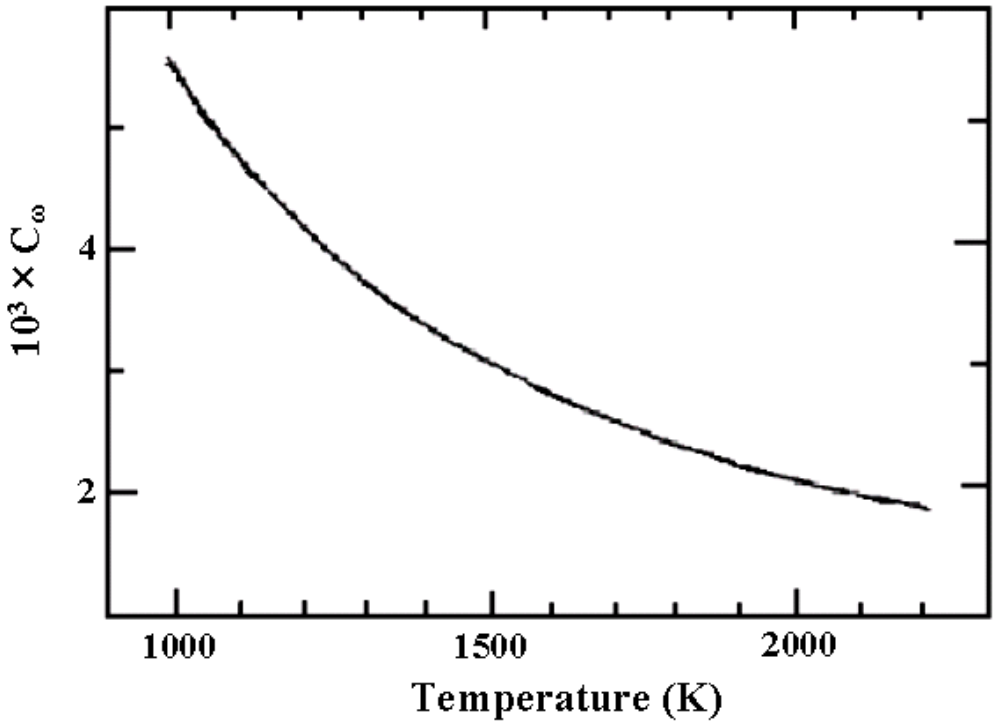

Figure 2.18 Concentrations of ω-embryos vs. temperature (Adapted from [126])

CHAPTER 3

OBJECTIVES

3.1 Objectives of the present research

The general objective of this research is to develop methods that can result in accelerated kinetics of boride layer growth on the surface of Ti. Two approaches were employed for this process.

First, on the basis of anomalous diffusion in HCP metals near the phase transition temperature, the hypothesis is that this anomalous B diffusion can lead to rapid ingress of B and it can lead to increased depths of boride layers. The key objectives are the following.

1. To perform isothermal B diffusion experiments close to the phase transition temperature in Ti. The resulting boride layer coating thicknesses are to be determined using optical and SEM microscopy techniques. The thicknesses are to be compared with the layer thicknesses obtained by isothermal B diffusion away from the transition temperature in order to demonstrate any significant effect. For comparison, the effect of isothermal B diffusion in the α, β and the α + β field for long hold periods on the boride layer growth kinetics are also to be investigated.
2. To identify, if any, the mechanism responsible for the enhanced B diffusion in Ti near the transition temperature. This would result in the accelerated boride layer growth.

3. To develop a theoretical model that can explain the growth behavior of boride layers near the transition temperature taking into account of the simultaneous boron diffusion within the boride and Ti-phases.

The second hypothesis is that by cyclically changing the surface temperature during B diffusion a heat-packet, which travels back and forth from the surface to interior, can be utilized to transport more B into bulk than is possible by conventional methods. The key objectives to verify this hypothesis are,

4. To carry out thermal cycling B diffusion experiments across the α/β transition temperature in Ti with various hold periods at the limit temperatures and for a varied number of cyclic thermal reversals.
5. To determine the resulting boride layer thicknesses by optical and SEM microscopy techniques and to compare the kinetics of growth with that obtained by the isothermal B diffusion method.
6. To formulate the subsurface temperature distribution profiles in Ti as induced by the cyclic temperature fluctuations at the surface during thermal cycling.
7. To investigate the mechanism of B transport into subsurface region by the repeated heat-packet travel caused by the surface temperature fluctuations and its effect on diffusion and supersaturation of B.

CHAPTER 4

EXPERIMETAL PROCEDURE

4.1 Powder mixture for B diffusion process

The powder mixture used for boriding experiments is comprised of three components: a compound as a boron source, a low melting compound, and a scavenger compound. A solid state boron source can exist either in crystalline or amorphous form. An amorphous boron source was chosen over a crystalline one because of its finer particle size and larger specific surface area (24 m^2/g for amorphous vs. <1 m^2/g for crystalline boron).[80] Finer amorphous boron particles will ensure higher reactivity and larger specific surface area will provide a higher dissolution rate to enhance the diffusion process. The second ingredient of the powder mixture is a low melting compound. Usually, solid state diffusion processes are carried out at temperatures > $0.5T_m$, and the second ingredient will be in liquid state at this treatment temperature. The liquid pool will provide easy dissolution and faster diffusion of boron particles within the powder mixture, maintaining a very high boron activity adjacent to the Ti substrate. An appropriate amount of this second ingredient is added to the powder mixture to obtain uniform distribution of the same around the boron source. However, addition of this second ingredient also introduces oxygen to the powder mixture.[104] Ti has strong affinity towards oxygen and forms titanium oxide (TiO_2) on its surface. Moreover, boron can also

react with oxygen to form boric acid (B_2O_3). Hence, in an oxidizing environment, there will be a reduction of boron activity in the powder mixture. Therefore, a third ingredient is added to the powder mixture to prevent the above mentioned reactions from occurring. This ingredient is a scavenging element that will lock the oxygen in the powder mixture by undergoing preferential oxidation over Ti or boron. The scavenging element was chosen based on two criteria: (i) the Gibbs free energy for this element to form its oxide is lower than that of Ti and boron, and (ii) it does not react with Ti.[104] A suitable ratio of these ingredients in the powder mixture (the boron source, the transport medium that forms the liquid pool, and the scavenger element) was used to get the optimum powder pack combination.[104]

4.2 Isothermal boriding near transition temperature

Grade 2 CP-Ti samples (composition in wt. %: 0.3 Fe, 0.17 O, 0.1 C, 0.03 N, 0.015 H, 0.3 max.) were polished using 800 grit SiC paper. A powder mixture,[104] composed of a boron source (amorphous boron, composition in wt.%: 95-97 B, 0.89 Mg, 0.12 water soluble, particle size FN 0.694, from SB Boron Corporation, Bellwood, IL), a transporting medium and an activator were prepared by ball milling the powders for 16 hours. The boriding experiments were done using this powder mixture in a sealed stainless steel crucible. The experiments were carried out for 3, 6, 12, 18 and 24 hours at each of the temperatures: 890, 910 and 915 ˚C. The temperature was controlled within ±3 ˚C, with a thermocouple that was in contact with the powder pack. After the treatment, the samples were removed, sectioned and metallographically polished. Metallographically etched coating structures were examined in optical and scanning electron microscopes (SEM). Coating thickness measurements were made from the SEM

and optical micrographs. The distance from the edge of the sample to the furthest tip of the penetrating TiB whisker is taken as the coating thickness. These measurements were done at 10 equally spaced locations on a micrograph taken at 50X, 100X and 2000X magnifications. Such measurements were done on multiple micrographs and then the average of these measurements was taken as the average coating thickness.

4.3 Isothermal boriding for long hold time

Commercially pure titanium (CP-Ti, Grade 2, Composition in wt. %:0.07 Fe, 0.12 O, 0.007 C, 0.006 N, 0.001 H and bal. Ti) samples were used for this study. The samples were polished till 800 grit surface finish before boriding. Similar experimental procedure was followed as discussed in the previous section. Isothermal boriding experiments were performed for 48 and 71 hours at each temperature of 850 and 1050 ˚C. Boriding at 900 ˚C was done for 3, 6, 12, 18, 24, 48 and 71 hours. The samples were then sectioned, metallographically polished, etched, and examined under optical and scanning electron microscope (SEM). The thicknesses of the TiB_2 and TiB whisker layers were determined by similar method as mentioned in the previous section.

4.4 Thermal cyclic boriding

Cyclic thermal diffusion experiments were performed using the same approach as mentioned above. CP-Ti grade 2 samples with chemical composition in wt. %: 0.3 Fe, 0.17 O, 0.1 C, 0.03 N, 0.015 H, 0.3 max. were thermally cycled between 890-910 ºC (with varying hold time at the limit temperatures) for total thermal exposure times of 3, 6, 12, 18 and 24 hours. The hold time at both limit temperatures were varied as 0, 6, 18, 30, 42 and 60 minutes. Furthermore, thermal cyclic experiments with CP-Ti Grade 2

samples with a different chemical composition (in wt. %:0.07 Fe, 0.12 O, 0.007 C, 0.006 N, 0.001 H and bal. Ti) were also done for 3, 6, 12, 18, 24, 48 and 71 hours of total exposure times across two sets of limit temperatures (one set: between 880 and 920 °C, other set: between 880 and 940 °C). The reason for conducting these two sets of experiments is discussed in detail in the results and discussion section in Chapter 5. A similar approach to that discussed above was implemented for determining the boride layer thicknesses.

CHAPTER 5

RESULTS AND DISCUSSION

5.1 Modeling of layer growth kinetics

5.1.1 Theoretical modeling based on second law of diffusion

The mathematical framework to predict the growth kinetics of the boride layers formed at temperatures above and below the beta transus (β-transus) temperature of Ti is very important both from fundamental and application points of view. There is no prior work on quantitative prediction of the growth of boride layers on Ti. For the growth of multiple compound layers by diffusion, error-function based solutions of Fick's second law can be developed to predict the kinetics.[151, 152] The growth of FeB/Fe_2B layers on Fe during boriding is somewhat similar to the boride layers here. Nearly all the growth of FeB/Fe_2B layers can be explained based on the diffusivity of B alone and assuming that the diffusion of metal component is negligible.[85, 86]

In the present analysis, error-function solutions for the growth of two boride layers during B diffusion are developed. The chemical diffusivity values of B in TiB_2 and TiB (determined from the work of Fan et al. [97]) were used to predict the growth of the two boride layers. In the Ti-B system, TiB_2 is a stoichiometric line compound and TiB has narrow stoichiometric range. Thus, in practice, diffusional growth of these compounds under B concentration gradient does not involve large concentration gradient

within the phases. Nevertheless, the concentration difference between B/TiB_2/TiB layers can be considered to represent the average compositional gradients in the phases.

The development of the error function solutions will be illustrated on the basis of growth of TiB_2/TiB whisker layer on titanium [Figure 5.1(a)]. Three interfaces exist in this system: the B-TiB_2 interface, TiB_2-TiB interface and the TiB-Ti interface. The B concentration profiles across the layers are schematically shown in Figure 5.1(b). The Fick's second law of diffusion, relating the changes in concentration of B with time and location is,

$$\frac{\partial C}{\partial t} = D \frac{\partial^2 C}{\partial x^2} \tag{5.1}$$

where D is the diffusion coefficient and C is the concentration. The development of error function solutions is based on these assumptions: (i) the growth of the dual layer is controlled only by the diffusion of B and the diffusion of Ti in the opposite direction can be ignored, [97] (ii) the diffusion coefficient of B is concentration independent, and (iii) the solubility of B in Ti-matrix is negligible.[23] With these assumptions, the initial and boundary conditions can be written as:

Initial conditions: (t=0)

$$C = C_S \text{ at } x = 0 \tag{5.2}$$

$$C \text{ (in } TiB_2/TiB) = 0 \text{ for } x > 0 \tag{5.3}$$

Boundary conditions: (t>0)

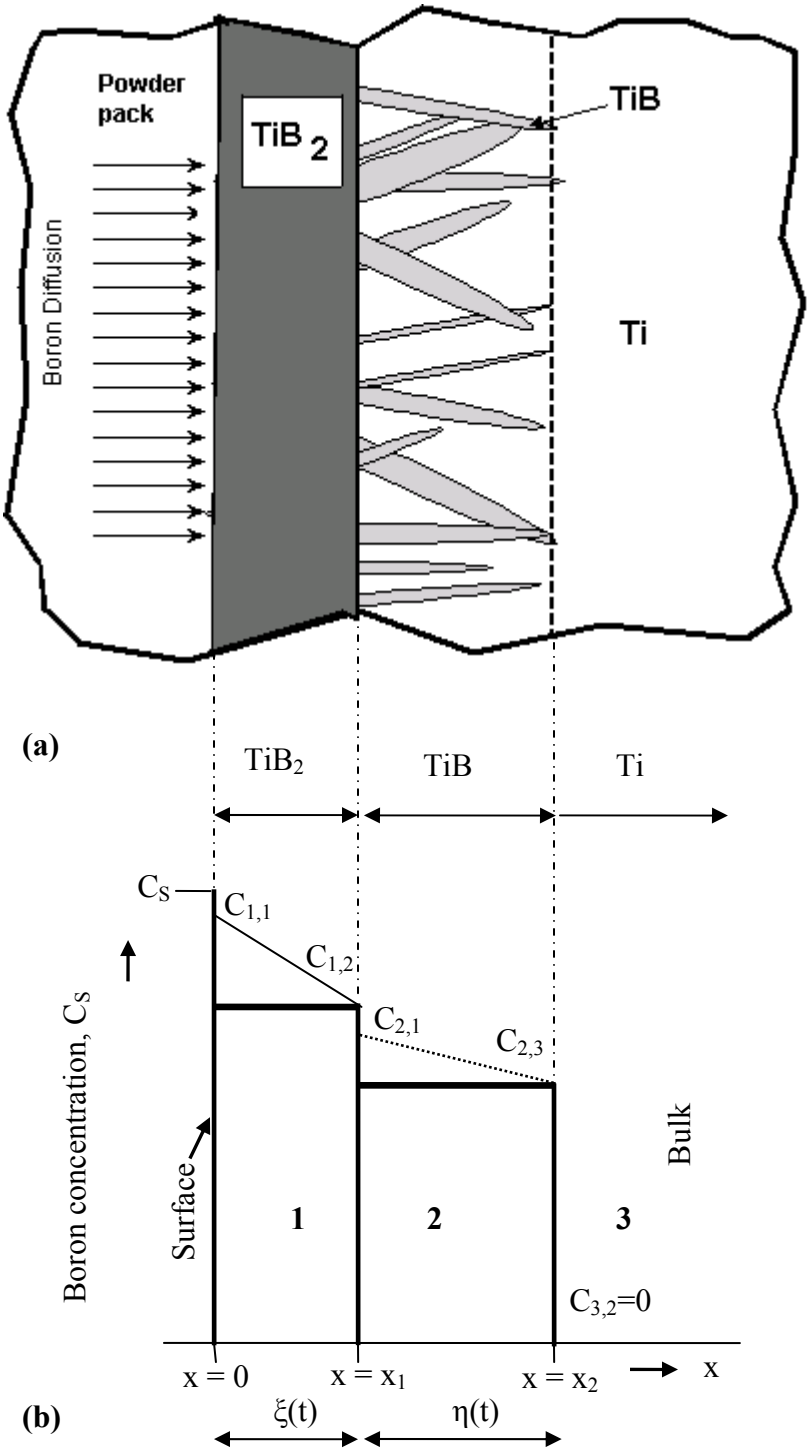

Figure 5.1 Schematic of growth of the TiB_2 layer and the TiB whisker layer **(a).** Concentration profile of B across the layers **(b)**.

$C = C_{1,1}$ = upper limit of B concentration in TiB_2 at the surface (5.4)

$C = C_{1,2}$ = lower limit of B concentration in TiB_2 at the TiB_2/TiB interface (5.5)

$C = C_{2,1}$ = upper limit of B concentration in TiB at the TiB_2/TiB interface (5.6)

$C = C_{2,3}$ = lower limit of B concentration in TiB at the TiB/Ti interface (5.7)

$C = C_{3,2}$ = B concentration in Ti matrix = 0 (5.8)

The general solutions for B concentration in the boride layers and for that in Ti matrix which satisfy Eqn. (5.1) are of the form,[151, 152]

$$C_i(x,t) = A_i + B_i erf\left(\frac{x}{2\sqrt{D_i t}}\right) \tag{5.9}$$

where C_i and D_i are the concentration and diffusivity of B in the respective phase (TiB_2, TiB or Ti). A_i and B_i are the respective constants for each phase which need to be determined from the initial and boundary conditions. Following Wagner approach, [152] the time-independent boundary position for the TiB_2/TiB interface at x_1 are,

$$x_1 = 2\xi\sqrt{D_1 t} \tag{5.10}$$

$$x_1 = 2\xi'\sqrt{D_2 t} \tag{5.11}$$

where ξ and $\xi^{/}$ are the normalized growth parameter for the TiB_2/TiB interface in terms of D_1 and D_2, respectively. Since the growth parameters corresponds to the movement of the same interface, one can write,[152]

$$x_1 = 2\xi\sqrt{D_1 t} = 2\xi^{/}\sqrt{D_2 t} \tag{5.12}$$

Rearranging Eqn. (5.12) yields,

$$\xi^{/} = \xi\sqrt{\frac{D_1}{D_2}} = \xi\phi_1 \tag{5.13}$$

where $\phi_1 = \sqrt{\frac{D_1}{D_2}}$

Similarly, for the TiB-Ti interface, one can write,

$$x_2 = 2\eta\sqrt{D_2 t} \tag{5.14}$$

where η is the normalized growth parameter for the TiB-Ti interface in terms of D_2.

Using Eqns. (5.10), (5.11), (5.13) and (5.14) and incorporating the initial and boundary conditions [(Eqns. (5.2) to (5.7)] in Eqn. (5.9), the variations of concentrations of B in TiB_2 and TiB phases are determined as,

$$C_{TiB_2}(x,t) = C_S - \left(\frac{C_S - C_{1,2}}{erf\xi}\right) erf\left(\frac{x}{2\sqrt{D_1 t}}\right) \tag{5.15}$$

$$C_{TiB}(x,t) = C_{2,1} - \left(C_{2,1} - C_{2,3}\right)\left(\frac{erf\left(\frac{x}{2\sqrt{D_2 t}}\right) - erf(\phi_1 \xi)}{erf\eta - erf(\phi_1 \xi)}\right) \tag{5.16}$$

During the growth of the layers, simultaneous advancement of the TiB_2/TiB and TiB/Ti interface boundaries at x_1 and x_2 in a small time step (dt) will occur because of the accumulation of B atoms at those interfaces driven by the differences in B flux between TiB_2, TiB and Ti phases. Hence, applying the rule of mass conservation at the TiB_2/TiB and TiB/Ti interfaces, one can write,[152]

$$\left(C_{1,2} - C_{2,1}\right)\left(\frac{dx_1}{dt}\right) = -D_1\left(\frac{\partial C_{TiB_2}}{\partial x}\right)_{x=x_1} + D_2\left(\frac{\partial C_{TiB}}{\partial x}\right)_{x=x_1} \tag{5.17}$$

$$\left(\mathrm{C}_{2,3} - \mathrm{C}_{3,2}\right)\left(\frac{\mathrm{dx}_2}{\mathrm{dt}}\right) = -\mathrm{D}_2\left(\frac{\partial \mathrm{C}_{\mathrm{TiB}}}{\partial \mathrm{x}}\right)_{\mathrm{x}=\mathrm{x}_2} \tag{5.18}$$

Differentiation of the concentration terms in Eqns. (5.15) and (5.16) at the interface x_1 yields,

$$\left[\frac{\partial C_{TiB_2}}{\partial x}\right]_{x=x_1} = -\frac{\left(C_S - C_{1,2}\right)}{erf\xi}\frac{\partial}{\partial x}\left(erf\left(\frac{x_1}{2\sqrt{D_1 t}}\right)\right)$$

$$= -\frac{\left(C_S - C_{1,2}\right)}{\left(erf\xi\right)\sqrt{\pi D_1 t}}\exp\left(-\xi^2\right) \tag{5.19}$$

$$\left[\frac{\partial C_{TiB}}{\partial x}\right]_{x=x_1} = -\frac{\left(C_{2,1}-C_{2,3}\right)}{\left(erf\eta - erf\left(\phi_1\xi\right)\right)}\frac{\partial}{\partial x}\left(erf\left(\frac{x_1}{2\sqrt{D_2 t}}\right) - erf\left(\phi_1\xi\right)\right)$$

$$= -\frac{\left(C_{2,1}-C_{2,3}\right)}{\left(erf\eta - erf\left(\phi_1\xi\right)\right)\sqrt{\pi D_2 t}}\exp\left(-\phi_1{}^2\xi^2\right) \tag{5.20}$$

Similarly, differentiating the concentration term in Eqn. (5.16) at interface x_2,

$$\left[\frac{\partial C_{TiB}}{\partial x}\right]_{x=x_2} = -\frac{\left(C_{2,1}-C_{2,3}\right)}{\left(erf\eta - erf\left(\phi_1\xi\right)\right)}\frac{\partial}{\partial x}\left(erf\left(\frac{x_2}{2\sqrt{D_2 t}}\right) - erf\left(\phi_1\xi\right)\right)$$

$$= -\frac{\left(C_{2,1}-C_{2,3}\right)}{\left(erf\eta - erf\left(\phi_1\xi\right)\right)\sqrt{\pi D_2 t}}\exp\left(-\eta^2\right) \tag{5.21}$$

Now, plugging in Eqns. (5.19) and (5.20) in Eqn. (5.17), we get,

$$\left(C_{1,2}-C_{2,1}\right)\frac{\xi\sqrt{D_1}}{\sqrt{t}} = \frac{D_1\left(C_S - C_{1,2}\right)}{erf\xi\sqrt{\pi D_1 t}}\exp\left(-\xi^2\right) - \frac{D_2\left(C_{2,1}-C_{2,3}\right)}{\left(erf\eta - erf\left(\phi_1\xi\right)\right)\sqrt{\pi D_2 t}}\exp\left(-\phi_1{}^2\xi^2\right) \tag{5.22}$$

Rearranging Eqn. (5.22),

$$\left(C_{1,2}-C_{2,1}\right) = \frac{\left(C_S - C_{1,2}\right)}{\xi\sqrt{\pi}erf\xi}\exp\left(-\xi^2\right) - \frac{\left(C_{2,1}-C_{2,3}\right)}{\xi\phi_1\sqrt{\pi}\left(erf\eta - erf\left(\phi_1\xi\right)\right)}\exp\left(-\phi_1^2\xi^2\right) \tag{5.23}$$

Similarly, plugging in Eqn. (5.21) in Eqn. (5.18), we get,

$$\left(C_{2,3}-C_{3,2}\right)\frac{\eta\sqrt{D_2}}{\sqrt{t}}=\frac{D_2\left(C_{2,1}-C_{2,3}\right)}{\left(erf\eta-erf\left(\phi_1\xi\right)\right)\sqrt{\pi D_2 t}}\exp\left(-\eta^2\right) \tag{5.24}$$

Rearranging Eqn. (5.24),

$$\left(C_{2,3}-C_{3,2}\right)=\frac{\left(C_{2,1}-C_{2,3}\right)}{\eta\sqrt{\pi}\left(erf\eta-erf\left(\phi_1\xi\right)\right)}\exp\left(-\eta^2\right) \tag{5.25}$$

Eqns. (5.23) and (5.25) are nonlinear and are to be solved for two unknown parameters, ξ and η, which are the growth parameters for the TiB_2 and TiB layer, respectively. These equations were solved simultaneously using MATLAB program and ξ and η were determined for the three treatment temperatures (850, 950, and 1050 ˚C). From the growth parameters, the time-dependent layer thicknesses for the TiB_2 and TiB layers can be calculated using Eqns. (5.10) & (5.14), respectively.

The experimentally measured coating thicknesses at 850, 950, and 1050 ˚C, reported by Tikekar et al.,[104] are being used to validate the theoretical model. Table 5.1 summarizes the experimental data of boride layer thicknesses at different treatment temperatures. An important aspect needs to be considered in comparing the predicted growth rates of the TiB_2 and TiB layers with the experimental data. Because B diffusion occurs during the heating of the samples (10 °C/min) from room temperature to the isothermal treatment temperatures, there will be some pre-existing layer thickness that is not part of growth at the diffusion temperatures. Hence this was subtracted from the experimental data for a meaningful comparison with experiments.

Table 5.1 Average thickness values of TiB_2, TiB and the composite (TiB_2 + TiB) coating layers, determined for different B diffusion temperatures and times [104].

Time (h)	850°C			950°C			1050°C		
	TiB* (μm)	TiB_2 (μm)	Total (μm)	TiB (μm)	TiB_2 (μm)	Total (μm)	TiB (μm)	TiB_2 (μm)	Total (μm)
0.083	13	0.5 ± 0.1	13.5 ± 3.0	15	1 ± 0.1	16 ± 2.5	15	1.5± 0.1	16.5 ± 1.9
3	21.5	1.5 ± 0.1	23 ± 3.2	22.8	3.2 ± 0.3	26 ± 2.7	26	5 ± 0.3	31 ± 2.5
6	21.3	2.7 ± 0.2	24 ± 3.5	24.2	4.8 ± 0.2	29 ± 3.2	27	10 ± 0.7	37 ± 3.4
12	21.8	3.2 ± 0.2	25 ± 4.2	28.6	5.4 ± 0.3	34 ± 3.3	29	12 ± 0.9	41 ± 3.6
18	22.7	3.3 ± 0.3	26 ± 5.4	39.3	5.7 ± 0.3	45 ± 4.4	35	15 ± 0.9	50 ± 5.7
24	24.1	3.9 ± 0.3	28 ± 6.3	40.6	6.4 ± 0.4	47 ± 5.4	37	17 ± 1.0	54 ± 5.9

* TiB coating thickness was determined by subtracting the average thickness of TiB_2 layer from the average total coating thickness. Hence there is no S.D. for these data.

5.1.2. Comparison with experimental data

For the present calculations, the B diffusion coefficients were determined from the work of Fan et al.[97] and are reported in Table 5.2. The TiB layer growth is predominantly controlled by the diffusion of B in [010] direction, and therefore, the estimated B diffusivity in TiB is specific to this direction. The diffusivities of Ti in TiB_2 and TiB are 10^3 to 10^4 times lower than that of B in these phases.[92, 97] Hence the effect of Ti diffusion on layer growth can be neglected.

Figure 5.2 shows the predicted TiB_2 thickness development as a function of time, compared against the experimental data. The experimental data have been corrected for the 5 minutes growths ─ the TiB_2 thicknesses observed after 5 minutes at the respective temperatures were deducted from the original thicknesses. A reasonable agreement between the predicted data and the experimental data at 850 and 1050 ˚C can be seen. In

Table 5.2 Diffusivity data [97] used in the calculations of kinetics using error function solutions.

T (°C)	Chemical diffusivity of B in TiB_2 (m^2/sec)	Chemical diffusivity of B in TiB (m^2/sec)
850	1.34×10^{-16}	6.13×10^{-15}
950	6.92×10^{-16}	3.25×10^{-14}
1050	2.78×10^{-15}	1.34×10^{-13}

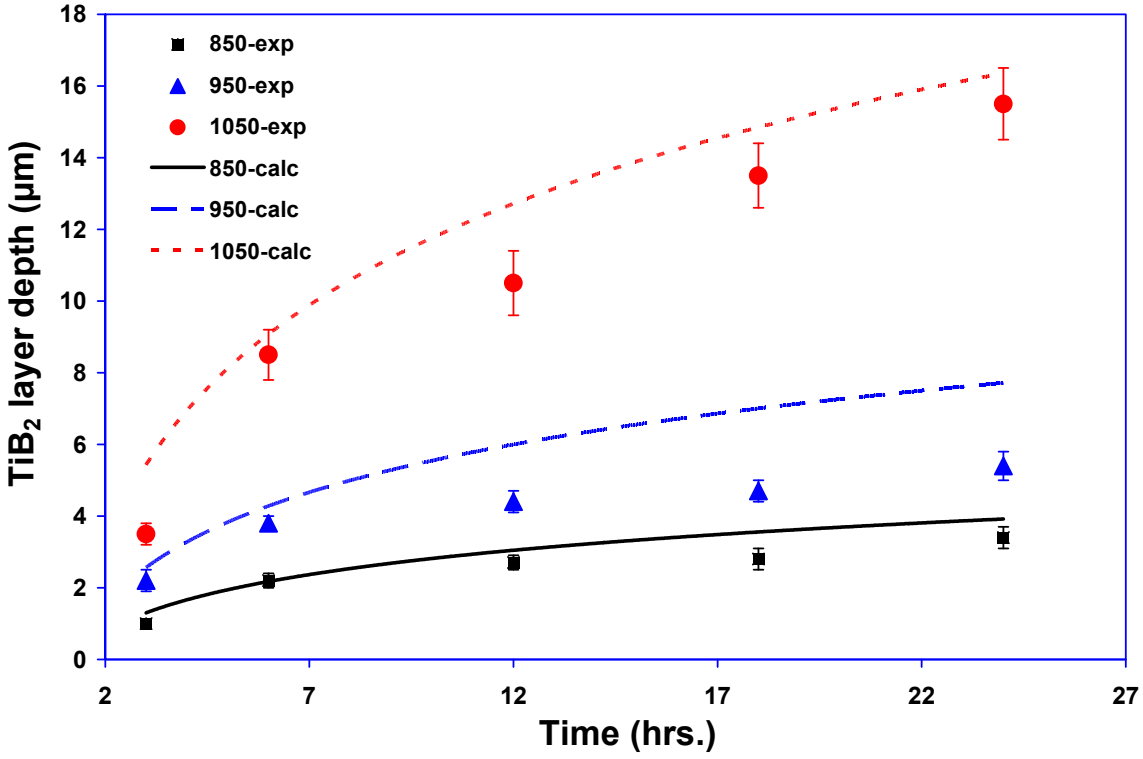

Figure 5.2 Comparison of the predicted and the experimentally measured TiB_2 thicknesses, after correcting for the TiB_2 layer growth due to 5 minutes exposure.

most cases, the predicted layer thicknesses of TiB_2 are within 10-20% of the experimental data. But the numerical predictions at 950 ˚C are slightly higher than the experimental trend. Especially for treatment times exceeding 6 hours, the numerical predictions are 20-30% higher than the experimental values. As discussed in the next section of this chapter, the TiB_2 layer recedes due to a complex mechanism involving enhanced anomalous diffusion in Ti near the α/β phase transition temperature.[21] The temperature region for such anomalous diffusion in Ti can extend up to 950˚C. It is therefore suggested that the small difference (20-30%) between the predicted and the experimental TiB_2 layer thickness at 950˚C, especially at longer boriding times, is due to the TiB_2 layer recession. This effect is absent at 850˚C and 1050˚C.

Figure 5.3 is the comparison of the experimentally measured TiB coating thicknesses (after deducting the TiB thicknesses due to 5 minutes exposure) and the predicted growth data. The predictions are in reasonable agreement with the experimental data at 850 and 950 °C. Most of the numerical data are in the range of 20-25% of that of the experimental values. However, there is a large discrepancy between the predicted and the experimental data at 1050 °C by about a factor of two. Actually, the experimental growth data at 1050 °C, being nearly similar to that at 950 °C, is itself quite unusual.[104] This may be attributed to the thickening of TiB whiskers at high temperatures. While almost all of the TiB whiskers were relatively thin at 850 and 950 °C; at 1050 °C, many TiB whiskers in the layer were relatively thicker (Figure 5.4 a and b). It was suggested earlier [92] that diffusion in the transverse direction of TiB whiskers is about 10 times slower than that in the [010] direction, which is the axial direction of whiskers. This means that the rates of thickening and lengthening will be about equal when the whisker

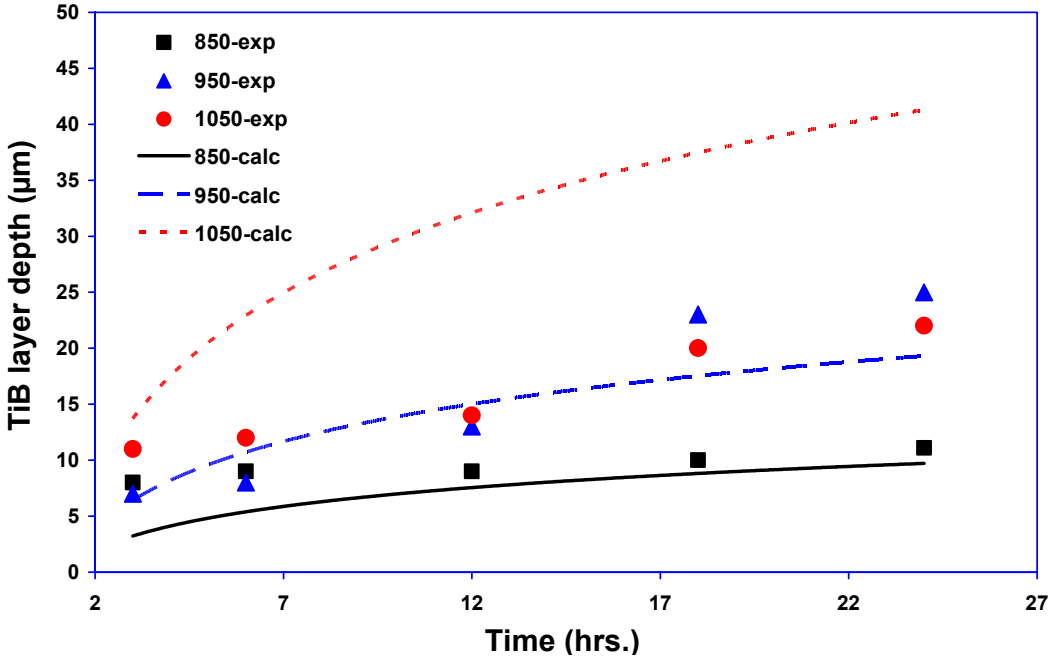

Figure 5.3 Comparison of the predicted and the experimentally measured TiB thicknesses, after correcting for the TiB layer growth due to 5 minutes exposure.

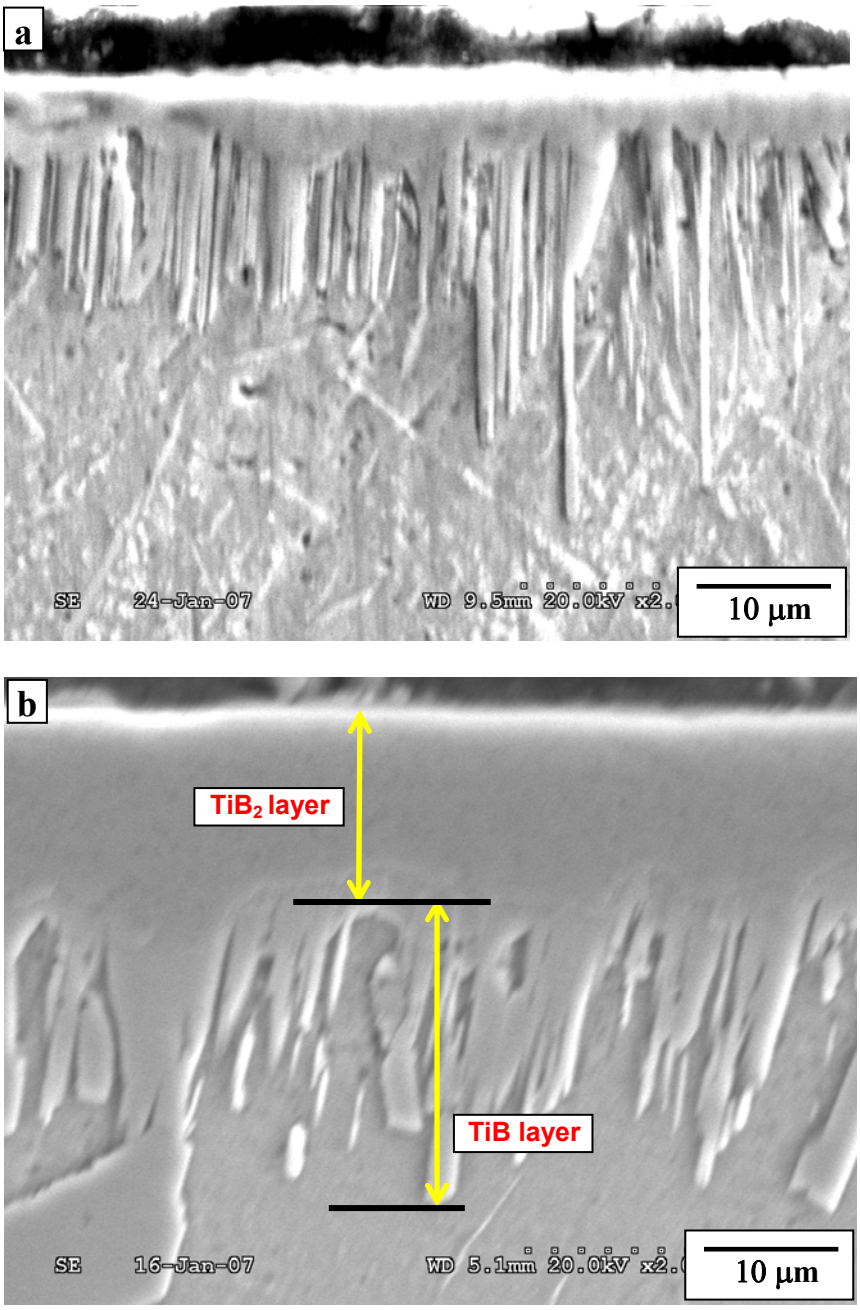

Figure 5.4 SEM micrographs of boride coating on grade 2 CP-Ti after isothermal treatments for 24 hours at **(a)** 850 °C and **(b)** 1050 °C.

aspect ratio reaches 10. Above this aspect ratio, thickening of TiB whiskers provides a faster means of transporting B and reacting with Ti, as opposed to the axial transport and extension of growth along the TiB axial direction. Since the model predictions are based only on diffusivities for growth along the [010] TiB direction, they should not agree with the experimental data of total layer thickness at 1050 °C, if TiB whiskers appear to be much thicker than those at lower temperatures. Indeed, it appeared from the experimental results, that at 1050 ˚C a significant fraction of TiB is no longer whiskers and they seemed to thicken due to increased B diffusion in the direction transverse to TiB whisker axis.

Figure 5.5 shows the comparison of the total (TiB_2+TiB) layer thickness predictions with the experimental data. The predictions for the 850 and 950 °C are in reasonable agreement with the experimental data, while at 1050 °C; the predicted thicknesses are relatively higher. This difference arises from the TiB layer growth behavior as discussed above.

The diffusion model, described above, seemed to predict the boride layer growth kinetics well–specifically at temperatures away from the phase transition temperature in Ti. The predicted TiB_2 layer thicknesses are within 25% of that the experimental values for all three boriding temperatures. The predictions of the TiB layer also show reasonable agreements with that of the experimental data except for the 1050 °C boriding condition. The plausible reason behind the discrepancy has also been described in view of the TiB layer morphology observed at 1050 °C.

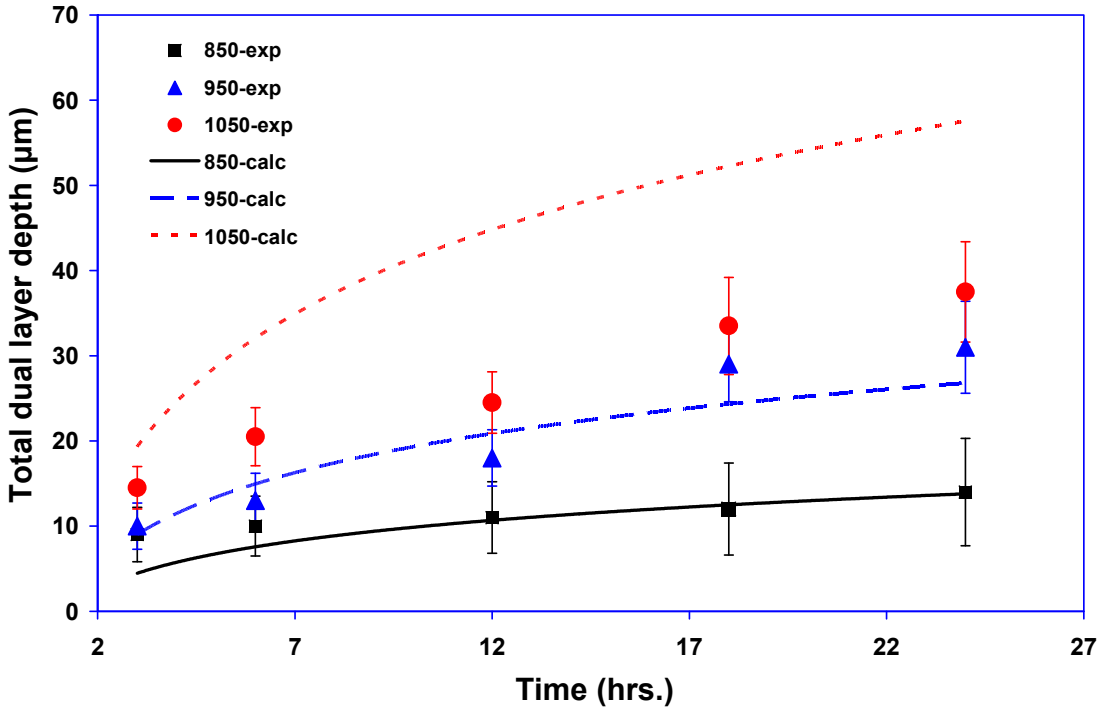

Figure 5.5 Comparison of the predicted and the experimentally measured dual (TiB_2+TiB) coating layer thicknesses, after correcting for the TiB_2 and the TiB layer growth due to 5 minutes exposure.

5.2 Structure and kinetics of growth of boride layers near the phase transition temperature in Ti

5.2.1 Premise

This section focuses on the detailed results obtained during the isothermal boriding experiments conducted near the phase transition temperature of Ti. The obtained boride layer thicknesses, analysis of morphological aspects and the hardness measurements on these layers were documented and reported. Furthermore, a theoretical model is proposed based on Fick's second law of diffusion to explain the boride layer growth kinetics near the transition temperature.

5.2.2 Structure and properties of boride coatings

The average coating thickness values along with the standard deviations obtained during isothermal boriding close to the transition temperature are presented in Table 5.3. Figure 5.6 shows the plot of the average coating thickness as a function of time at different treatment temperatures. The coating thicknesses increase with increase in treatment time. The coating thicknesses obtained at 900 and 1050 ˚C in our previous studies [104] are also plotted in the same figure for comparison. The growth behavior of boride layers at all temperatures can be represented by the parabolic kinetics. In Figure 5.6, the treatment temperatures: 900, 910, and 915 °C are the closest to the β transus temperature (913 °C) of the material used in this study. Of these, the temperature 910 °C, within the experimental error of ±3 °C, is the closest to the β transus and it can be seen that the coating growth kinetics at this temperature is the most accelerated, compared to that at 900 and 915 °C. Thus, 910 °C, for all practical purposes can be considered to be right on the α-β transition point.

Table 5.3 Summary of total (TiB_2+TiB) coating thicknesses obtained in varied isothermal treatments

Time (hr)	890˚C		900˚C		910˚C		915˚C	
	Total (µm)	SD (µm)	Total (µm)	SD (µm)	Total (µm)	SD (µm)	Total (µm)	SD (µm)
3	18	6	39	4	30	5	23	6
6	28	7	40	4	44	8	35	8
12	31	8	45	5	54	9	52	8
18	44	8	54	6	65	10	58	9
24	46	10	60	6	75	11	66	10

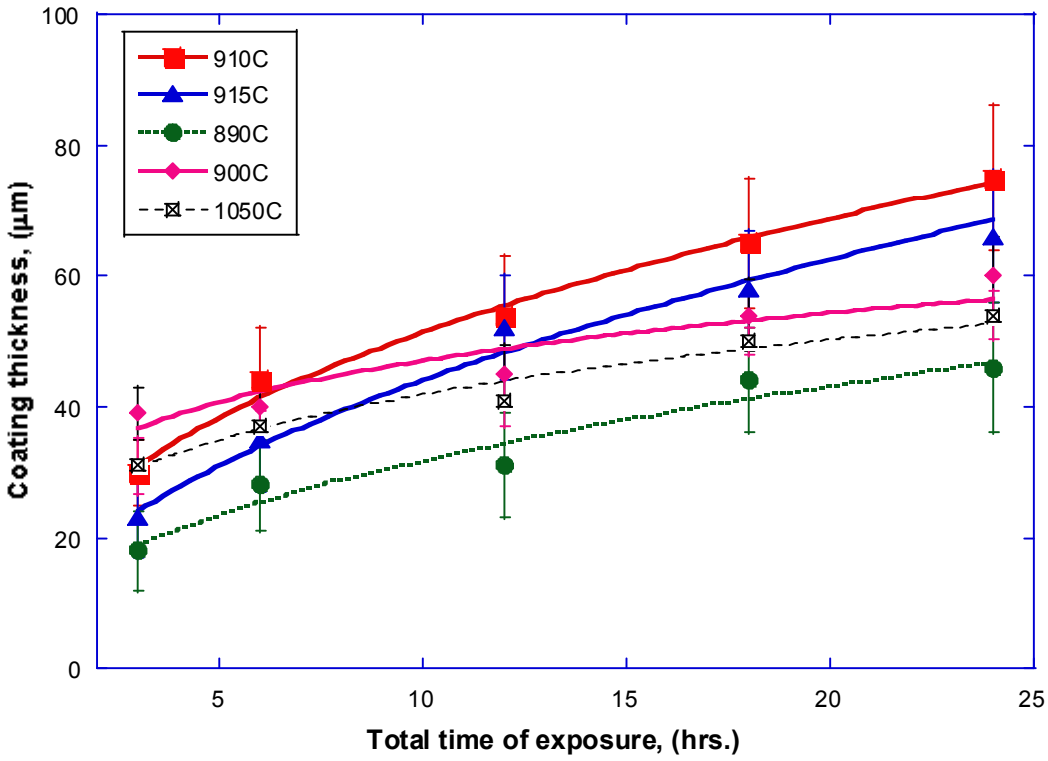

Figure 5.6 Total (TiB_2+TiB) coating thicknesses obtained in isothermal diffusion treatments plotted as a function of total isothermal exposure time.

To illustrate the general structure of conventional boride layers on titanium, the SEM micrographs of the boride coating structure obtained at 850 and 1050 ˚C isothermal treatments are to be referred from Figure 5.4 (a) and (b), respectively.[104] These coatings actually consist of two boride layers, a top TiB_2 layer and a TiB layer below. The TiB_2 is a monolithic layer whereas the TiB layer is made of long, high aspect ratio whiskers that grow nearly perpendicular to the surface. Generally, the relative kinetics of growth of these layers determine the total coating thickness, since the B-TiB_2, TiB_2-TiB and TiB-Ti interfaces are nearly in equilibrium during the diffusion layer growth.[88] It was found that at temperatures in α-phase field (850 ˚C), the TiB layer growth is relatively faster than that of TiB_2 layer. On the other hand, at treatment temperatures > 950 ºC which is well

inside the β-phase field, a relatively thicker TiB_2 layer is formed. This is evident from coating structure of 1050 ˚C sample, where a relatively thicker TiB_2 layer is obtained compared to that obtained at 850 ˚C. The total coating depth is, however, controlled by the diffusion of B through the axis of TiB whiskers.[92] The reverse rate of diffusion of Ti in TiB toward the surface is about ten times slower than the forward diffusion of B.[97] Therefore, the major limiting factor is the diffusion of B through TiB and its reaction with Ti substrate to grow the TiB whisker. Consistent with this, the coating thicknesses at the isothermal diffusion temperatures of 850 and 1050 ˚C for 24 hours saturates to about 30 and 55 μm, respectively.

The structure of boride layer in samples borided at 890, 910, and 915˚C for 3 hours are presented in Figure 5.7 (a-c). The coating at this stage is characterized by a very thin TiB_2 outer layer (1 to 1.5 μm) and a TiB layer containing distributed TiB whiskers growing into the depth. The thickness of the TiB_2 layer does not seem to vary with the temperature. However, the TiB layer beneath the TiB_2 layer grew slightly deeper into the substrate at temperatures 910˚C compared to that at 890 and 915˚C, although the layer itself does not contain a high area density of TiB whiskers. This is probably due to the early stage of B diffusion where the inherent tendency of the formation and growth of TiB into substrate is distributed in nature.[103]

The SEM micrographs of coating structure in samples borided at 890, 910, and 915 ˚C for 12 hours are presented in Figure 5.8 (a-c). The only common aspect between the coating structures in these conditions and that obtained at 850 and 1050 ˚C is that both TiB_2 and TiB layers are present. The thicknesses of the TiB_2 layers in these samples

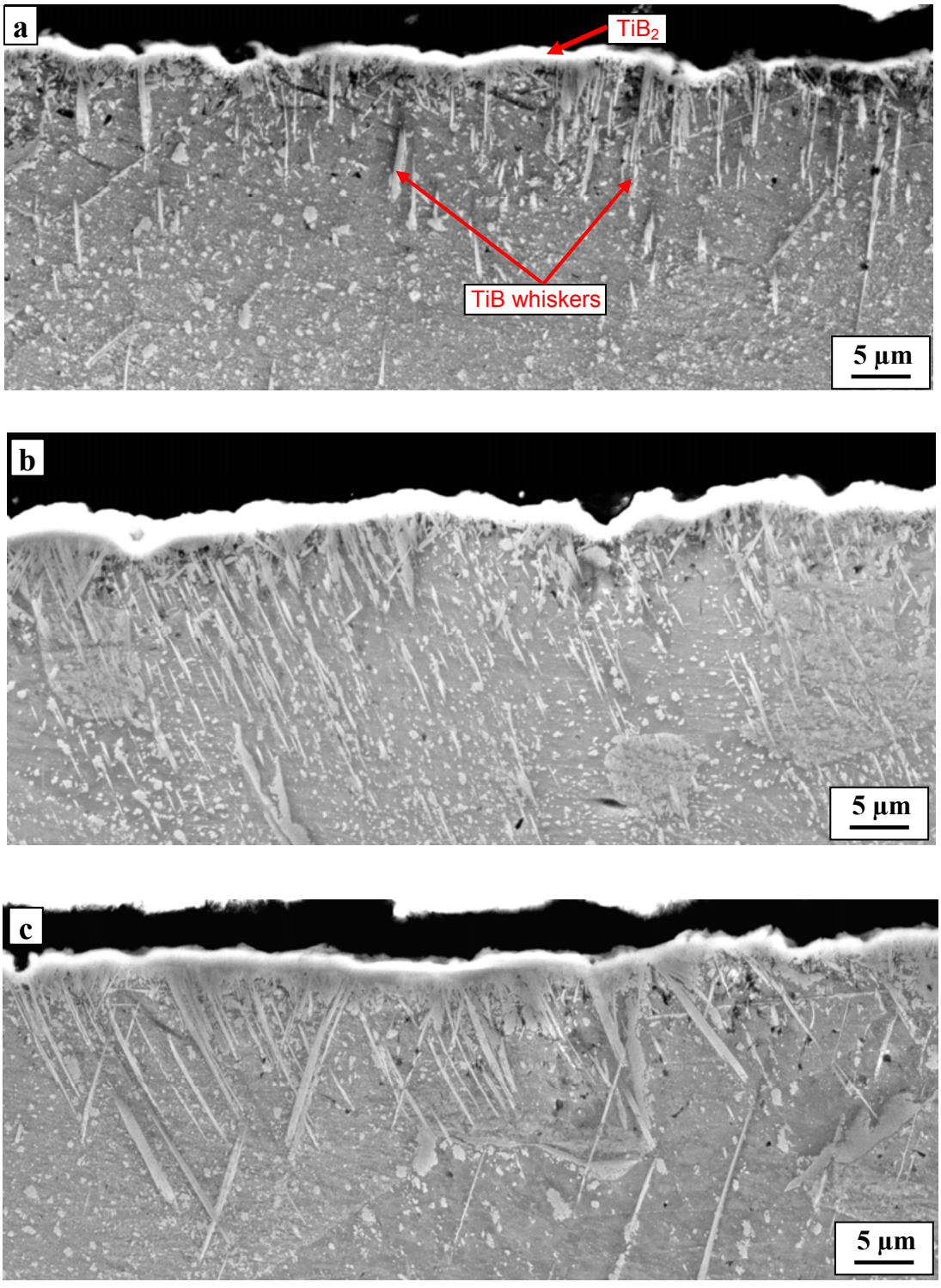

Figure 5.7 SEM micrographs of boride coating on grade 2 CP-Ti after isothermal treatments for 3 hours at **(a)** 890 °C, **(b)** 910 °C and **(c)** 915 °C.

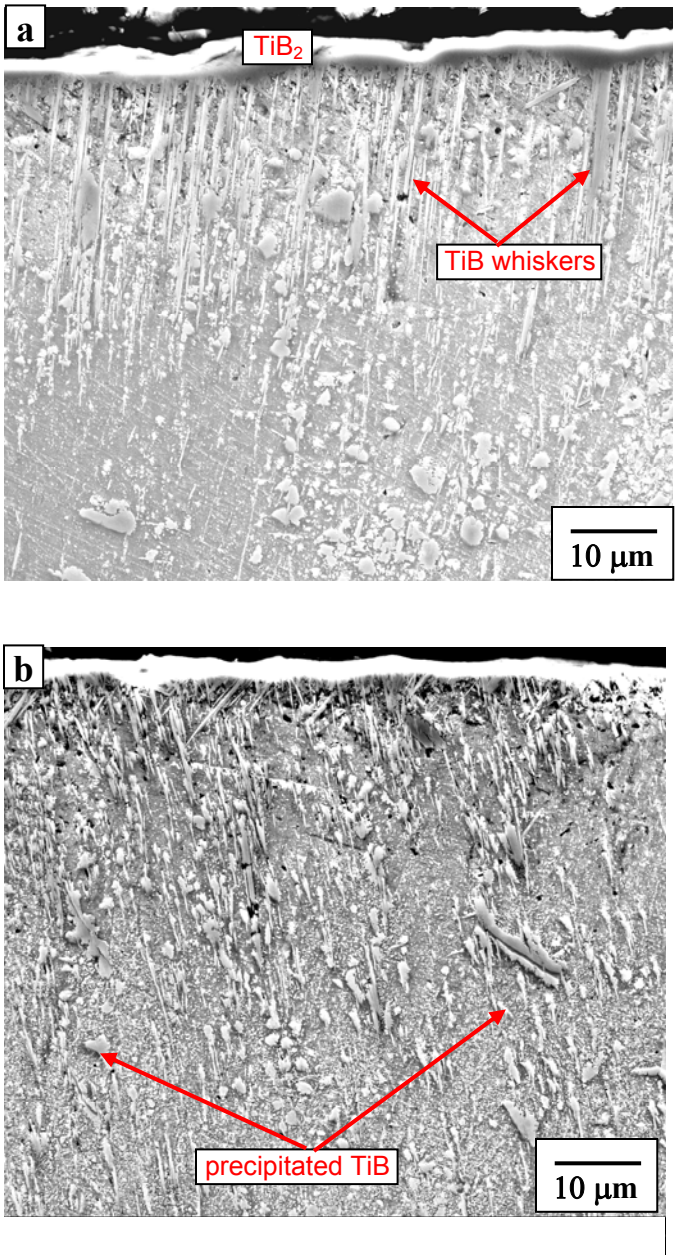

Figure 5.8 SEM micrographs of boride coating on grade 2 CP-Ti after isothermal treatments for 12 hours at **(a)** 890 °C, **(b)** 910 °C and **(c)** 915 ºC.

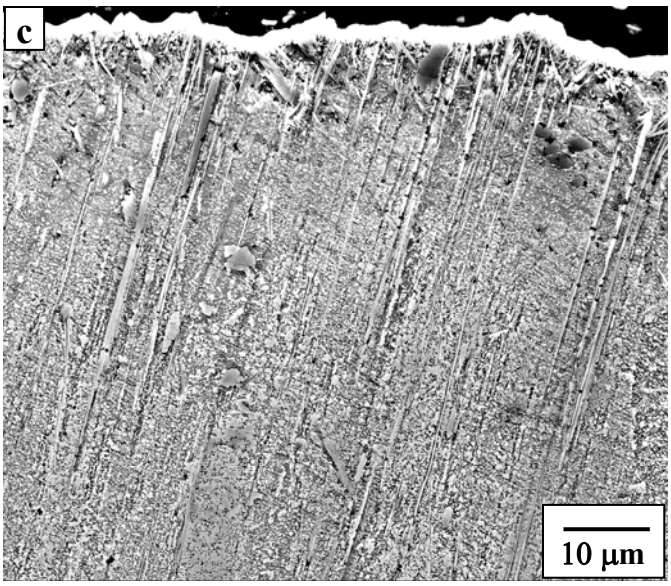

Figure 5.8 continued

are in the range between 3 to 4 μm. As observed in 3 hours treated sample, the thickness of the TiB_2 layers in these samples also do no seem to be affected by the temperature, whereas the TiB layer beneath the TiB_2 layer grew relatively deeper into the substrate at temperatures 910 and 915 ˚C compared to that at 890 ˚C (Table 5.3). The TiB layers are made of TiB whiskers and precipitated TiB particles as shown in Figure 5.8 (a and b).

The SEM micrographs of coating structure in samples borided at 890, 910, and 915 ˚C for 24 hours are shown in Figure 5.9 (a-c). A very thin layer of TiB_2 also formed in these samples, irrespective of the treatment temperature. The TiB_2 layers in these samples are relatively thicker than those in 12 hours treated samples but still much thinner than that in the sample treated at 1050 ˚C for 24 hours. This is expected, because a relatively thicker TiB_2 layer is favored at this treatment temperature as it lies

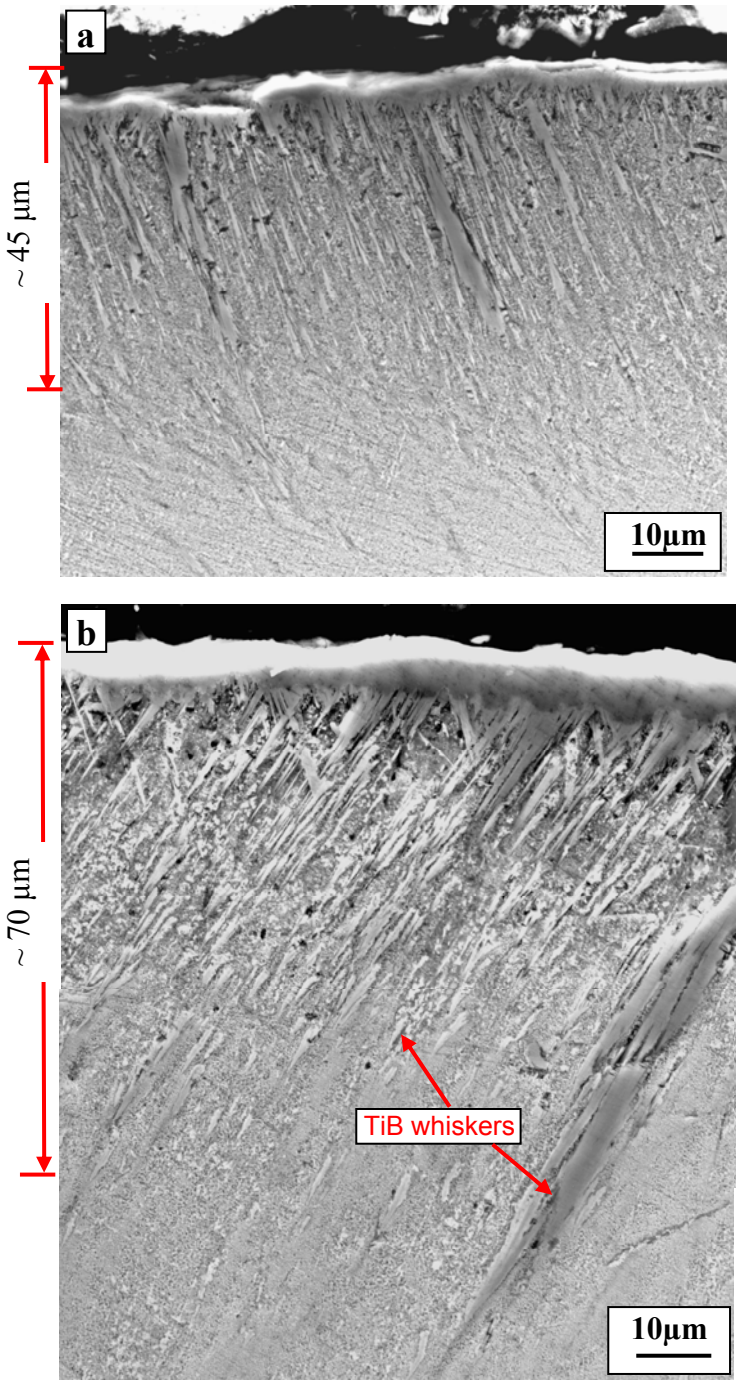

Figure 5.9 SEM micrographs of boride coating on grade 2 CP-Ti after isothermal treatments for 24 hours at **(a)** 890 °C, **(b**) 910 °C and **(c)** 915 ˚C.

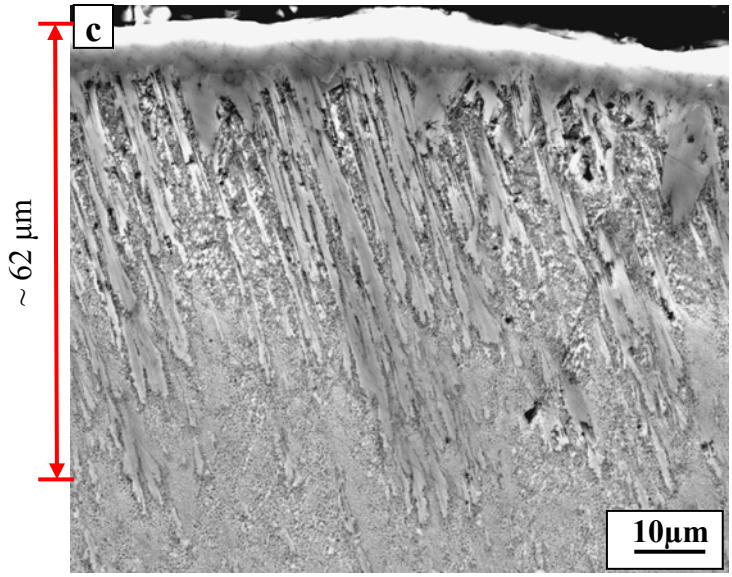

Figure 5.9 continued

completely in the β phase field of Ti. TiB layers in the present samples are characterized by ahigh area density of TiB whiskers penetrating deep into the substrate. In particular, at treatment temperatures of 910 and 915 ˚C, the area densities of TiB whiskers are relatively higher and the penetration was much deeper, compared to that treated at 890 ˚C. For the sample borided at 890 ˚C for 24 hours (Figure 5.9 (a)), a lower average coating thickness (~ 46µm) was obtained compared to that at 910 and 915 ˚C. This treatment temperature is significantly below the transition temperature (transition temperature for titanium ~ 913˚C) and probably only α phase field existed in this condition.

To illustrate the influence of proximity to the phase transition temperature the TiB_2 and the total layer thicknesses were plotted as a function of temperature in Figure

5.10 (a and b). The thickness of TiB_2 layer after 24 hours varied significantly with the temperature while such a variation is not seen at shorter times (3 hours). As shown in Figure 5.10(a), the TiB_2 layer thickness, grown in 24 hours of diffusion, goes through a minimum near the phase transition temperature. Assuming that "normal" growth conditions exist at 850°C and 1050°C, a straight line was drawn joining these two data points to show how far the TiB_2 growth at temperatures near the phase transition is lagging behind the normal trend. Figure 5.10(b) shows the variation of total boride layer thickness as a function of temperature for various treatment times. It can be seen that near the phase transition temperature, much deeper boride layers are obtained. Again assuming the prevalence of overall normal growth kinetics at 850°C and 1050°C, a straight line was drawn to show how far the growth kinetics is accelerated near the phase transition temperature. It can be seen that the increased TiB growth is more than that required to offset the lag in TiB_2 growth near the transition temperature. It is also to be noted that the α-β phase transition temperature is sensitive to alloying elements, especially oxygen. Even the presence of a small amount of oxygen introduces a α+β phase field in Ti.[27] For example, for 0.15 wt% of oxygen, α to β transition takes place over a temperature range of 883 to 914˚C. Hence, the enhanced TiB layer growth can also be seen at 890˚C (Figure 5.10(b)), as the α to β phase transformation must have started at this temperature.

The surprising finding of this study is that the TiB whiskers grow deeper at temperatures close to the α-β transition temperature and this growth is significantly higher than that obtainable at a much higher temperature (1050 ˚C). This is evident from

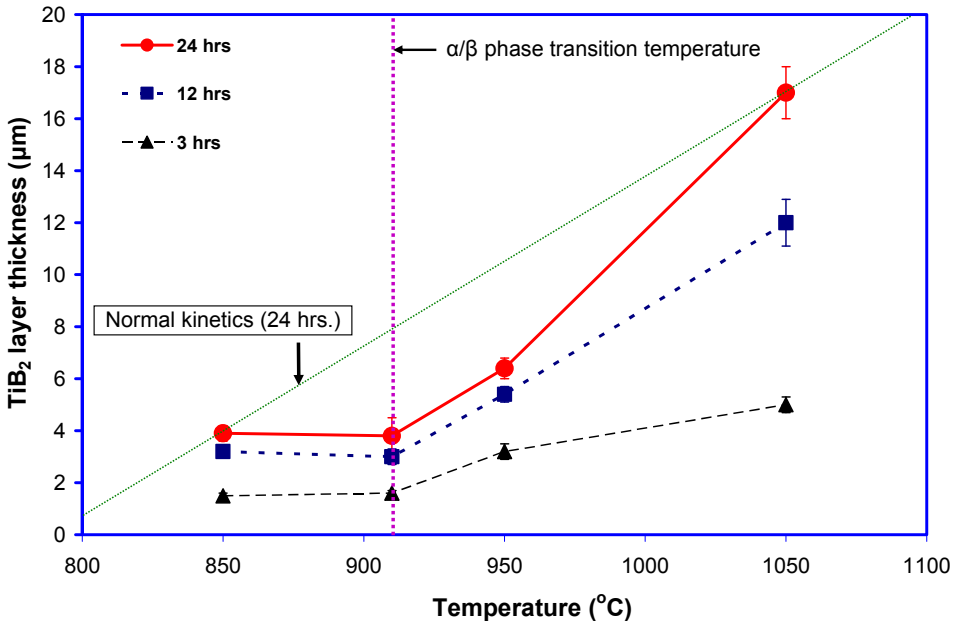

(a)

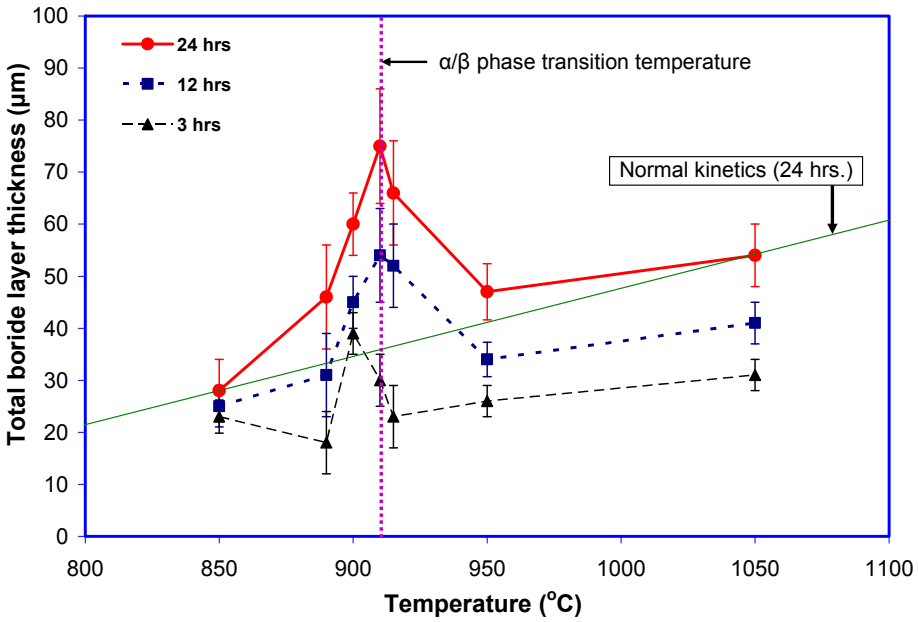

(b)

Figure 5.10 The enhanced growth of boride layers near the phase transition temperature, **(a)** TiB_2 layer thickness and **(b)** the total (TiB_2+TiB) boride layer thickness at different temperatures. A dotted line approximately indicating the expected normal kinetics for 24 hours (without the anomalous contribution), across the region near the phase transition, is drawn to highlight the deviations.

Figure 5.6 and 5.9 (b and c), where the average depth of the coating layers exceeded 60 μm. The sample treated at 1050 ˚C for 24 hours has a maximum coating depth of about 50 μm. Figure 5.11 (a and b) shows the montage of coating morphologies for the samples borided at 900 and 910 ˚C for 24 hours. Most of the TiB whiskers are in nanometer size range varying between 200 to 450 nm although isolated whiskers of 2 to 3 μm size range are also present in some places. The TiB layer is actually made of two forms of TiB– long whiskers and particle-like and/or irregular shaped TiB. The particle-like TiB are referred to as "precipitated TiB" because these particles appear to have formed during cooling of the sample from the boriding temperature. The B atoms diffusing in the Ti matrix at the time of boriding treatment may have precipitated as TiB particles during the cooling of the sample because of the limited solubility of B in Ti. These particles are clearly seen in the magnified SEM image of the 900˚C/24hrs treated sample in Figure 5.12. This structure seems to support the idea that B diffusion near the phase transition temperature is enhanced.

Knoop hardness measurements were made on the sample treated at 910 ˚C for 24 hours and the hardness profile is shown in Figure 5.13. The data confirm the observations with respect to the SEM coating structure– the surface layers are hardened to a depth of about 40 μm. The hardening depth is smaller than the depth of the actual coating because the coating depth is taken as the farthest tip of the growing TiB whiskers. The high hardness (> 3000 kg/mm^2) region near the surface corresponds to the thin layer of TiB_2 (the hardness of monolithic TiB_2 is about ~4000 kg/mm^2).[153] The subsurface layer to a depth of about 5 μm is actually a mixture of TiB whickers and TiB_2 monolith, or the transition region which explains the steep decrease in hardness with distance into

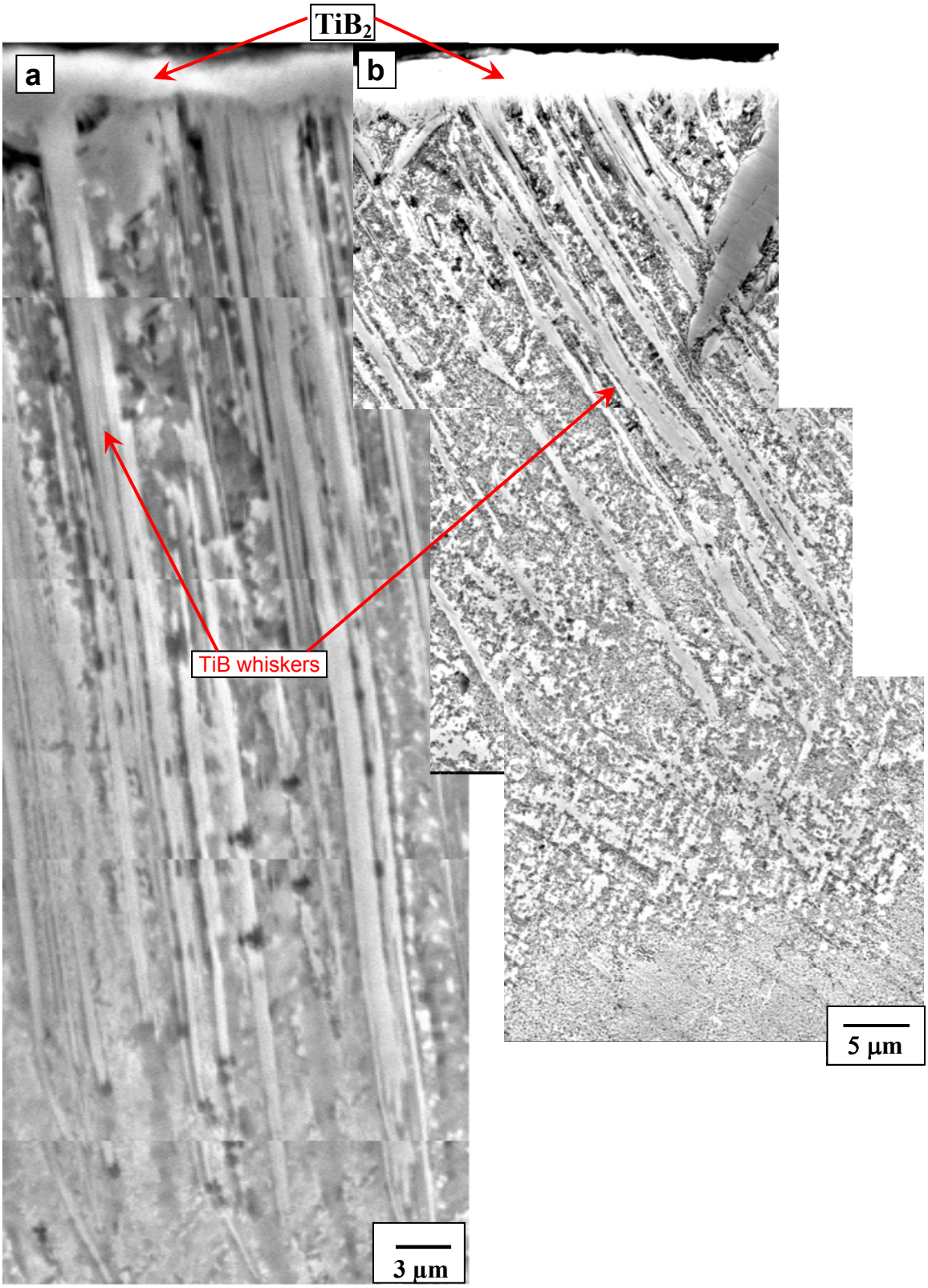

Figure 5.11 Higher magnification SEM micrographs of boride coating on grade 2 CP-Ti after isothermal treatments for 24 hours at **(a)** 900 ˚C [104], **(b)** 910 ˚C.

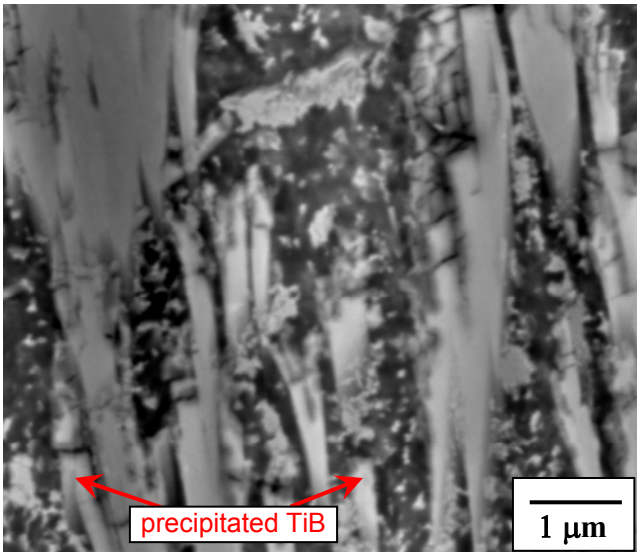

Figure 5.12 Higher magnification SEM micrograph showing the TiB precipitates in 900 °C/24 hours boriding condition.

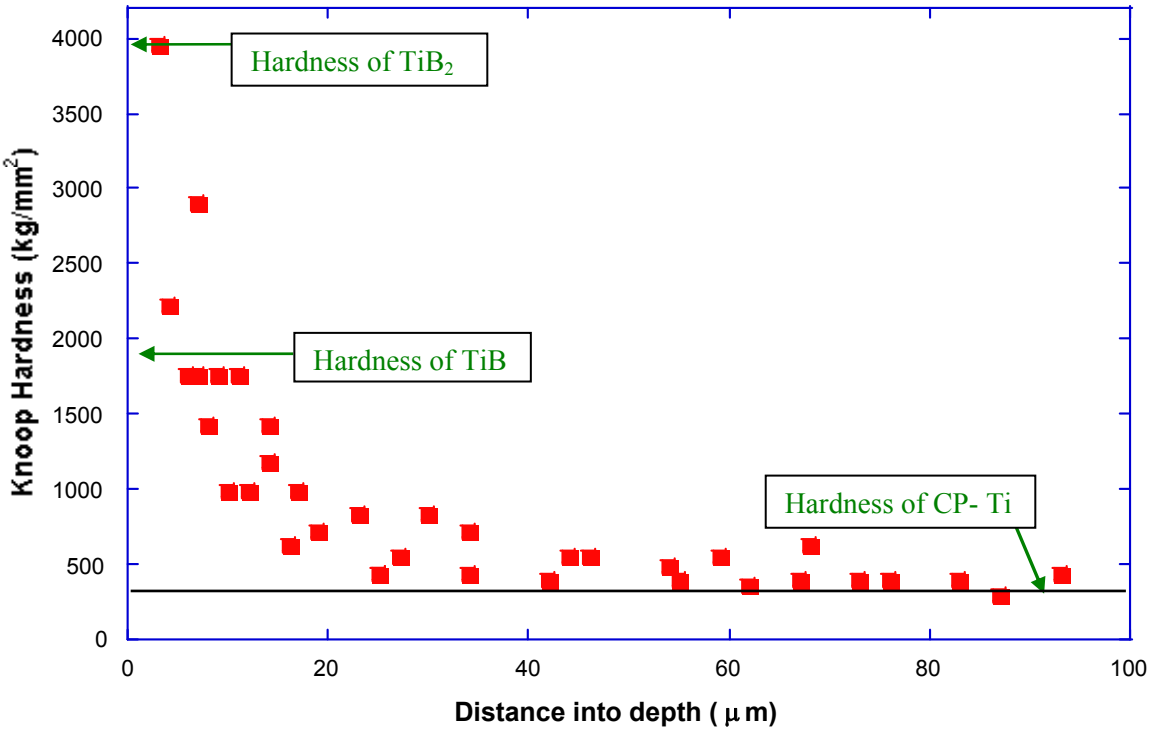

Figure 5.13 Knoop hardness profile for the total (TiB_2+TiB) coating produced under isothermal treatment at 910 ˚C for 24 hours.

the substrate. The hardness of monolithic TiB is about 1900 kg/mm^2.[154] The coating structure beyond about 5 μm is a mixture of TiB and Ti, with the volume fraction of TiB gradually decreasing with distance into the depth of the sample. The hardness profile beyond 5 μm is consistent with the coating structure.

It is evident from the present results that near the α-β phase transition temperature of CP-Ti, the overall boride coating thicknesses obtained were significantly higher than at temperatures farther from it. The coating thickness obtained at very close to the transition temperature (910 ˚C) was the highest among all the treatment conditions. Since the TiB layer growth is limited by the diffusion of B in TiB phase, the results suggest the existence of additional diffusion paths for B in Ti matrix in order to account for the enhanced TiB layer growth near the transition temperature. The influence of anomalous diffusion in Ti and its impact on B diffusion in Ti near the transition temperature can be helpful in explaining such enhancement in TiB layer growth. It is to be noted that in the anomalous diffusion domain, enhanced diffusivities of Sn [148] and Al [149] in Ti has also been reported in the literature. Hence, it is quite possible that the B diffusivities in β-Ti near the phase transition temperature are increased to bring about relatively higher degree of boride coating growth. In the following section, an attempt has been made to develop a numerical model to calculate the TiB coating thickness close to the transition temperature incorporating B diffusivity through TiB_2, TiB as well as through the Ti matrix.

5.2.3 Modeling of coating growth kinetics

Theoretical modeling of TiB_2 and TiB growth under normal diffusion conditions on the basis of Fick's second law of diffusion was discussed in the previous section. However, the same model would not provide an agreeable layer thickness near the phase

transition temperature (910 ˚C) as the growth of the boride phases are limited by the diffusivities of B through these phases. Hence, there seems to exist some additional diffusion path for B near the phase transition. It is assumed here that the Ti-matrix regions present in between TiB whiskers are the additional path for B diffusion. The Ti-matrix seems to be in direct contact with the TiB_2 layer–the TiB_2 can act as a B source for diffusion inside the matrix and thereby forming additional TiB whiskers. Here, a modification of the previous diffusion model is presented which simultaneously considers the B diffusion in TiB and Ti-matrix regions to explain the relatively deeper TiB coating growth.

The development of the model is illustrated on the basis of growth of TiB_2/TiB whisker layer on titanium as shown in Figure 5.14 (a and b). There are three interfaces present in this system: the B-TiB_2 interface (x_0), TiB_2-TiB interface (x_1), and the TiB-Ti interface (x_2). The diffusion model, described in the previous section, can be modified for the case of diffusion of B near the transition temperature with the incorporation of a B flux term though the Ti-matrix present in between the TiB whiskers. A certain area fraction of Ti-matrix $\left(A_{Ti}^{f}\right)$ exists in between the growing TiB whiskers.[1] This is shown schematically in Figure 5.15, where a unit cross-sectional area of the TiB_2 interface (x_1) is in contact with certain area fraction $\left(A_{Ti}^{f}\right)$ of the Ti-matrix and the remaining fraction $\left(A_{TiB}^{f}\right)$ with the TiB such that $A_{Ti}^{f} + A_{TiB}^{f} = 1$. The B atoms from the TiB_2 layer are expected to diffuse through both TiB whiskers as well as the matrix, thereby forming additional growth of TiB. The extent to which B atom can diffuse through the matrix depends on the

[1] It is noted that the TiB layer is not a solid monolith, but is made of the growing TiB whiskers and Ti matrix between TiB whiskers. In SEM micrographs, this Ti matrix appears to be in contact with the continuous TiB_2 layer at the surface. So, this assumption is reasonable.

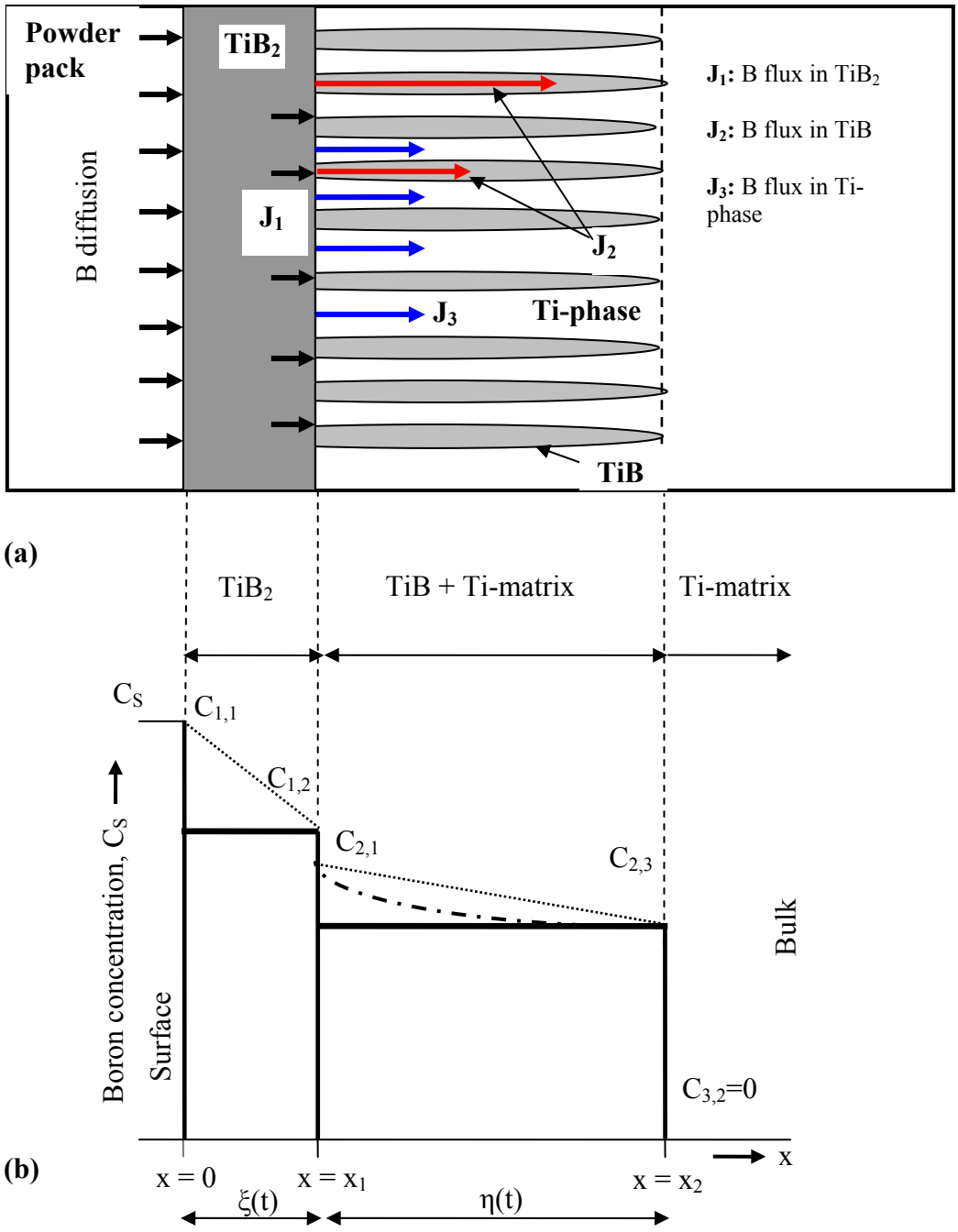

Figure 5.14 Illustration of diffusional growth of TiB whiskers near the phase transition temperature (910 ˚C) in CP-Ti **(a)**. The B concentration profile in growing boride phases into the depth of the substrate **(b)**.

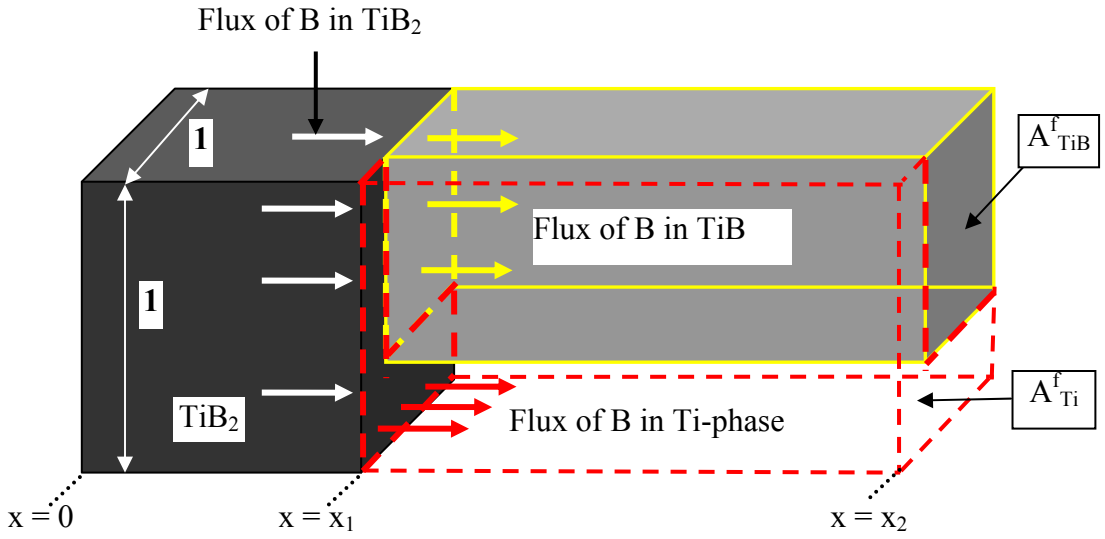

Figure 5.15 Schematic of the structure of TiB_2 interface of unit area that is in contact with a certain fractional area (A^f_{TiB}) of TiB phase and the remaining fractional area (A^f_{Ti}) of Ti phase.

fractional area of the matrix that is in contact with the TiB_2 layer at the interface x_1. The area fraction of the matrix that is in contact with the TiB_2 layer is significant as observed in the SEM micrographs. The relatively higher diffusivities of B though the matrix compared to that through the TiB near the transition temperature can enhance the growth kinetics of the TiB layer.

Hence, for this case, Eqns. (5.17) and (5.18), pertaining to mass conservation at TiB_2-TiB and TiB-Ti interfaces, can be modified as,

$$\left(C_{1,2}-C_{2,1}\right)\left(\frac{dx_1}{dt}\right)=-D_1\left(\frac{\partial C_{TiB_2}}{\partial x}\right)_{x=x_1}+D_2\left(A^f_{TiB}\right)\left(\frac{\partial C_{TiB}}{\partial x}\right)_{x=x_1}+D_3\left(A^f_{Ti}\right)\left(\frac{\partial C_{Ti}}{\partial x}\right)_{x=x_1} \tag{5.26}$$

$$\left(C_{2,3}-C_{3,2}\right)\left(\frac{dx_2}{dt}\right)=-D_2\left(A^f_{TiB}\right)\left(\frac{\partial C_{TiB}}{\partial x}\right)_{x=x_2}-D_3\left(A^f_{Ti}\right)\left(\frac{\partial C_{Ti}}{\partial x}\right)_{x=x_2} \tag{5.27}$$

In Eqns. (5.26) and (5.27), the term containing D_3 is the term that accounts for the additional flux of B by anomalous diffusion through the Ti-matrix region between the TiB whiskers. This flux together with the flux of B through the TiB whiskers (terms containing D_2 in Eqns. (5.26) & (5.27)) is the total flux of B atoms leaving the TiB_2-TiB interface. Hence, this total flux is subtracted from the flux of B in TiB_2 in Eqn. (5.26). The total flux arriving at the TiB-Ti interface will cause the movement of this interface into the depth of the substrate satisfying Eqn. (5.27). Note that the differential of the concentration terms are negative. The variation of concentration of B in the Ti-matrix region is given by,

$$C_{Ti}(x,t) = C_{2,1}\left(1 - erf\left(\frac{x}{2\sqrt{D_3 t}}\right)\right) \tag{5.28}$$

where D_3 is the diffusion coefficient of B in the Ti-matrix.

For the TiB_2-Ti interface position (x_1), one can define a dimensionless growth parameter, $\xi^{//}$ such that,

$$x_1 = 2\xi^{//}\sqrt{D_3 t} \tag{5.29}$$

Eqn. (5.29) corresponds to the same interface movement described by Eqns. (5.10) and (5.11). Hence, they can be equated as,

$$x_1 = 2\xi\sqrt{D_1 t} = 2\xi^{/}\sqrt{D_2 t} = 2\xi^{//}\sqrt{D_3 t} \tag{5.30}$$

Rearranging Eqn. (5.30), one can get,

$$\xi^{//} = \xi\sqrt{\frac{D_1}{D_3}} = \xi\phi_2 \tag{5.31}$$

where $\phi_2 = \sqrt{\frac{D_1}{D_3}}$

Similarly, at TiB-Ti interface at x_2, one can write,

$$x_2 = 2\eta\sqrt{D_2 t} = 2\eta^{/}\sqrt{D_3 t} \tag{5.32}$$

Rearranging Eqn. (5.32), one can get,

$$\eta^{/} = \eta\sqrt{\frac{D_2}{D_3}} = \eta\phi_3 \tag{5.33}$$

where $\phi_3 = \sqrt{\frac{D_2}{D_3}}$

Differentiation of the concentration term in Eqn. (5.28) at the interface x_1 yields,

$$\left[\frac{\partial C_{Ti}}{\partial x}\right]_{x=x_1} = -C_{2,1}\frac{\partial}{\partial x} erf\left(\frac{x_1}{2\sqrt{D_3 t}}\right)$$

$$= -\frac{C_{2,1}}{\sqrt{\pi D_3 t}}\exp\left(-\phi_2^2\xi^2\right) \tag{5.34}$$

Similarly, differentiating the concentration term in Eqn. (5.28) at interface x_2,

$$\left[\frac{\partial C_{Ti}}{\partial x}\right]_{x=x_2} = -C_{2,1}\frac{\partial}{\partial x}erf\left(\frac{x_2}{2\sqrt{D_3 t}}\right)$$

$$= -\frac{C_{2,1}}{\sqrt{\pi D_3 t}}\exp\left(-\phi_3^2\eta^2\right) \tag{5.35}$$

Now, plugging in Eqns. (5.19), (5.20) and (5.34) in Eqn. (5.26), we get,

$$\left(C_{1,2}-C_{2,1}\right)\frac{\xi\sqrt{D_1}}{\sqrt{t}} = \frac{D_1\left(C_S-C_{1,2}\right)}{erf\xi\sqrt{\pi D_1 t}}\exp\left(-\xi^2\right) - \frac{D_2 A_{TiB}^f\left(C_{2,1}-C_{2,3}\right)}{\left(erf\eta - erf\left(\phi_1\xi\right)\right)\sqrt{\pi D_2 t}}\exp\left(-\phi_1^2\xi^2\right) -$$
$$\frac{D_3 A_{Ti}^f C_{2,1}}{\sqrt{\pi D_3 t}}\exp\left(-\phi_2^2\xi^2\right)$$

Rearranging the above Eqn.,

$$\left(C_{1,2}-C_{2,1}\right) = \frac{\left(C_S-C_{1,2}\right)}{\xi\sqrt{\pi}erf\xi}\exp\left(-\xi^2\right) - \frac{A_{TiB}^f\left(C_{2,1}-C_{2,3}\right)}{\xi\phi_1\sqrt{\pi}\left(erf\eta - erf\left(\phi_1\xi\right)\right)}\exp\left(-\phi_1^2\xi^2\right) -$$
$$\frac{A_{Ti}^f C_{2,1}}{\xi\phi_2\sqrt{\pi}}\exp\left(-\phi_2^2\xi^2\right) \tag{5.36}$$

Similarly, plugging in Eqns. (5.21) and (5.35) in Eqn. (5.27), we get,

$$\left(C_{2,3}-C_{3,2}\right)\frac{\eta\sqrt{D_2}}{\sqrt{t}} = \frac{D_2 A_{TiB}^f\left(C_{2,1}-C_{2,3}\right)}{\left(erf\eta - erf\left(\phi_1\xi\right)\right)\sqrt{\pi D_2 t}}\exp\left(-\eta^2\right) + \frac{D_3 A_{Ti}^f C_{2,1}}{\sqrt{\pi D_3 t}}\exp\left(-\phi_3^2\eta^2\right)$$

Rearranging the above Eqn.,

$$\left(C_{2,3}-C_{3,2}\right) = \frac{A_{TiB}^f\left(C_{2,1}-C_{2,3}\right)}{\eta\sqrt{\pi}\left(erf\eta - erf\left(\phi_1\xi\right)\right)}\exp\left(-\eta^2\right) + \frac{A_{Ti}^f C_{2,1}}{\eta\phi_3\sqrt{\pi}}\exp\left(-\phi_3^2\eta^2\right) \tag{5.37}$$

In Eqns. (5.36) and (5.37), except ξ, η and A_{TiB}^{f}, all other terms can be obtained from the literature. The B concentrations in TiB_2 and TiB are the weight percent of B in these phases. Diffusivities of B in TiB_2 and TiB at the boriding temperature (910 ˚C) are not available in the literature. However, these diffusivities were estimated from the work of Fan et al.[97] In that study, diffusivities of B in TiB_2 and TiB phases were expressed as normal Arrhenius relationship with the Q and D_0 values for B diffusion in the TiB_2 as 187.1 kJ/mol and 6.8 $\times 10^{-8}$ m^2/s, respectively. The corresponding values in the TiB phase are 190.4 kJ/mol and 437.6 $\times 10^{-8}$ m^2/s, respectively. Table 5.4 presents the B diffusivities in the boride phases at selected temperatures which were used in the present calculations.

To predict the accelerated kinetics of the boride layer growth near the transition temperature, in addition to the B diffusivities in boride phase (Table 5.4), the B diffusivity in Ti near the phase transition temperature is also needed. These data are not available but a reasonable estimate of this can be made from the anomalous diffusivities of Ti. As described in the literature review chapter, based on calculations following Sanchez [126] the anomalous self-diffusivity of Ti at 910 ˚C was determined to be the order of 1×10^{-13} m^2/s. Araki et al.[149] conducted diffusion experiments in Ti-2.1 wt% Al [2] system and determined the diffusivity of Al (5×10^{-14} m^2/sec at 950 ˚C) in Ti. These values are quite comparable suggesting that the "anomalous" solute diffusivity near transition temperature can be close to the "anomalous" self-diffusivity of Ti. Based on these, we make a reasonable assumption here that the B diffusivity near the phase

[2] For Ti-2.1 wt% Al system, the transition temperature will be higher than that of nonalloyed Ti as Al is an α-stabilizing agent. For Ti-3Al-2.5V (near α-alloy), the transition temperature is reported as 935±15˚C[*]. Noting that the alloy studied in this case does not have any β-stabilizing element like V, it can be assumed that this alloy will have the transition temperature somewhere near 950˚C.

[*] *Materials Properties Handbook, Titanium Alloys, ASM International, p. 265, (1994)*

Table 5.4: Diffusivity data for various phases.

T (˚C)	Diffusivity of B in TiB_2 (m^2/sec) [97]	Diffusivity of B in TiB (m^2/sec) [97]	Self-diffusivity of Ti (m^2/sec) [155,156]
850	1.34×10^{-16}	6.13×10^{-15}	9.0×10^{-17}
910	3.71×10^{-16}	1.73×10^{-14}	1.0×10^{-13}
950	6.92×10^{-16}	3.25×10^{-14}	1.1×10^{-13}
1050	2.78×10^{-15}	1.34×10^{-13}	2.5×10^{-13}

transition temperature is about the same as the anomalous self-diffusivity of Ti for the calculations. It is important to note this assumed B diffusivity value (1×10^{-13} m^2/s) is about six times higher than that in TiB (1.73×10^{-14} m^2/s) which is consistent with the mechanism of additional, and faster, diffusion accelerating the TiB whisker growth. Only by the faster diffusion of B through the Ti phase can the B atoms reach the tip of growing TiB whisker. If the B diffusivity is equal or less (which is very unlikely) then the anomalous diffusion would make no impact on the boride layer growth kinetics. With the diffusivities in Table 5.4, Eqn. (5.36) and (5.37) were solved simultaneously using a MATLAB code to evaluate the dimensionless growth parameters ξ and η. Once the growth rate constants were determined, the thicknesses of the TiB_2 and TiB layers can be computed using Eqn. (5.10) and (5.14) for different treatment times at 910 ˚C.

A key variable in the prediction of accelerated kinetics is the area fraction of TiB and Ti phases, A_f^{TiB}, A_f^{Ti},respectively, in the plane perpendicular to the growth direction. Experimental determination of this was difficult; therefore some reasonable assumptions were made. In the microstructures of coating obtained after 24 hours at 910˚C (Figure 5.9(b)), the A_{TiB}^f of TiB whiskers seemed to be certainly more than about 0.75. Therefore,

it was considered reasonable to vary the A_{TiB}^{f} between 0.75 and 0.95 with the A_{Ti}^{f} between 0.25 and 0.05. This is acceptable, because the TiB layer consisted of a high concentration of TiB whiskers separated by some small amount of Ti in between (Figure 5.9). In the calculations, it was observed that as the A_{TiB}^{f} increased, the thickness of the total boride layer, after a given diffusion time, decreased as shown in Figure 5.16(a). This is consistent, because the decrease in A_{Ti}^{f} reduces the size of Ti-region and hence the amount of B atoms that diffuse "anomalously" and form the additional TiB at the tip of growing TiB whiskers.

Figure 5.16(b) shows the comparison of the predictions of accelerated kinetics with the experimental data. It has been found that for a good agreement with the experimental data the A_{TiB}^{f} and A_{Ti}^{f} values needed to be assumed as 0.85 and 0.15, respectively. For a proper comparison, the experimental data were corrected to remove the TiB growth (about 15 um) that had occurred during the heat up (10°C/min) period to 910˚C. To put the present theory and experiments on acceleration of kinetics in proper perspective, Figure 5.16(b) also shows the predictions of the total boride layer growths at 850 and 910˚C excluding the contribution from the anomalous B diffusion through the Ti phase. It can be seen that at 850˚C, the predicted layer growth agrees well with experimental data, as it should, because the kinetics at 850°C are not influenced by anomalous B diffusion in Ti. However, the prediction for 910˚C, without the inclusion of the growth contribution due to anomalous B diffusion in Ti, clearly under predicts the experimental data. This confirms that the accelerated kinetics of TiB layer growth at 910˚C is necessarily due to the additional growth provided by the B diffusion in Ti phase. The additional growth contribution diminishes as the diffusion temperature deviates from

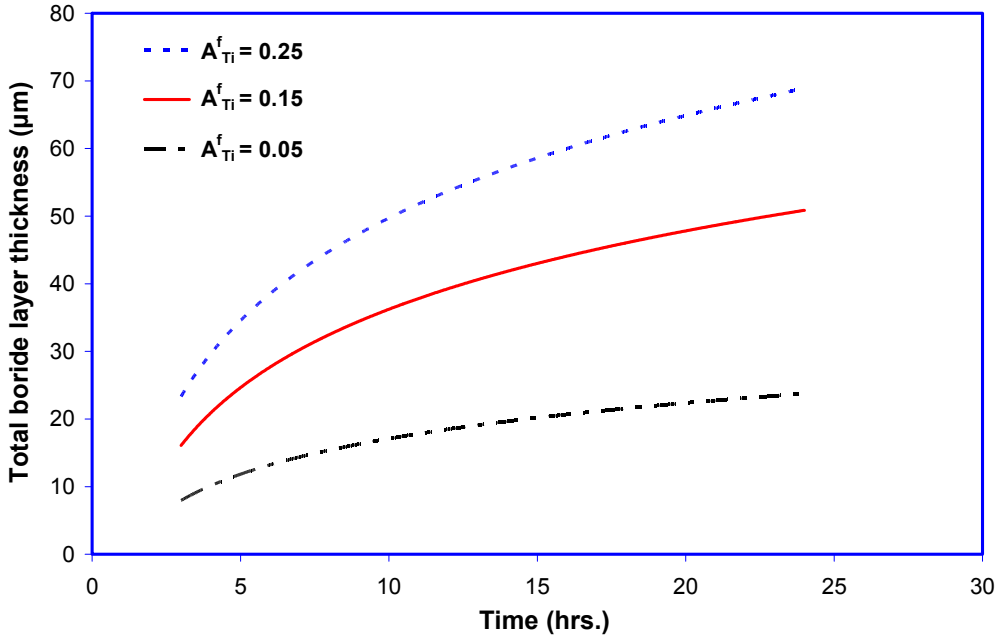

(a)

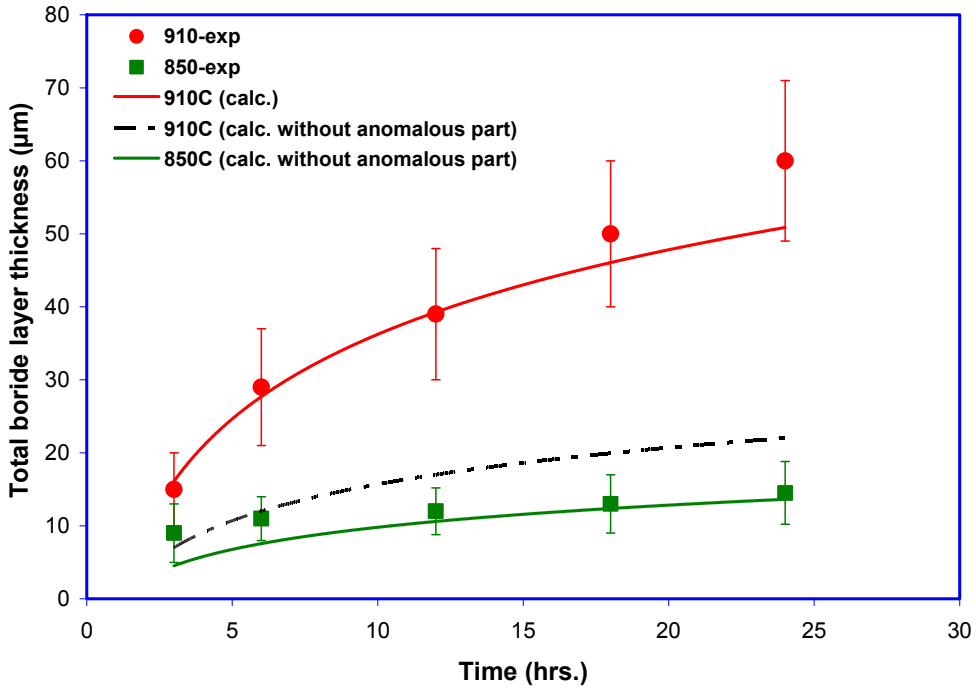

(b)

Figure 5.16 The predicted boride layer thicknesses 910˚C with varying area fractions of TiB and Ti phases **(a)**. Comparison of the predicted boride layer growth in Ti at 910˚C with and without the anomalous component, along with the experimental data **(b)**. For reference, the predicted and experimental data for 850˚C and without the anomalous part are also included.

the phase transition temperature, consistent with the experimental data in Figure 5.10.

5.3 Isothermal diffusion saturation of boron in boride layers

5.3.1 Premise

In general, the kinetics of boride layer growth in Ti during isothermal diffusion conditions are limited because of the sluggish diffusion of B in the high melting boride compounds such as TiB_2 or TiB. The kinetics of growth of these layers primarily depends on two parameters: treatment temperature and exposure time. Higher treatment temperatures lead to deeper layer growth due to higher diffusivities of B in the boride phases. However, the extent to which these two parameters affect the coating growth kinetics depends on whether boriding experiments are done in α-phase, β-phase or near α/β phase transition temperature of Ti. For example, boriding at 1050 ˚C (β-phase) imparts 93% higher coating growth than at 850 ˚C (α-phase) for a given treatment time (24hrs.).[104] However, the coating thickness obtained at 910 ˚C in 24 hours is higher (~39%) compared to 1050 ˚C for same duration of time. The effect of the exposure time on overall coating thickness also varies depending on the phase domain of Ti in which boriding experiments are done. An increase in coating thickness of 21% was observed [104] by increasing the exposure time from 3 hours to 24 hours at 850 ˚C. Boriding treatments in β-phase of Ti resulted in much increase (74% at 950 ˚C and 80% at 1050 ˚C) in thicknesses during similar increase in treatment times. One the other hand, near the phase transition temperature (910 ˚C), layer thickness achieved during 24 hours of treatment time was the highest among all conditions compared to that obtained in 3 hours.

This section has been treated differently from the earlier section for two reasons, the first and primary reason being that the oxygen content of the Ti specimen used for this study is 0.12 wt% while the previous one was 0.17 wt%. Since the oxygen content plays an important role in deciding the location in which the sample is going to be held in the α + β phase field during the near tarsus boriding experiments. From the Ti-O phase diagram (Figure 2.3), it appears that Ti sample containing 0.12 wt% O will be somewhere in the middle of the α + β phase field domain if boriding is performed at 900 ˚C. Hence it would be interesting to find out how this phase proportions will impact the layer growth kinetics. The second reason is that the isothermal B diffusion experiments were carried out for longer times to establish if there is any effect of the phase domain on the saturation of layer growth kinetics.

This work concentrates in analyzing titanium layer growth kinetics in CP-Ti substrates during isothermal boriding in the α, β-phase and near the α + β phase field of Ti for extended period of time. The relative growths of the TiB_2 and TiB layers and their dominance over the total layer thickness will be analyzed.

5.3.2 Results and discussion

The summary of thicknesses of TiB_2 layer and total (TiB_2 + TiB) boride layers obtained at all the treatment temperatures and times are listed in Table 5.5. The layer thicknesses corresponding to 3-24 hours of boriding at 850 and 1050 ˚C were also referred [104] for comparison. In the present work, B diffusion up to 71 hours at 850, 900 and 1050 ˚C was also performed to establish clearly the effect of B diffusion temperature at relatively longer time periods on layer growth kinetics. At all temperatures and at the longer times than before, still dual boride layer structure formed comprising of an outer

Table 5.5 Comparison of TiB_2 and total (TiB_2+TiB) coating thicknesses obtained in varied phase fields of Ti during isothermal treatments. The thickness values shown as italics were taken from ref [104] for comparison.

Time (hr)	850°C		900°C		1050°C	
	TiB_2 (µm)	**Total (µm)**	**TiB_2 (µm)**	**Total (µm)**	**TiB_2 (µm)**	**Total (µm)**
3	*1.5*	*23*	1.5	30	*5*	*31*
6	*2.7*	*24*	2.1	42	*10*	*37*
12	*3.2*	*25*	3.2	48	*12*	*41*
18	*3.3*	*26*	3.6	55	*15*	*50*
24	*3.9*	***28***	3.8	**63**	*17*	***54***
48	3.7	**30**	3.9	**102**	20	**55**
71	3.9	**31**	4.0	**108**	11	**55**

TiB_2 layer followed by TiB whisker layer, although there were some differences in the boride structure.

The SEM micrographs of samples borided at 850 ˚C for 24, 48 and 71 hours are shown in Figure 5.17. A continuous outer layer of TiB_2 followed by TiB whiskers into the depth of the substrate is seen in all the samples. The TiB_2 layer is continuous and its thickness is almost constant even during the increase in treatment time from 48 to 71 hours (Table 5.5). The TiB whiskers have needle-like morphology extending into the substrate. The sizes of TiB whiskers are of the order of 10-100 nm, indicating clearly that these are nanostructured. The total layer thickness also does not seem to increase with the increase in the treatment time from 24 to 71 hours. The comparison of the micrographs also suggests that there is no significant change in the area density of TiB whiskers with increase in treatment time. It appears that B diffusion reached saturation at

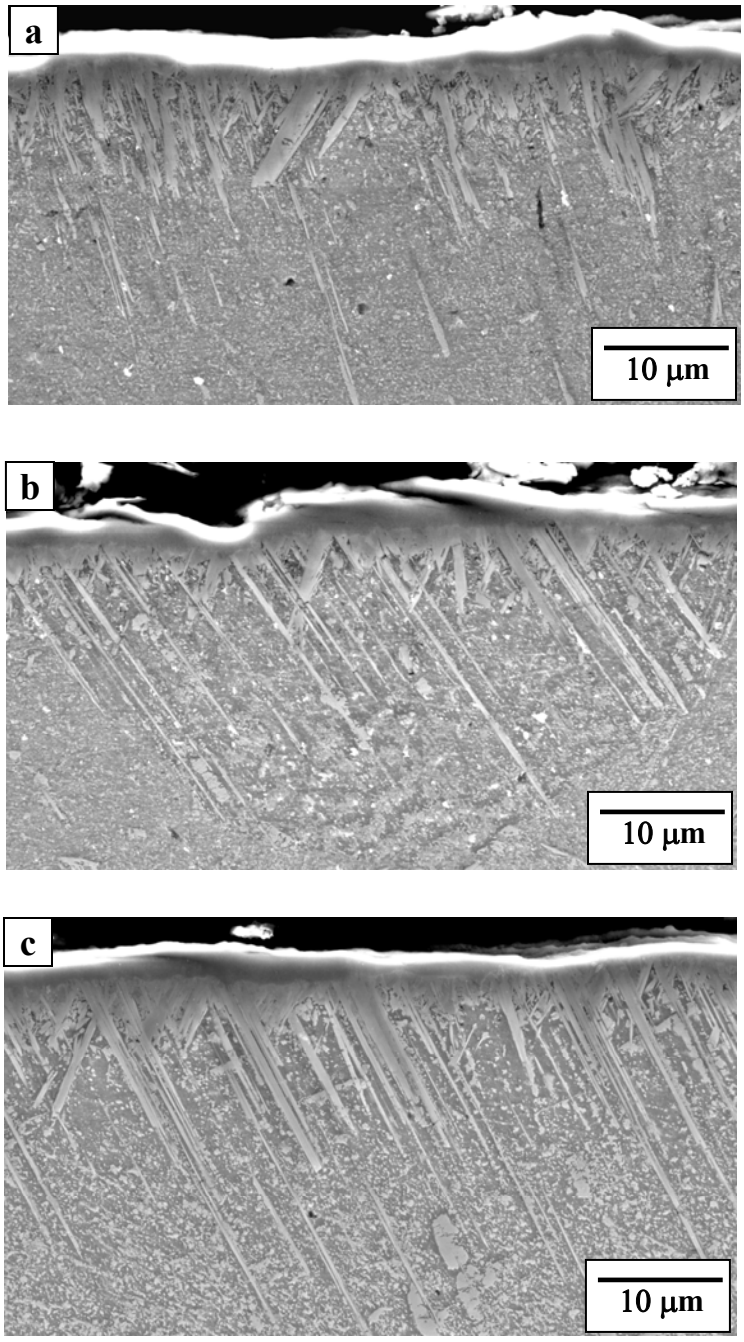

Figure 5.17 SEM micrographs of boride coating on grade 2 CP-Ti after isothermal treatments at 850 °C for **(a)** 24 hours, **(b)** 48 hours, and **(c)** 71 hours.

24 hours after which no additional growth occurred or the area density of TiB layers changed.

Figure 5.18 shows the SEM images of samples borided at 1050 °C for 24, 48 and 71 hours, respectively. In these samples, a thicker TiB_2 layer is observed compared to that observed at 850 °C. The increase in the TiB_2 layer thickness is only about 3 μm during the increase of boriding time from 24 to 48 hours. A rather unusual result is that the thickness of this layer decreased by about 50% after 71 hours of treatment compared to that at 48 hours. This may be because of depletion of B source in the powder pack upon long exposure (71 hrs.), but this could not be verified. The SEM micrograph (Figure 5.18(c)) shows that the TiB_2 layer was actually converted to TiB and the interface between TiB_2/TiB has moved into the TiB_2 layer compared to the structure at 24 and 48 hours. Similar behavior was reported [85] in the case of iron boriding, where the outer FeB layer was completely consumed leaving only the Fe_2B whisker layer upon boriding at 850 °C for 120 minutes. The behavior of growth of TiB layer at 1050 ˚C also seems to be different from that at 850 °C. In particular, the size ranges for the TiB whiskers at 1050 °C are very different from that at 850 °C. The TiB whiskers are relatively thicker after 24 hours (Figure 5.18(a)) and it seems that as the treatment time was increased to 48 and 71 hours, there was even more thickening of these whiskers (Figure 5.18(b and c)). The size range of the TiB whiskers in 48 and 71 hours treated samples seems to be between 2-10 μm. The possible reason behind the thickening of TiB whiskers at higher boriding temperatures (1050 °C), especially in the β-phase of Ti, was discussed in the earlier section of this chapter. When the whisker aspect ratio reaches about 10, thickening of TiB whiskers provides a faster means of transporting B and reacting with Ti, as opposed to

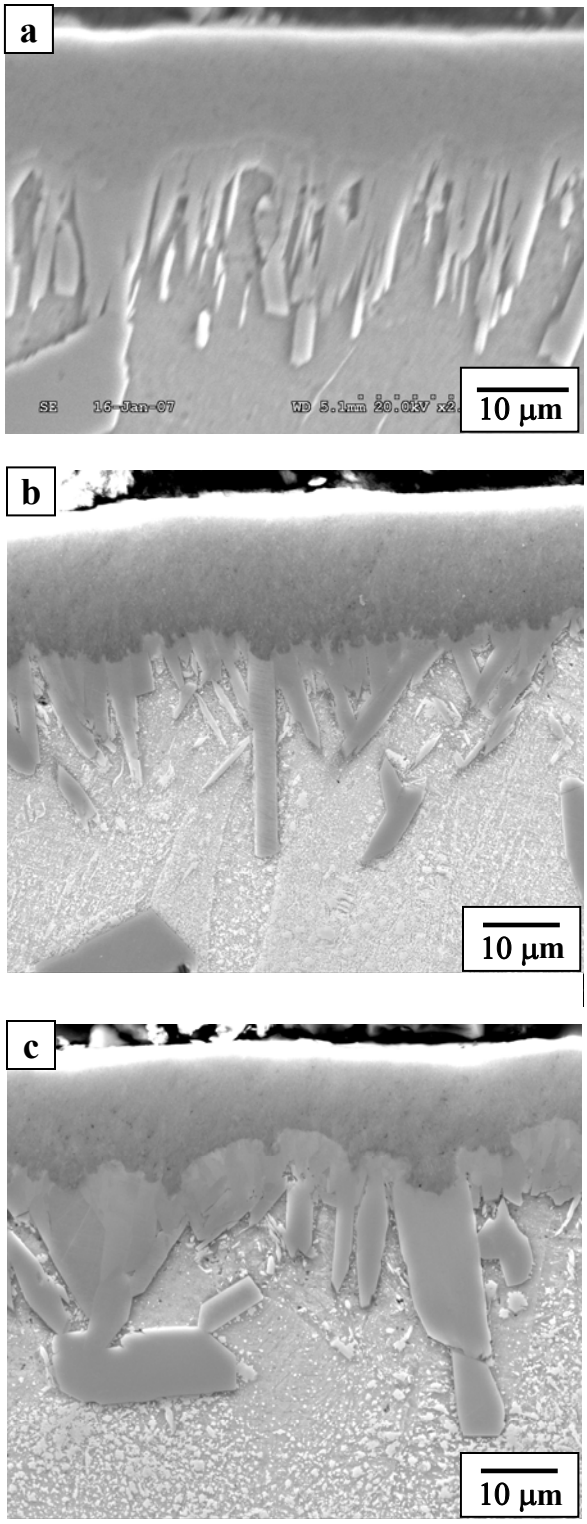

Figure 5.18 SEM micrographs of boride coating on grade 2 CP-Ti after isothermal treatments at 1050 °C for **(a)** 24 hours, **(b)** 48 hours, and **(c)** 71 hours.

the axial transport and extension of these whiskers. The contribution of the TiB whisker layer thickness to the total layer thicknesses is relatively less compared to that at 850 °C. The growth rate of the layers does not seem to increase with increase in boriding time from 24 hours to 71 hours which is very similar to the case of boriding at 850 ˚C. This is clearly evident from the SEM micrographs.

A very intriguing result is seen in the samples borided near the α/β transition temperature (900 ˚C), especially for the treatment times of 48 and 71 hours. This temperature is expected to lie somewhere in the middle of the α + β phase field of Ti, since presence of O induces a two phase field region (Figure 2.3). Although the SEM micrograph for the 24 hours treated sample (Figure 5.19(a)) shows a relatively deeper boride layer compared to that at 850 and 1050 ˚C, the growth at 900 °C does not seem to get saturated at this treatment time. Figure 5.19 (b) and (c) show the structure of boride layer formed during 48 and 71 hours treatment at 900 ˚C, respectively. Clearly much deeper coating layers are observed in these two conditions. The coating thicknesses obtained in 48 and 71 hours are in excess of 100 μm and with respect to the thickness after 24 hours, this corresponds to an increase of approximately 90%. The morphological aspects of the TiB whiskers in 48 and 71 hours samples are similar to that of 24 hours– the TiB coating structure is constituted of very thin TiB whiskers. The thicknesses of the TiB_2 layers at 900 °C are relatively small (~ 3 - 5 μm) irrespective of the treatment time. Since the growth of the TiB layer is driven by the B diffusion from the TiB_2 layer, the relatively lesser thickness of the TiB_2 layer can be understood.

The TiB_2 layer thicknesses are plotted as a function of time in Figure 5.20 (a). The total coating thicknesses (TiB_2 + TiB) are plotted in Figure 5.20 (b). The growth of

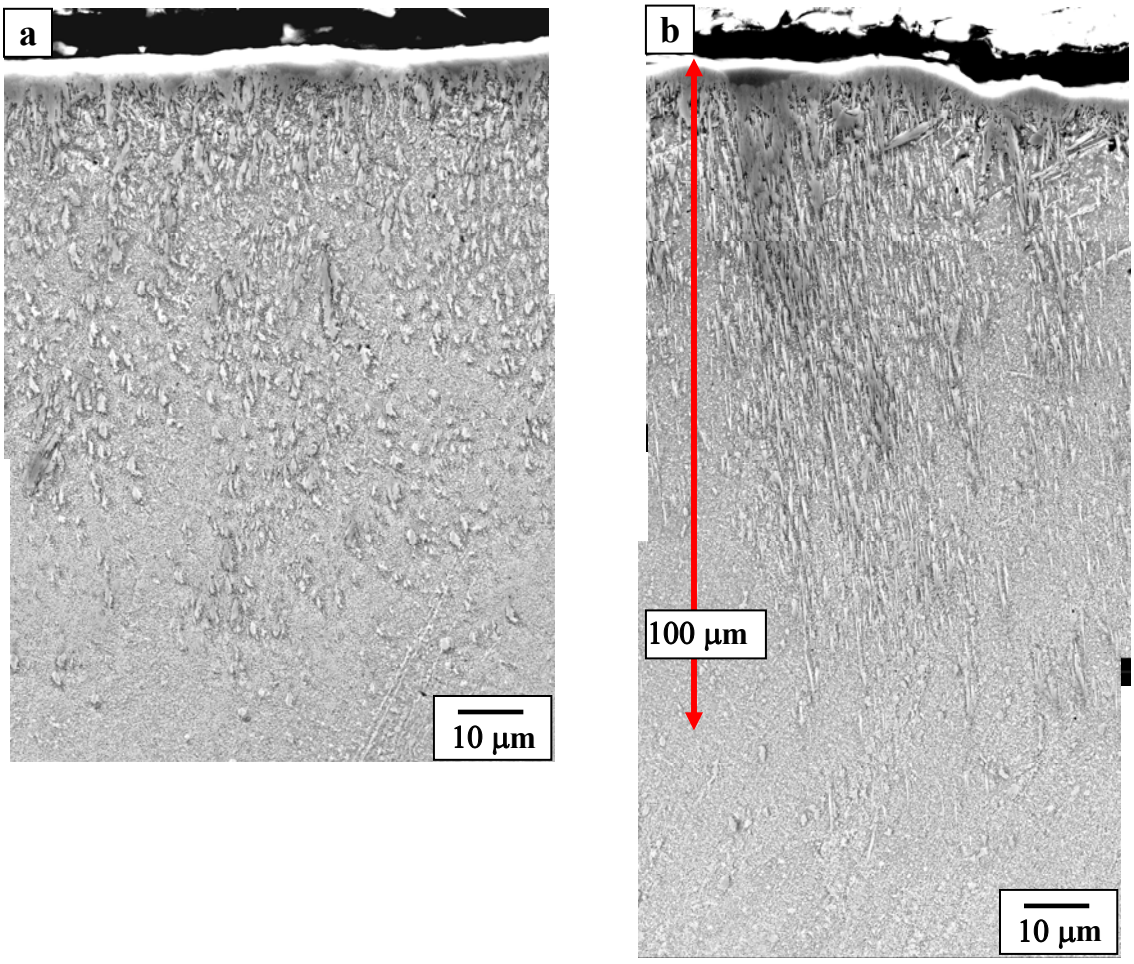

Figure 5.19 SEM micrographs of boride coating on grade 2 CP-Ti after isothermal treatments at 900 °C for **(a)** 24 hours, **(b)** 48 hours and **(c)** 71 hours.

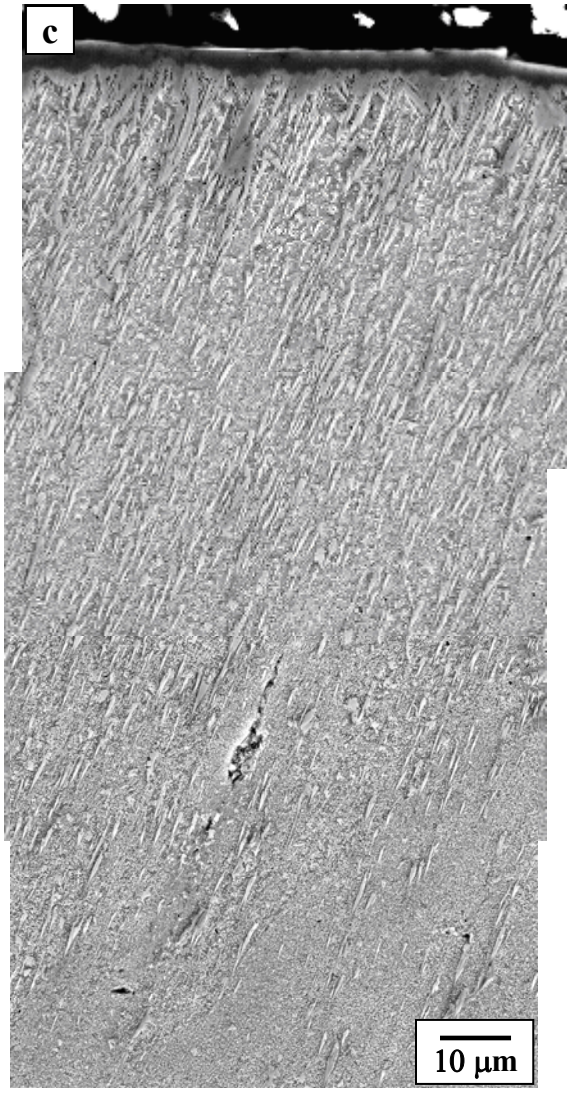

Figure 5.19 continued

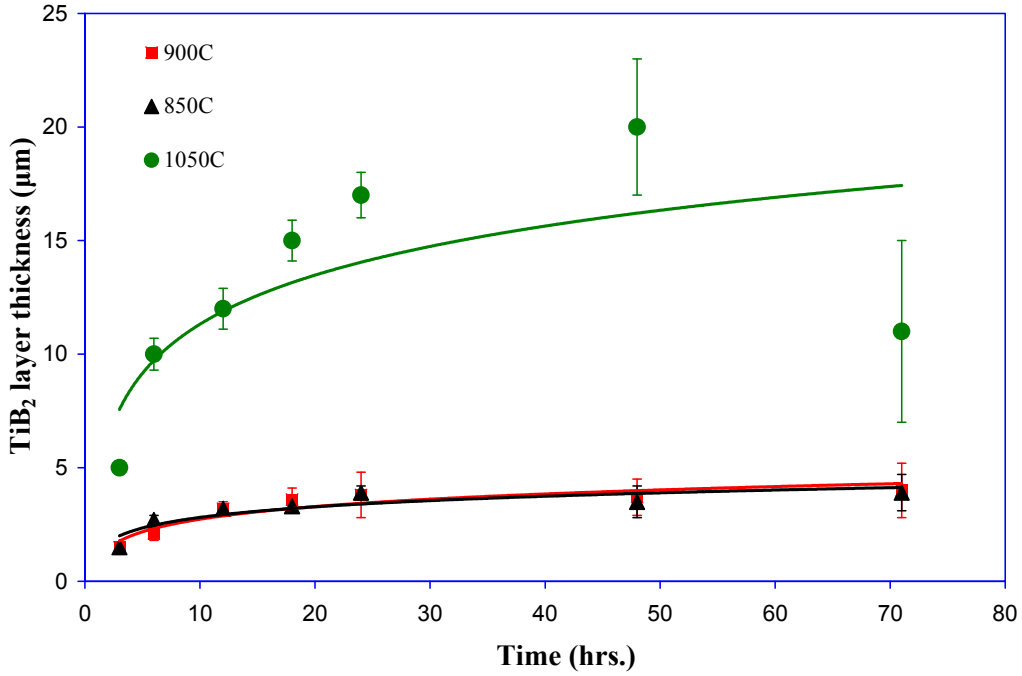

(a)

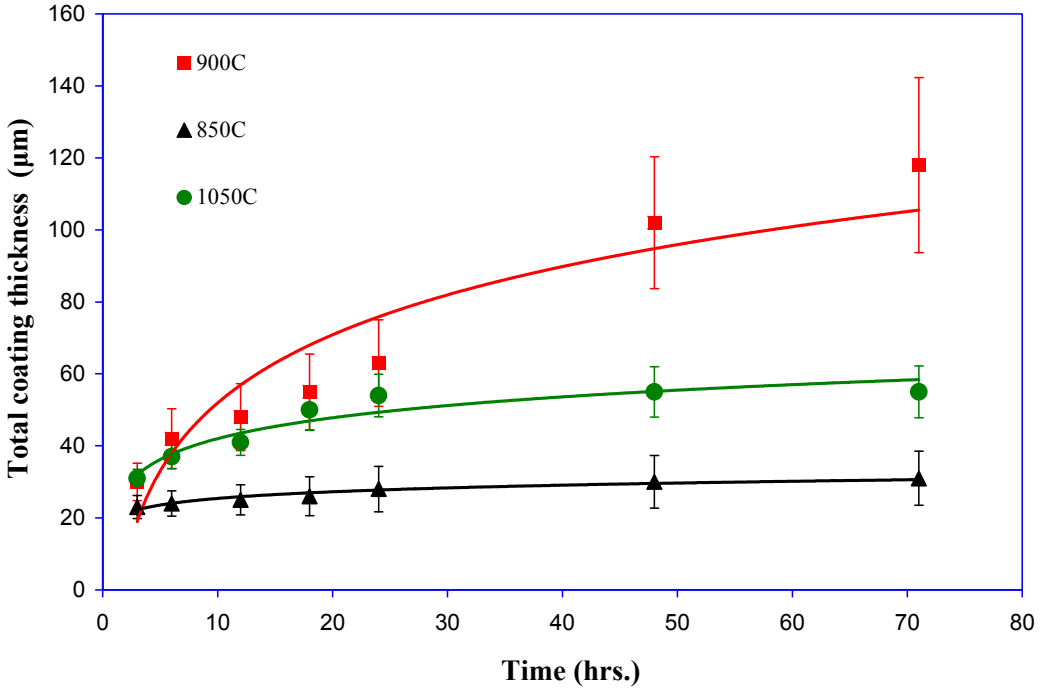

(b)

Figure 5.20 Coating thicknesses obtained for **(a)** TiB_2 and **(b)** total (TiB_2+TiB) layers in isothermal diffusion treatments plotted as a function of total time.

the TiB_2 layer at 1050 ˚C shows deviation from the parabolic form of diffusion kinetics after 48 hours of treatment– the probable reason (B depletion) for this was described earlier. For the other two temperature conditions, however, the parabolic form can been observed (Figure 5.20 (a)). With the exception of the 71 hours condition, TiB_2 layer thicknesses at 1050 °C are higher by a factor of 3 to 5, relative to those at 850 and 900 ˚C. However, the degree of TiB_2 layer growth at 900 °C is nearly comparable to that at 850 °C. On the other hand, the contributions of the TiB layer thicknesses towards the total coating thicknesses are higher at 900 ˚C (~ 95% of the total coating thickness is TiB in 71 hour).

The results here can have significant impact on boriding of Ti and its alloys. The isothermal growth limitation of boride layers can be overcome by boriding near the transition temperature. This is also economical because significantly higher thicknesses can be achieved at a relatively lower temperature.

In the previous section, the mechanism behind the accelerated coating growth kinetics near the transition temperature was analyzed based on 'anomalous' diffusion characteristics of Ti and its effect on diffusion of B in Ti-matrix. It is to be noted that the B diffusion behavior within the boride phases is not expected to be influenced by the diffusion anomaly in Ti near the transition temperature. The growth of these phases is solely determined by the diffusion of B through these phases–the diffusivities of B in these phases are well described by the Arrhenius type relationship (the activation energy (Q) values of 187 and 190 kJ/mol in TiB_2 and TiB, respectively,[97] and the respective pre-exponential factors (D_0) are 6.8×10^{-8} and 4.38×10^{-6} m^2/s). This should also be the case when boriding is done close to the transition temperature. Based on B diffusion alone in

the boride phases at 900°C for 24 hours, the expected layer thicknesses are about 8 and 35 μm for the TiB_2 and TiB phase, respectively. Hence, the B diffusion through the TiB phase alone can not explain the layer thicknesses obtained close to the transition temperature. Therefore, additional B diffusion mechanisms should be invoked. The TiB_2 is a solid monolithic phase; the growth of this phase solely depends on the B diffusion through this phase at 900 °C. The enhanced growth kinetics seem to be by the TiB sub-layer as this layer is in immediate contact with the Ti-matrix, as seen in the SEM micrographs. It is possible that if faster B diffusion paths exist in the Ti-phase between the whiskers, this might explain the increased growth kinetics of TiB at 900 °C. The notion of anomalous diffusion at β transus is not invoked here, since 900 °C is approximately in the middle of the α + β field.

The question is how the diffusivity of B is increased in the Ti-matrix in the α + β phase field. In fact, the reason for the increased self-diffusivity of Ti near the phase transition temperature is not properly established. Without disregarding the role of anomalous B diffusion in Ti-phase, we explore an additional B diffusion mechanism. This is the diffusion of B through the α/β interphase boundaries. Both α and β phases are expected to exist in a metastable state near the phase transition temperature– the volume fractions of these phases are determined by the temperature in the α + β phase field. Ti undergoes complete phase transformation from α to β phase though a range of temperatures (Figure 2.3). When the specimen is held at a temperature just above the α to α+β transus line, the volume fraction of the β phase would be less compared to when it is held just below the α+β to β transus line. Nevertheless, depending on the temperature, a high amount of the interphase boundaries between α and β phases are expected to be

present. These boundaries may act as a faster diffusion path for B diffusion than the phase boundaries or through the bulk. In some metals and alloys including Ti, higher diffusivities of the diffusing species, up to two orders of magnitude, were found due to diffusion through the interphase boundaries.[157, 158] In a diffusion study of C and Ni radioactive isotopes in Ti alloys, Bokshteyn et al.[157] reported a relatively higher diffusivities of these elements in the Ti matrix due to diffusion through the α/β interface boundaries. Especially, their experiments involving diffusion of Ni isotopes in a Ti alloy containing 10% β-phase demonstrated that the diffusion coefficients along the interphase boundaries are 3-4 orders of magnitude higher than diffusion coefficients in the β-phase and 4-5 orders of magnitude greater than that in the α-phase. It is to be noted that this is comparable to the enhancement due to anomalous diffusion (Section 5.2). In a different study,[158] the diffusion of Ni isotope in cast iron containing 10-40 μm size graphite particles and Sn isotope in Babbitt (bearing alloy of Cu-Sn-Sb) alloy containing up to 100 μm size SnSb intermetallic particles were performed. Accelerated diffusion of both isotopes was noticed through the matrix-intermetallic phase boundaries. For example, Ni diffusion along the ferrite-graphite phase boundaries at 600 ˚C was approximately 4 to 5 times faster than that along the grain boundaries and through the bulk of the ferrite phase. The relatively higher diffusivities along the phase boundaries were suggested to exist because of dislocations and vacancy concentrations that are present along the phase boundaries. It is beyond the scope of this research to explore the level of dominance of the inter-phase boundaries on B diffusion in Ti, but it is assumed here that they can play a very important role in accelerating B diffusion and thereby enhancing the growth kinetics of the TiB layer close to the transition temperature.

It is rather interesting to note that the enhancement of B diffusion through the α/β interphase boundaries in Ti can be of the same order of magnitude as anomalous diffusion. Therefore, a similar effect is seen here at 900 °C, compared to the result at 910 °C in the anomalous diffusion conditions (Section 5.2). It is not possible, due to the limited scope of the study, to distinguish between the two phenomena, but either can explain the accelerated growth kinetics near the phase transition temperature.

5.4 Mechanism and kinetics of growth of titanium boride layers under cyclic-phase-change-diffusion (CPCD)

5.4.1 Premise

The isothermal diffusion kinetic limitations may be overcome and large ingress and supersaturation of B in the subsurface layers of titanium may be realized by cyclic-phase-change-diffusion (CPCD) process. This may lead to more extensive subsurface TiB phase formation and a much higher coating thickness. The basic hypothesis of this process is that if reversible phase transformations were induced in titanium surface layers at the same time as B diffusion, the transformation could effectively "pump" more B into subsurface layers and could lead to subsurface supersaturation with B.

Grade 2 CP-Titanium undergoes α to β phase transformation around a temperature of about 913 ˚C. Thermally cycling the specimen across the α/β transition temperature, such that the specimen surface enters the α or β phase fields repetitively for short periods of time should lead to large B supersaturation in Ti subsurface layers. The solubility of B in BCC β phase is higher than that in HCP α phase. When the specimen surface enters the β phase field, a relatively large amount of B can be dissolved in subsurface layers. This B can then be converted into TiB whiskers that are formed when the specimen

surface enters α phase field—this formation is encouraged by the low solubility of B in α and the coherent crystallographic interface [92] between α-Ti and the TiB phase. Even at temperatures close to 900 ˚C, the α phase shows very little solid solubility for B. Thus, any B present should readily phase separate into TiB phase which grows as pristine, long whiskers, embedded in α-phase.

The mechanistic basis for the CPCD treatment employed here is quite different from the cyclic heat treatments intended to change the bulk microstructure. In the CPCD treatment, the emphasis is the complete cyclic traversing of the phase transition temperature such that large ingress and supersaturation B can be facilitated when the surface layers enter a high temperature phase (β). Subsequently a hard phase (TiB) is precipitated when the layers traverse into the low temperature phase (α).

5.4.2 Subsurface temperature profiles during CPCD

The cyclical variations in surface temperature lead to oscillating subsurface temperatures creating a zone of excess heat (*heat-packet*) that can be made to travel from surface to the interior during each thermal cycle. This *heat-packet* is the region of the subsurface that is relatively at a higher temperature than the mean temperature of the thermal cycle. The nature of how this occurs can be illustrated by examining the effect of harmonic surface temperature variations on the subsurface temperature distributions in a given solid. The differential equation governing the one-dimensional heat transfer in a semi-infinite solid is:

$$\frac{\partial^2 T}{\partial x^2} = \frac{1}{\kappa}\frac{\partial T}{\partial t} \tag{5.38}$$

where T is temperature, κ is thermal diffusivity, x is distance from the surface and t is time. Here, the temperature (T) at the surface ($x = 0$) is a function of time. To obtain the temperature distribution inside the material for a given time-dependent temperature profile at the surface, Eqn. (5.38) is to be solved with appropriate boundary conditions. For the trapezoid shaped temperature profile as shown in Figure 5.21 which is employed in the thermal cycling experiments here, the subsurface temperature profiles can be determined by Fourier transformations.

The Fourier series can represent any periodic waveform that is not continuously differentiable in terms of sine and cosine functions. The Fourier transformation of an arbitrary wave, *f(θ)* can be written as,

$$f(\theta) = f_{mean} + \sum_{n=1}^{\infty} \left(a_n \cos(n\theta) + b_n \sin(n\theta)\right) \tag{5.39}$$

where $a_n = \frac{1}{\pi} \int_{-\pi}^{\pi} f(\theta)\cos(n\theta)d\theta$ n = 0, 1, 2…… (5.40)

and $b_n = \frac{1}{\pi} \int_{-\pi}^{\pi} f(\theta)\sin(n\theta)d\theta$ n = 1, 2…… (5.41)

where f_{mean} is the mean value of the waveform, a_n and b_n are the amplitudes of cosine and sine waves, respectively. θ is an independent variable that represents time here. Figure 5.21 shows the schematic of a trapezoidal wave starting from – π to + π and with a total period of 2π. The temperature profile is divided into various segments which are identified as **a** to **f**. The variations in temperature in each segment is then,

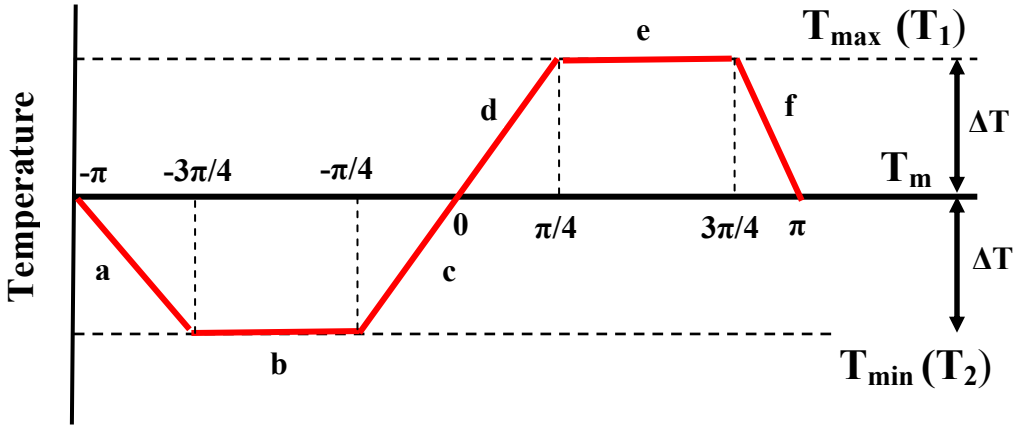

Figure 5.21 Schematic of temperature profile for single cycle as employed for cyclic boriding with different heat segments

Segment **a**: $$f_1(\theta) = (4T_2 - 3T_m) - \frac{4(T_m - T_2)}{\pi}\theta \quad \text{for } (-\pi \le \theta \le -3\pi/4) \tag{5.42}$$

Segment **b**: $$f_2(\theta) = T_2 \quad \text{for } (-3\pi/4 \le \theta \le -\pi/4) \tag{5.43}$$

Segment **c**: $$f_3(\theta) = T_m - \frac{4(T_2 - T_m)}{\pi}\theta \quad \text{for } (-\pi/4 \le \theta \le 0) \tag{5.44}$$

Segment **d**: $$f_4(\theta) = T_m - \frac{4(T_m - T_1)}{\pi}\theta \quad \text{for } (0 \le \theta \le \pi/4) \tag{5.45}$$

Segment **e**: $$f_5(\theta) = T_1 \quad \text{for } (\pi/4 \le \theta \le 3\pi/4) \tag{5.46}$$

Segment f: $$f_6(\theta) = (4T_1 - 3T_m) - \frac{4(T_1 - T_m)}{\pi}\theta \quad \text{for } (3\pi/4 \le \theta \le \pi) \tag{5.47}$$

Hence, the functions, $f_i(\theta)$ (i =1, 2,..6) are the temperature profiles at different time interval of the period. T_1, T_2 and T_m are the maximum, minimum and mean temperature of the thermal cycle as shown in Figure 5.21.

The trapezoid shaped waveform is an odd function [159] and hence, all the cosine co-efficient (a_n, n = 0, 1, 2..) in Eqn. (5.39) are zero leaving only the sine components. Hence, for the trapezoidal wave, Eqn. (5.39) becomes,

$$f(\theta) = f_{mean} + \sum_{n=1}^{\infty} \left(b_n \sin(n\theta)\right) \tag{5.48}$$

Now, only the co-efficients, b_n for the sine terms are to be evaluated for the temperature profile, which can be done by plugging in Eqns. (5.42) to (5.47) in Eqn. (5.41),

$$b_n = \frac{1}{\pi}\left[\int_{-\pi}^{-3\pi/4} f_1(\theta)\sin(n\theta) + \int_{-3\pi/4}^{-\pi/4} f_2(\theta)\sin(n\theta) + \int_{-\pi/4}^{0} f_3(\theta)\sin(n\theta) + \int_{0}^{\pi/4} f_4(\theta)\sin(n\theta) + \int_{\pi/4}^{3\pi/4} f_5(\theta)\sin(n\theta) \right.$$

$$\left. + \int_{3\pi/4}^{\pi} f_6(\theta)\sin(n\theta) \right] \tag{5.49}$$

Each term in the right hand side of Eqn. (5.49) can be evaluated by inserting $f_i(\theta)$ term from Eqns. (5.42) to (5.47), as,

$$\int_{-\pi}^{-3\pi/4} f_1(\theta)\sin(n\theta) = \left[-\frac{T_2}{n}\cos\left(-\frac{3n\pi}{4}\right) + \frac{T_m}{n}\cos(-n\pi) - \frac{4(T_m - T_2)}{n^2\pi}\sin\left(-\frac{3n\pi}{4}\right) \right] \tag{5.50}$$

$$\int_{-3\pi/4}^{-\pi/4} f_2(\theta)\sin(n\theta) = \left[-\frac{T_2}{n}\cos\left(-\frac{n\pi}{4}\right) + \frac{T_2}{n}\cos\left(-\frac{3n\pi}{4}\right)\right] \tag{5.51}$$

$$\int_{-\pi/4}^{0} f_3(\theta)\sin(n\theta) = \left[-\frac{T_m}{n} + \frac{T_2}{n}\cos\left(-\frac{n\pi}{4}\right) + \frac{4(T_2 - T_m)}{n^2\pi}\sin\left(-\frac{n\pi}{4}\right)\right] \tag{5.52}$$

$$\int_{0}^{\pi/4} f_4(\theta)\sin(n\theta) = \left[\frac{T_m}{n} - \frac{T_1}{n}\cos\left(\frac{n\pi}{4}\right) - \frac{4(T_m - T_1)}{n^2\pi}\sin\left(\frac{n\pi}{4}\right)\right] \tag{5.53}$$

$$\int_{\pi/4}^{3\pi/4} f_5(\theta)\sin(n\theta) = \left[-\frac{T_1}{n}\cos\left(\frac{3n\pi}{4}\right) + \frac{T_1}{n}\cos\left(\frac{n\pi}{4}\right)\right] \tag{5.54}$$

$$\int_{3\pi/4}^{\pi} f_6(\theta)\sin(n\theta) = \left[-\frac{T_m}{n}\cos(n\pi) + \frac{T_1}{n}\cos\left(\frac{3n\pi}{4}\right) + \frac{4(T_1 - T_m)}{n^2\pi}\sin\left(\frac{3n\pi}{4}\right)\right] \tag{5.55}$$

After evaluating Eqn. (5.49) using Eqns. (5.50) to (5.55) and following the general trigonometric relationships of sine and cosine functions [$\sin(-\theta) = -\sin(\theta)$ and $\cos(-\theta) = \cos(\theta)$], b_n can be written as,

$$b_n = \frac{4}{\pi^2}\left[\frac{(T_1 - T_m)}{n^2}\sin\left(\frac{n\pi}{4}\right) + \frac{(T_m - T_2)}{n^2}\sin\left(\frac{n\pi}{4}\right) + \frac{(T_1 - T_m)}{n^2}\sin\left(\frac{3n\pi}{4}\right) + \frac{(T_m - T_2)}{n^2}\sin\left(\frac{3n\pi}{4}\right)\right] \tag{5.56}$$

For the temperature profile, the amplitude of the profile (ΔT) is,

$$\Delta T = T_1 - T_m = T_m - T_2 \tag{5.57}$$

Incorporating Eqn. (5.57) in Eqn. (5.56),

$$b_n = \frac{8(\Delta T)}{\pi^2 n^2}\left[\sin\left(\frac{n\pi}{4}\right)+\sin\left(\frac{3n\pi}{4}\right)\right] \tag{5.58}$$

Substituting Eqn. (5.58) in Eqn. (5.48) and noting that $f_{mean} = T_m$ and $f(\theta) = T(\theta)$, the trapezoidal temperature profile at the surface becomes,

$$T(\theta) = T_m + \frac{8(\Delta T)}{\pi^2}\sum_{n=1}^{n=\infty}\left(\frac{1}{n^2}\left[\sin\left(\frac{n\pi}{4}\right)+\sin\left(\frac{3n\pi}{4}\right)\right]\sin(n\theta)\right) \tag{5.59}$$

The change in surface temperature distribution with time as described by Eqn. (5.59) is shown in Figure 5.22 along with the actual temperature profile measured by a thermocouple in a furnace where the cyclic temperature changes were imposed. Plugging $T(\theta)$ from Eqn. (5.59) in Eqn. (5.38), and following the solution method [160] the variation of subsurface temperature with time and depth from the surface is given by,

$$T(x,t) = T_m + \frac{8(\Delta T)}{\pi^2}\sum_{n=1}^{n=\infty}\left(\frac{1}{n^2}\left[\sin\left(\frac{n\pi}{4}\right)+\sin\left(\frac{3n\pi}{4}\right)\right]\exp\left(-x\sqrt{\frac{n\pi}{2\kappa\vartheta}}\right)\sin\left(\frac{n\pi t}{\vartheta}-x\sqrt{\frac{n\pi}{2\kappa T}}\right)\right) \tag{5.60}$$

where ϑ is the period of the thermal cycle.

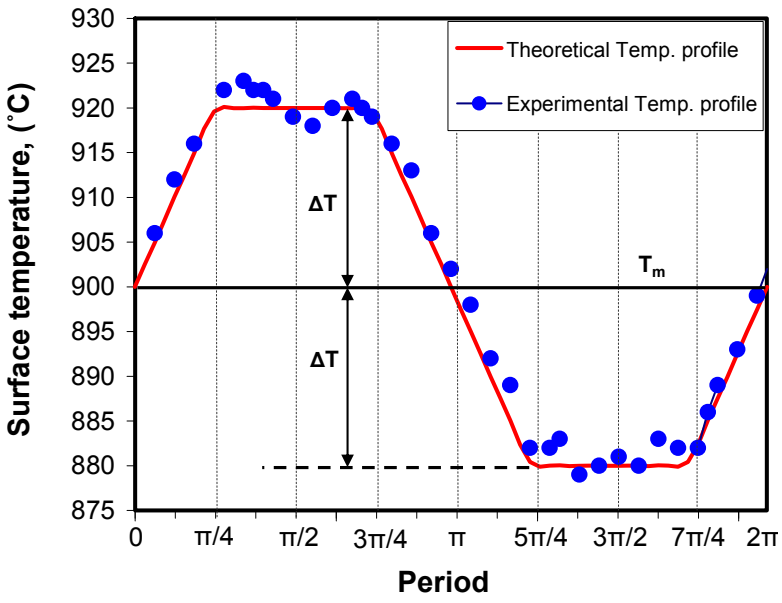

Figure 5.22 Variation of surface temperature with time

Normalizing the depth with a dimensionless parameter,[160] $\xi \left(= x\sqrt{\frac{\pi}{2\kappa\vartheta}} \right)$, Eqn. (5.60) can be written as:

$$T(x,t) = T_m + \frac{8(\Delta T)}{\pi^2}\sum_{n=1}^{n=\infty}\left(\frac{1}{n^2}\left[\sin\left(\frac{n\pi}{4}\right) + \sin\left(\frac{3n\pi}{4}\right)\right] \exp\left(-\xi\sqrt{n}\right)\sin\left(\frac{n\pi t}{\vartheta} - \xi\sqrt{n}\right)\right) \quad (5.61)$$

The temperature distribution from Eqn. (5.61) is plotted in terms of normalized distance, ξ in Figure 5.23. When the surface temperature is at T_{max} ($t/T = \pi/2$– as shown in Figure 5.22), the temperature decreases with distance and it is $T = T_m$ at $\xi = 1.6$. Then it dies down approaching the T_m in the bulk of the material. In the middle of the decreasing part of the thermal cycle ($t/T = \pi$), even though the surface temperature is T_m, the subsurface temperature up to about $\xi = 4$ is actually higher than T_m. This is because although the surface temperature has decreased to T_m, the excess heat below the surface due to the

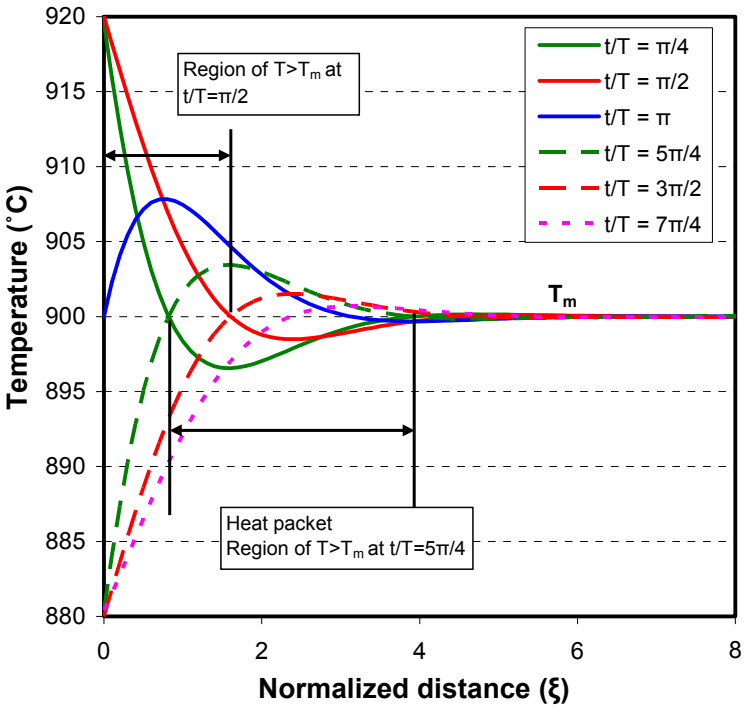

Figure 5.23 The subsurface temperature distributions corresponding to specific period of temperature cycle shown in Figure 5.22.

heating period of the cycle has not yet dissipated, leading to a *heat packet* (inside which $T > T_m$) formation in the subsurface region. With further surface cooling, say to about t/T = 5π/4 in Figure 5.22 (when the surface temperature reaches T_{min}), the peak temperature of the heat packet has shifted to the inside of the solid (Figure 5.23). This is the *transport* of the *heat packet*, even though the peak temperature of the packet itself is slowly diminishing with time. At this point of the thermal cycle, the region of $T > T_m$ extends from about $\xi = 0.8$ to about $\xi = 4.0$ and represents a subsurface region that is actually hotter than T_m, but bound by a relatively cooler surface layer ($0< \xi <0.8$) and the bulk ($4.0< \xi <\infty$). The *heat packet* almost dies down when the surface temperature is towards the end of the bottom of the thermal cycle (t/T = 7π/4). During the heat phase in the next cycle (t/T = 2π), the subsurface temperature increases again and sets up the conditions for

the transport of another *heat packet* during the subsequent cooling phase of the cycle. Thus, in each cycle, a *heat packet* (where $T > T_m$) is created at the surface at T_{max} and is transported into depth during cooling phase and dies down at some distance when $T= T_{min}$. This process repeats with the repetition of the cyclical variation in surface temperature.

The *heat-packet travel* as induced by the cyclic surface temperature variation can be exploited for large scale transport of B into Ti when the cyclic temperature variation is performed across the phase transition temperature. If the T_m is made to coincide with the phase transition temperature of Ti, above and below of which the solubility of B is higher and lower, respectively, then a large amount B atoms that would be soluble in the high temperature β-phase of Ti can be trapped inside the *heat-packet* and subsequently can be transported inside the bulk**.**

The cyclic variations in surface temperature during diffusion of B into Ti surface can lead to enhanced dissolution of B and subsequent precipitation as TiB phase during cooling thereby increasing the coating depth. The objective of this section is to perform B diffusion experiments with the temperature of the specimen cycled across the phase transition temperature. The kinetics of boride layer growth, the mechanical properties and the microstructural details of the layers are to be established.

5.4.3 Results and discussion

The average coating thickness values obtained during thermal cycling experiments are presented in Table 5.6. It is to be noted here that as the holding time at the limit temperatures is increased, the corresponding frequency of cycling decreases for the fixed total treatment times of 3,6,12,18 and 24 hours. The effect of holding time at the

Table 5.6 Summary of total coating thicknesses obtained in varied cyclic thermal treatments

Time* (hr.)	Coating Thickness (µm)									
	3		6		12		18		24	
	Total	SD	Total	SD	Total	SD	Total	SD	Total	SD
910C-890C-(0 min)	26	4	33	6	46	7	52	8	65	10
910C-890C-(6 min.)	24	3	32	4	47	5	54	9	64	11
910C-890C-(18 min.)	24	4	33	4	44	6	53	10	64	11
910C-890C-(30 min.)	28	7	35	8	48	10	55	10	67	12
910C-890C-(42 min.)	25	4	32	5	42	6	52	7	60	11
910C-890C-(60 min.)	23	7	30	9	41	10	53	9	60	11

* Time in thermal cycling conditions refers to the total time of treatment, with the sample being held at 890˚C and 910˚C for varying holding times at the limit temperatures.

limit temperatures and the number of thermal fluctuations (frequency) of cycling, on the total coating growth does not appear to be significant. For example, the thicknesses of the coating layers increased from about 25 µm to about 60 µm with the increase in total treatment time from 3 to 24 hours for all hold periods.

The optical and SEM micrographs of samples thermally cycled for hold times of 0, 30, 42 and 60 minutes at the limit temperatures are presented in Figures 5.24-5.27. Figures 5.24 (a-c) are the optical micrographs for samples borided for 12, 18 and 24 hours of total treatment time with 0 minute of holding time. Figure 5.24 (d) is the higher magnification SEM micrograph of the 24-hour sample. Figures 5.25-5.27 are also arranged in the same order for 30, 42 and 60 minutes hold times. From Figures 5.24-5.27, it can be seen that irrespective of the holding time at the limit temperatures, a thin layer

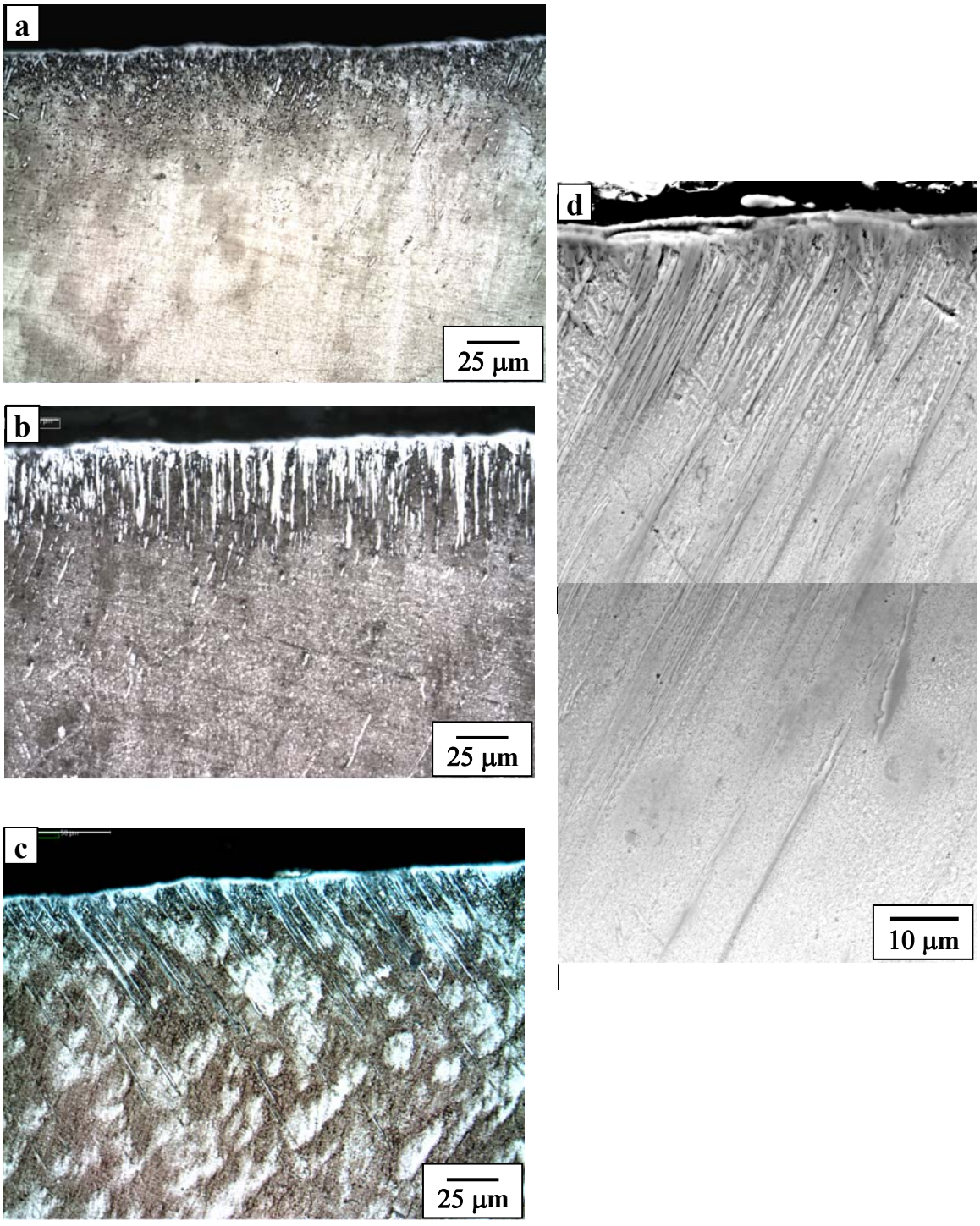

Figure 5.24 Optical micrographs of samples thermally cycled between 890-910C during B diffusion with 0 minute hold time for total time of **(a)** 12 hours **(b)** 18 hours **(c)** 24 hours **(d)** Higher magnification SEM micrographs for 24 hours treated sample.

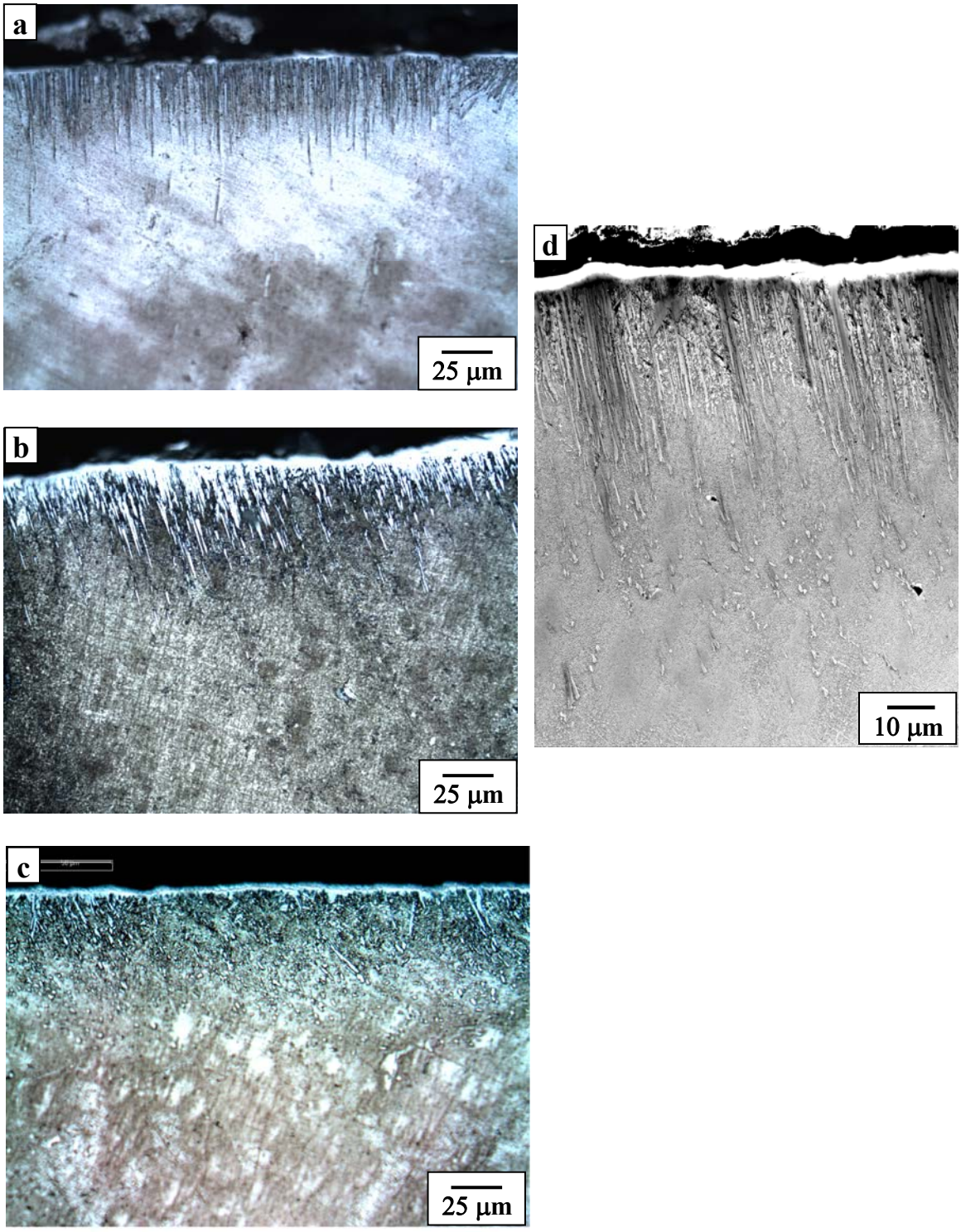

Figure 5.25 Optical micrographs of samples thermally cycled between 890-910C during B diffusion with 30 minutes hold time for total time of **(a)** 12 hours **(b)** 18 hours **(c)** 24 hours **(d)** Higher magnification SEM micrographs for 24 hours treated sample.

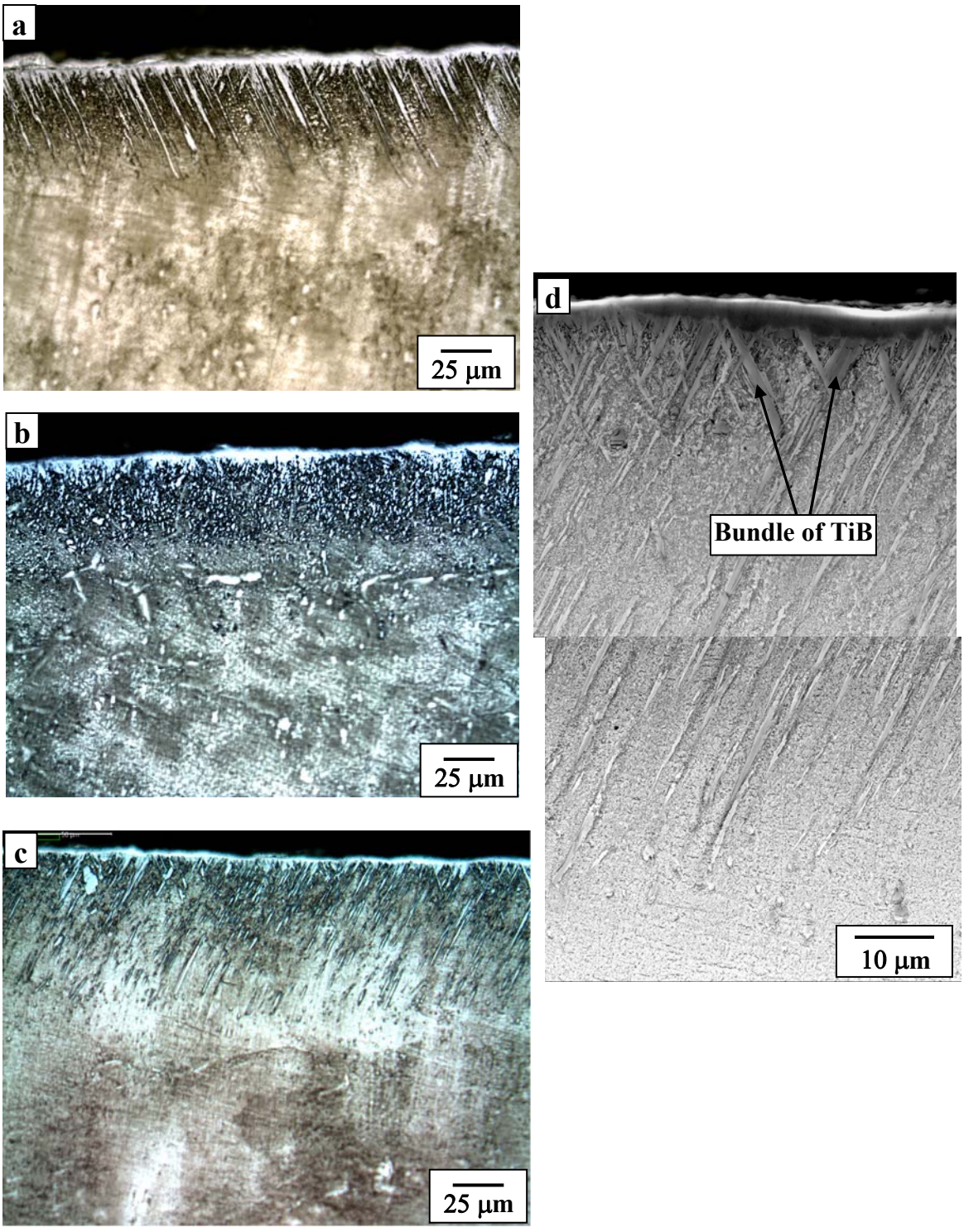

Figure 5.26 Optical micrographs of samples thermally cycled between 890-910C during B diffusion with 42 minutes hold time for total time of **(a)** 12 hours **(b)** 18 hours **(c)** 24 hours **(d)** Higher magnification SEM micrographs for 24 hours treated sample.

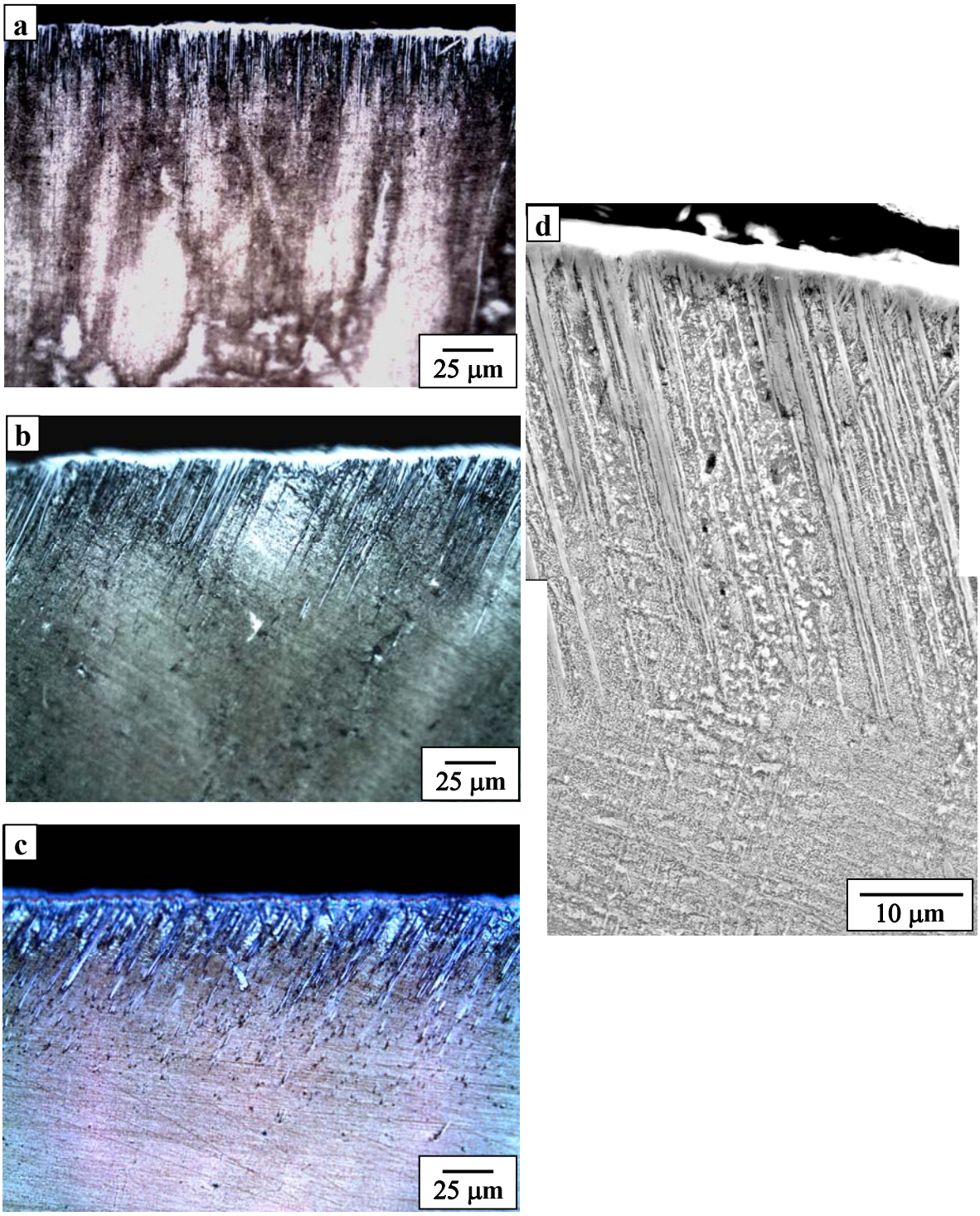

Figure 5.27 Optical micrographs of samples thermally cycled between 890-910C during B diffusion with 60 minutes hold time for total time of **(a)** 12 hours **(b)** 18 hours **(c)** 24 hours **(d)** Higher magnification SEM micrographs for 24 hours treated sample.

of TiB_2 formed on the top of the growing TiB whiskers. As the total treatment time is increased from 12 to 24 hours, the thickness of the TiB_2 layer seems to increase by a small amount. The thickness of the TiB_2 layer is of the order of 2-3 μm in all the 24-hour thermally cycled samples regardless of the hold time. The TiB layers in all samples are characterized by very thin whiskers penetrating deep into the substrate. The thicknesses of these whiskers are of the order of 10-100 nm with a very high aspect ratio. The presence of some isolated thick TiB whiskers can be seen clearly in Figure 5.26 (d). These thick TiB whiskers may be bundles of thin TiB whiskers which are yet to be confirmed. With increase in the total thermal cycling time from 3 to 24 hours, the penetration depth of the TiB whiskers increases from about 23 to 55 μm in all the cyclic conditions. Also, the area density of the whiskers within the TiB layer increased with an increase in the treatment time. The samples cycled for 24 hours showed a higher TiB area density compared to the samples cycled for shorter times. This trend is uniform across all hold time experiments.

The total boride layer thicknesses are plotted as a function of the total cycling time in Figure 5.28 for all the thermal cycling conditions. The growth kinetics at all temperatures seem to obey the parabolic behavior. The general trend is that the average total boride layer thicknesses increase with the increase in the total time of cycling. There does not seem to be any significant difference in coating thicknesses with change in the hold time at the limit temperatures.

Figure 5.28 also highlights the effect of thermal cycling during B diffusion in comparison with the isothermal treatments. The boride layer thicknesses obtained by cycling across the phase transition temperature for all combinations of hold time (at the

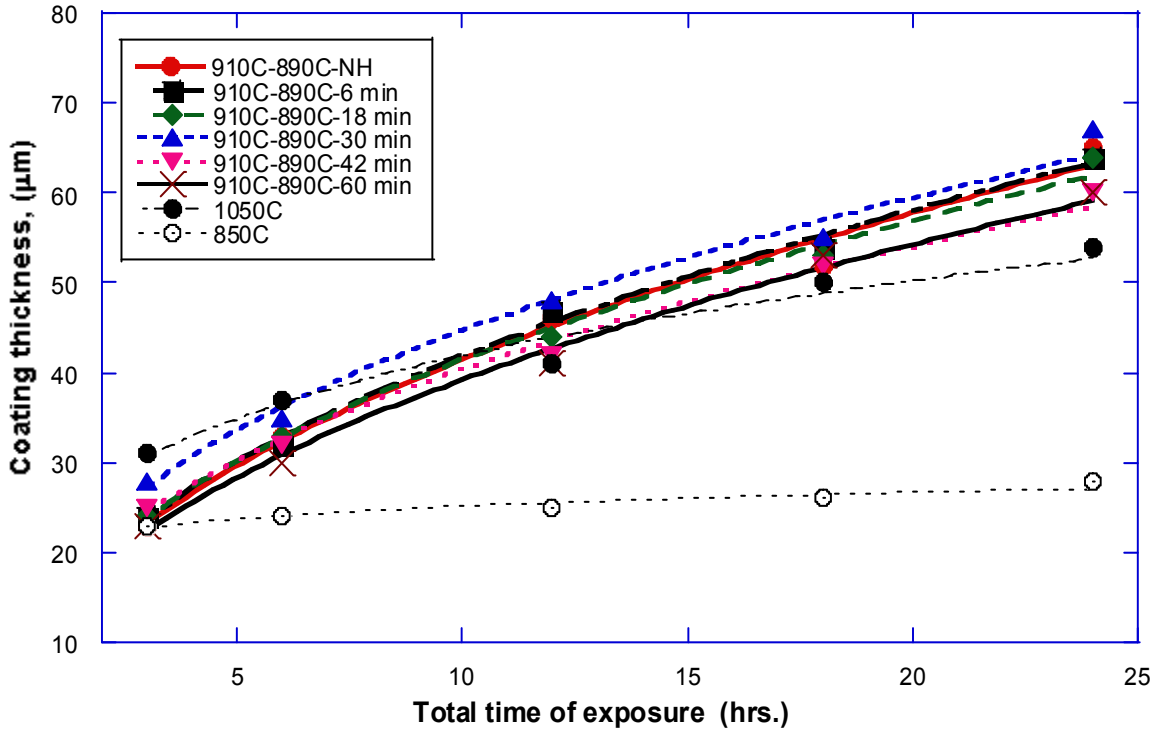

Figure 5.28. Total coating thicknesses obtained in cyclic boriding treatments plotted as a function of total exposure time.

limit temperatures) and frequencies of thermal cycling are on average, slightly higher than that of isothermal treatment at a higher temperature (1050 °C) in the β phase field (Figure 5.28). It is to be noted that the coating depth and the coating morphologies obtained through cyclic treatment are quite similar to that obtained by isothermal B diffusion near the phase transition temperatures (Figure 5.20(b)). Isothermal B diffusion at 900 °C for 24 hours leads to a total boride layer thickness of ~65 µm, which is comparable to that obtained after 24 hours of thermal cycling, for any hold time. This similarity is not expected. The reason for similar results is examined in the following discussion.

Although the idea of CPCD treatment is rooted on the requirement of the complete reversal from α to β phase in every thermal cycle, it turned out that this was not the case for 890-910 °C cycling performed with Ti containing 0.17 wt% O. Commercially pure titanium (CP-Ti) contains a small amount of oxygen; therefore, it is important to examine the location of the limit temperatures with respect to the phase boundaries, since these vary with the O content. Figure 5.29 illustrates the Ti-O phase diagram where the phase boundaries were demarked based on the work of Jaffee et al.[27] The presence of O actually introduces a α+β two-phase field with two transus temperatures, one for the phase transition from α to α+β field (α-transus) and the other from α+β to β field (β-transus). In the phase diagram, the oxygen content (0.17 wt%) of

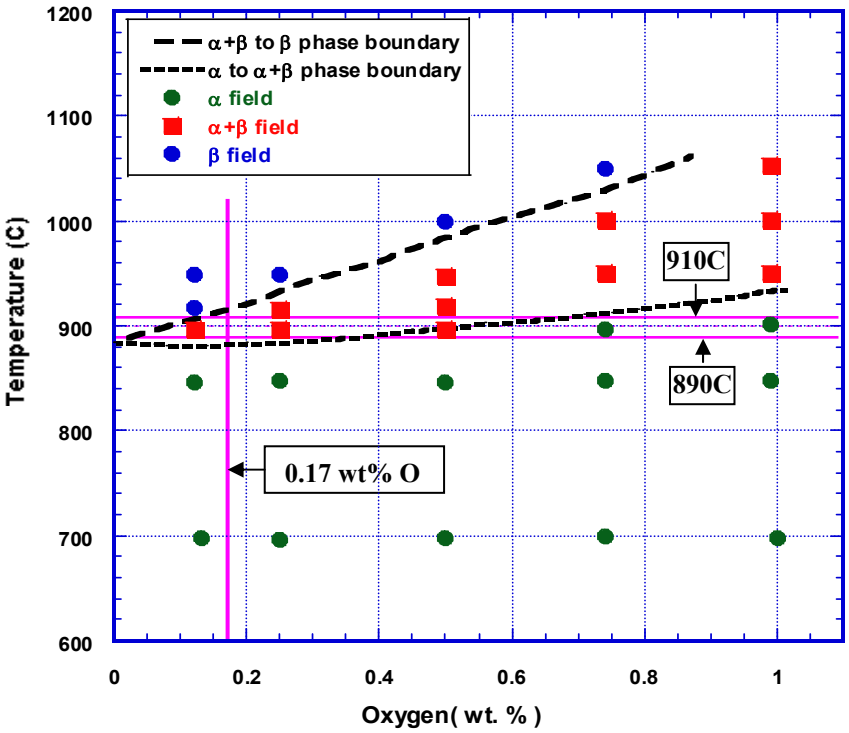

Figure 5.29 Ti-O phase diagram showing the O wt% of grade 2 CP-Ti and the limit temperatures during thermal cyclic experiments.

the sample as well as the cyclic limit temperatures are indicated. It is evident that cycling between 890 and 910 °C may not necessarily produce the complete and reversible α to β transformation as envisaged in CPCD. In fact, the limit temperatures lie in the α+β phase field. This aspect was not recognized at the beginning of experiments and in the results reported earlier in this section. This was mainly due to the practical difficulty of ensuring the precise O content in the Ti sample available commercially– O content can vary between 0.1 wt% and 0.25 wt% while meeting the Grade 2 standard, in commercial production of Ti.

To ensure that the sample undergoes complete α to β phase reversal in every cycle of the thermal treatment, new sets of experiments were designed with samples having lower O content. The nominal composition (in wt%) of the new CP-Ti grade 2 sample is 0.07 Fe, 0.12 O, 0.007 C, 0.006 N, 0.001 H and bal. Ti. The O content and the thermal cycling profile used for the new experiment are shown in Figure 5.30, superimposed in the Ti-O phase diagram. Two new sets of experiments were devised. The limit temperatures for one set of experiments were 880 and 920 ˚C while for the other set were 880 and 940 ˚C. The lower and upper limit temperatures for thermal cycling are well inside the respective α and β phase fields (Figure 5.30). The upper limit temperature in the second set of experiments was kept at 940 ˚C to determine the effect of cycle frequency, if any on growth behavior. The increase in upper limit temperature to 940 ˚C will reduce the number of thermal cycles for a given period of total exposure time, compared to that with 920 ˚C as the upper limit temperature. This is intended to

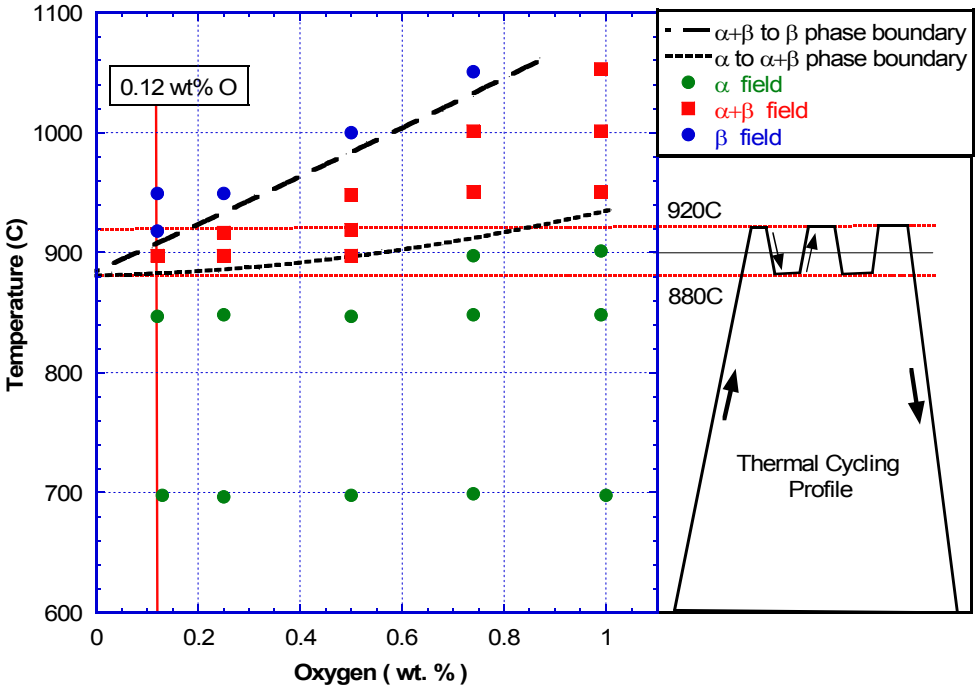

Figure 5.30 The O wt% of grade 2 CP-Ti superimposed in the Ti-O phase diagram and the limit temperatures used for new sets of thermal cyclic experiments.

investigate if there is an effect of number of thermal cycles on the coating growth behavior. A lesser number of cycles will reduce the number of times the *heat-packet* traverses through the subsurface of the material, and could possibly lead to a decrease in the coating growth kinetics. The experiments were conducted using a powder mixture similar to that used in the previous experiments. Thermal cycling was done for 2, 5, 9, 13, and 17 cycles with 880-920 ˚C limit temperatures which corresponded to total thermal exposure times of 3, 6, 12, 18 and 24 hours, respectively, and for 2, 4, 8, 14 cycles with 880-940 ˚C limit temperatures which corresponded to total time of 3, 6, 12, and 24 hours, respectively. The hold time at limit temperatures were kept as 0.5 hours for both sets of experiments.

The optical and SEM micrographs of the TiB boride layers obtained during cycling between 880-920 ˚C for 24 hours are shown in Figures 5.31 (a&b), respectively. They all show a boride layer morphology consisting of surface regions highly enriched with TiB whiskers, with the depth of penetration of TiB whiskers of about 65 μm. The coating structure consists of long TiB whiskers interdispersed with a very fine structure of precipitated TiB phases in both samples. The optical micrograph of the sample treated between 880-940 ˚C for 24 hours is shown in Figure 5.31 (c). The depth of the TiB layer in this sample is significantly less than that of 880-920 °C sample. The average depth of the TiB layer in 880-920 ˚C cycling was approximately 65 μm, whereas for 880-940 ˚C cycling it was approximately 50 μm (Table 5.7). The coating layer thicknesses obtained for other total exposure times (3, 6, 12 and 18 hours) were also relatively higher in 880-920 ˚C cyclically treated samples compared to those cycled at 880-940 ˚C. The difference in the coating thicknesses obtained between these two cycling conditions increases with

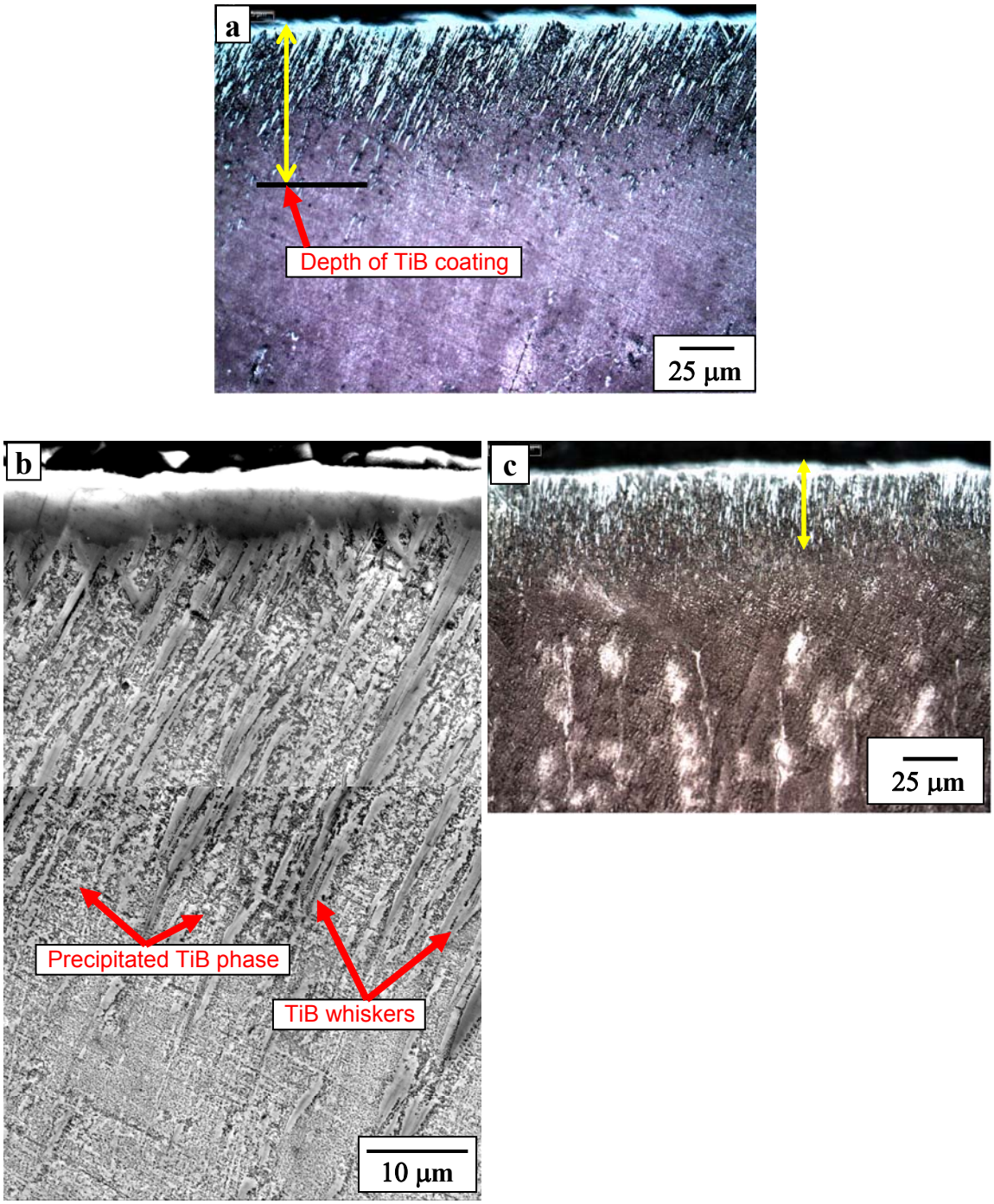

Figure 5.31 Optical **(a)** and SEM **(b)** micrographs of TiB coating produced under thermal cycling between 880-920°C for a total time of 24 hours (17 cycles). Optical **(c)** micrograph of TiB coating produced under thermal cycling between 880-940°C for 24 hours.

Table 5.7 Summary of TiB coating thicknesses obtained in cyclic thermal treatment compared with isothermal treatments.

Time* (hr)	850˚C		1050˚C		920˚C-880˚C/0.5 hr holds		940˚C-880˚C/0.5 hr holds	
	Total (µm)	SD (µm)	Total (µm)	SD (µm)	Total (µm)	SD (µm)	Total (µm)	SD (µm)
3	23	3.2	31	2.5	18	3	18	4
6	24	3.5	37	3.4	36	6	31	7
12	25	4.2	41	3.6	55	8	41	7
18	26	5.4	50	5.7	57	9		
24	28	6.3	54	5.9	66	11	48	12
27					79	15		
48	30	7.3	55	7	108	22	77	16
71	31	7.5	55	7.2	126	27	97	21

*Time in thermal cycling conditions refers to the total time of treatment, with the sample being held at 880˚C and 920˚C for 30 minutes in each cycle. This corresponds to 2, 5, 9, 13, 17, 20, 34 and 50 cycles for 3, 6, 12, 18, 24, 27, 48 and 71 hours of treatment, respectively.

increase in the total exposure time (Table 5.7). For example, for the total exposure time of 6 hours, the coating thickness obtained by 880-920 ˚C cycling was 16% higher compared to that obtained by 880-940 ˚C cycling. For total exposure of 24 hours, this difference is about 35%. It is to be realized that in 6 hours of total exposure, there are 5 cycles in 880- 920 ˚C cycling, whereas in case of 880-940 ˚C, it was 4. In other words, the difference between the number of cycles for the two cyclic conditions increases with total exposure time. For 24 hours of total exposure, the number of cycles corresponding to 880-920 ˚C and 880-940 ˚C are 17 and 14, respectively. Hence, for a given exposure time, the number of times the *heat- packet* forms and traverses to the depth of the sample are higher for 880-920 ˚C cycling than that for 880-940 ˚C cycling. In every traversal of the heat packet, more B atoms are expected to get transported to the inside of the matrix. Some of this B may add to the length of existing TiB whiskers and some may eventually precipitate as TiB phase during the cooling phase of the temperature cycle. Hence, it

seems that the relatively deeper TiB coating layer achieved in 880-920 ˚C cycling compared to 880-940 ˚C cycling can be attributed to the increased number of cycles or heat-packet traveled in the former.

The above results suggest that it might be possible to achieve even deeper TiB coating if the number of thermal cycles is increased. To explore this possibility, samples (with 0.12 wt% O) were thermally cycled between 880-920 ºC (with 0.5 hours hold at the limit temperatures) for 20, 34 and 50 cycles, corresponding to total exposure times of 27, 48 and 71 hours. A set of experiments was also performed by cycling between 880-940 ˚C for 30 and 45 cycles for the total time of 48 and 71 hours, respectively.

The optical and SEM micrographs of TiB coating layers obtained by cycling between 880-920 ˚C for 48 and 71-hours of cyclic diffusion treatment are shown in Figures 5.32 & 5.33, respectively. The figures show much deeper TiB whisker penetration into the substrate. For example, the sample treated for 48 hours shows a coating depth of about 100 μm. The 71-hour treated sample shows even higher TiB layer growth. The TiB layer penetrated in excess of 120 μm as shown in Figure 5.33. The figures also indicate relatively higher area densities of TiB whiskers and phases as compared to the sample treated for 24 hours (Figure 5.31(a)). This increase in thickness of the coating layers is attributed to the increased number of thermal cycles that resulted in more pumping and precipitation of B atoms as TiB whiskers during each thermal cycle. As observed in the case of cycling for 24 hours of total exposure, the layer thicknesses obtained by cycling the sample between 880-940 ˚C for 48 and 71 hours were also relatively less compared to that of 880-920 ˚C cycled samples. The optical micrographs for these samples are presented in Figure 5.34. It is evident from the figures

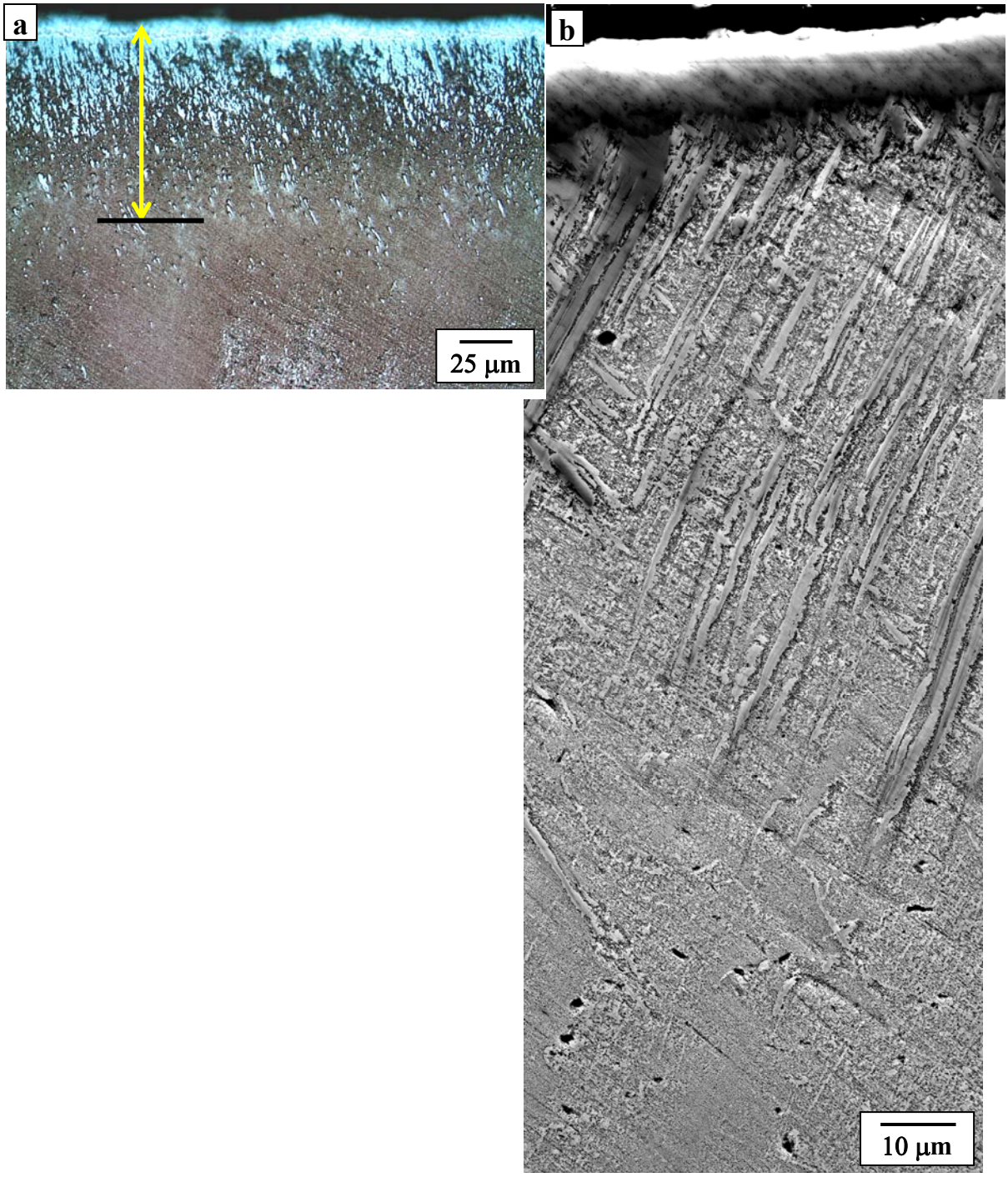

Figure 5.32 Optical **(a)** and SEM **(b)** micrographs of TiB coating produced under thermal cycling between 880-920°C for a total time of 48 hours (34 cycles). The SEM montage of micrographs in **(b)** illustrates the TiB whisker structure as well as the fine structure of the matrix consisting of irregular TiB particles precipitated out of the α matrix.

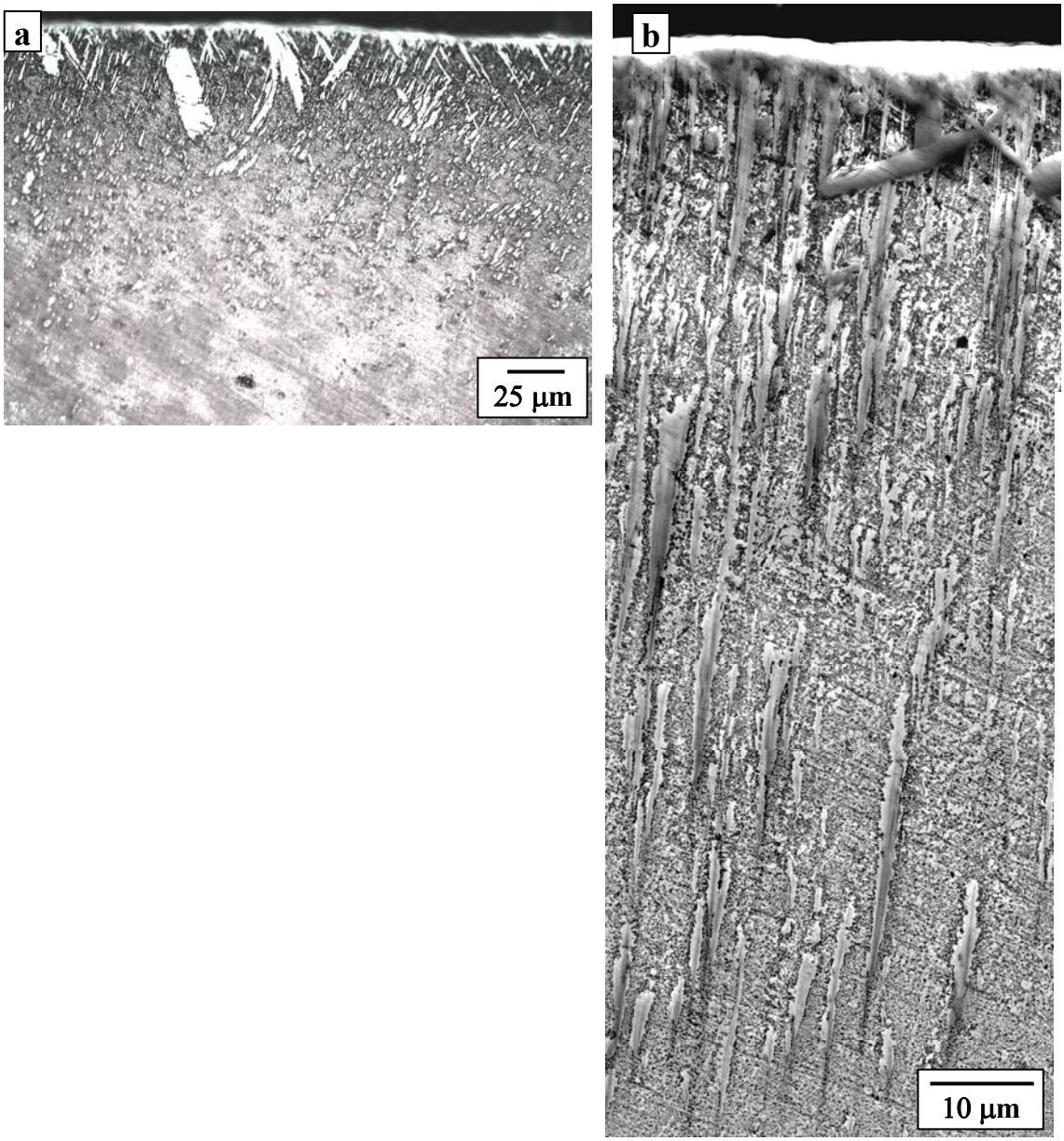

Figure 5.33 Optical **(a)** and SEM **(b)** micrographs of TiB coating produced under thermal cycling between 880-920°C for a total time of 71 hours (50 cycles). The SEM montage of micrographs in **(b)** illustrates the TiB whisker structure as well as the fine structure of the matrix consisting of irregular TiB particles precipitated out of the α matrix.

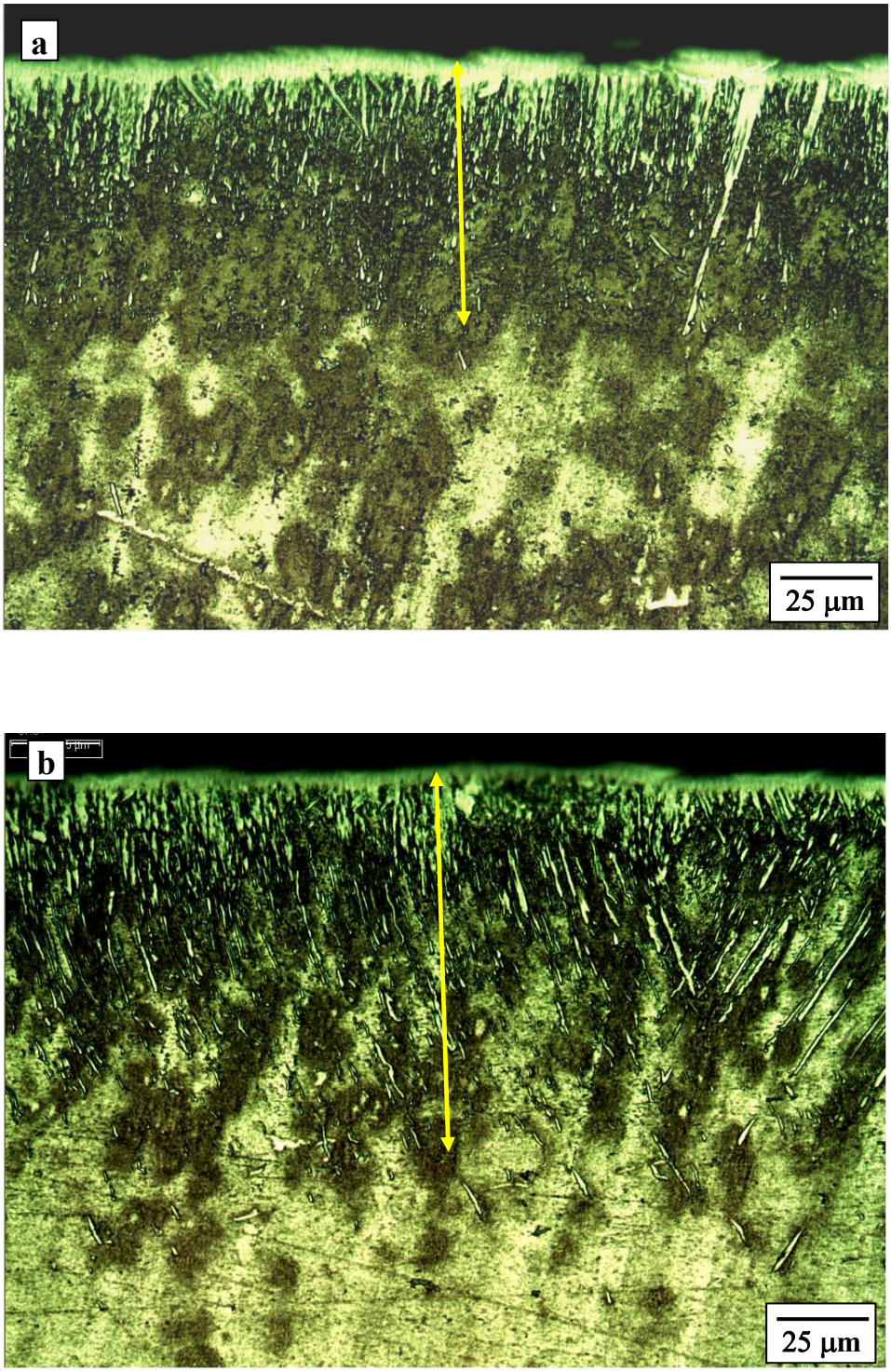

Figure 5.34 Optical micrographs of TiB coating produced under thermal cycling between 880-940°C for a total time of **(a)** 48 hours (30 cycles) and **(b)** 71 hours (45 cycles).

that the approximate depths of the coating layers are about 80 and 100 μm after 48 and 71 hours, respectively. Again, the reduced coating thicknesses are attributed to the lesser number of thermal cycles associated with the 880-940 ˚C cycling compared to that of 880-920 ˚C cycling.

The accelerated boride layer growth phenomenon is in contrast to the results obtained by isothermal treatments in completely α or β phase fields where the growth saturates after about 24 hours of total treatment time. This is illustrated in Figure 5.35, where coating thicknesses obtained for cyclic treatments were plotted as a function of total treatment time. In the same figure, the thicknesses obtained at 850 (completely α phase) and 1050 ˚C (completely β phase) isothermal B diffusion are plotted for

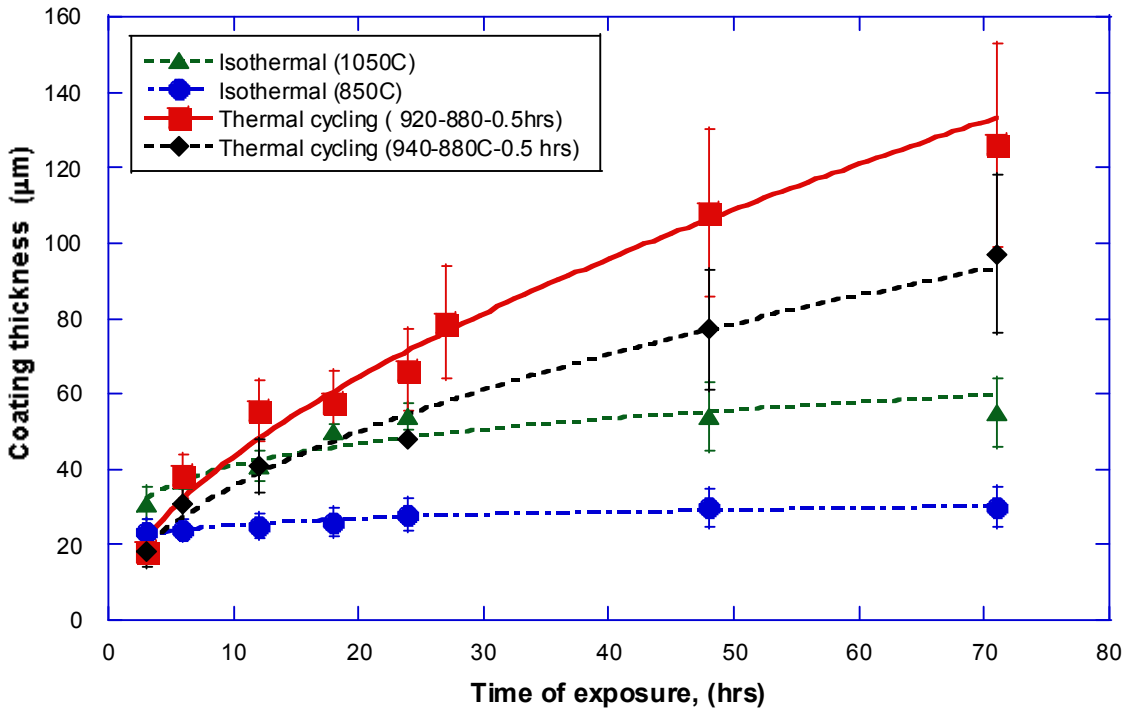

Figure 5.35 TiB coating thicknesses obtained in cyclic as well as isothermal diffusion treatments plotted as a function of total thermal exposure time.

comparison. The coating thicknesses obtained by thermal cycling are significantly higher than that obtained in isothermal treatments. During isothermal treatments at 850 and 1050 °C, the coating growth saturates clearly at 71 hours. On the other hand, cyclic treatment for 71 hours produces a coating thickness which is more than twice of that obtained after 71 hours at 1050 °C. This confirms the accelerating effect of thermal cycling on B diffusion– the pumping action induced by repeated traversing of heat-packet between surface and subsurface seem to have accelerated the boride layer growth kinetics and subsurface B supersaturation.

The Knoop hardness profile of the TiB coating, obtained by thermal cycling between 880-920 ˚C for 71 hrs, is presented in Figure 5.36. The data confirms the observations with respect to the SEM coating structure that the surface layers are hardened to a depth exceeding 100 μm in the sample cycled for 71 hours. The hardness at the surface approaches 3000 kg/mm^2 due to the presence of a thin layer of TiB_2 (~3500 kg/mm^2 monolithic hardness) at the surface. The surface layer to a depth of about 15 μm is actually a mixture of TiB whiskers and TiB_2 monolith, which explains the variation of hardness. The hardness of monolithic TiB is about 2000 kg/mm^2. The coating structure beyond about 15 μm is a mixture of TiB and Ti, with the volume fraction of TiB gradually decreasing with distance into the depth of the sample. The hardness variation in this region is consistent with the proportions of TiB/Ti phases and how they change with depth.

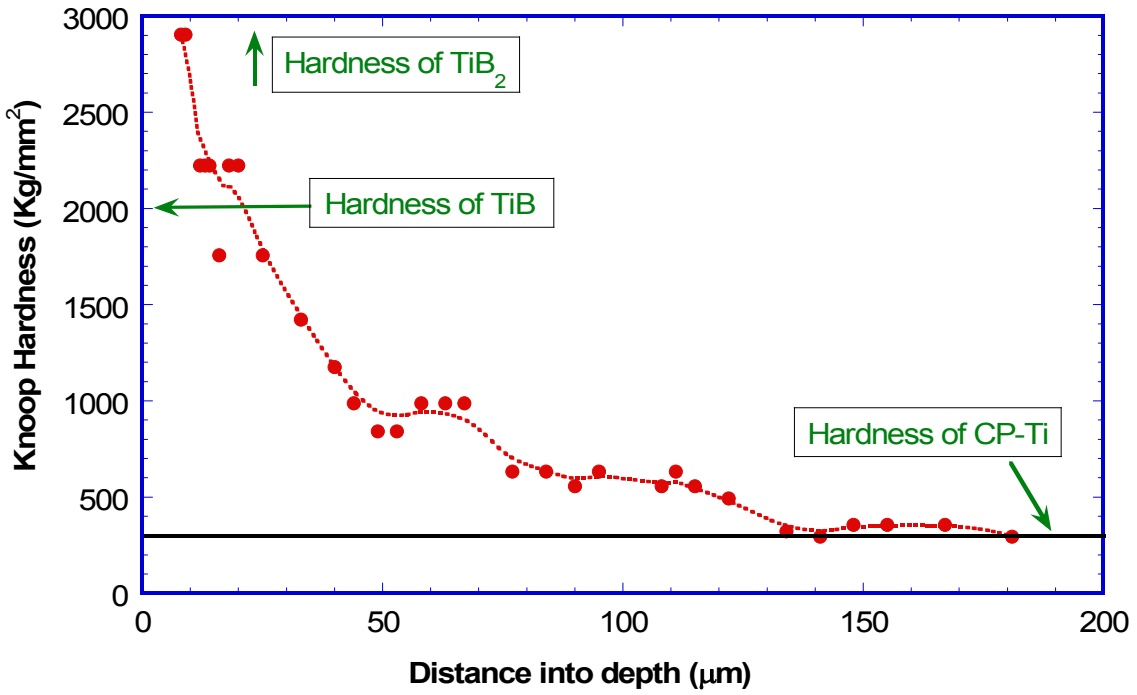

Figure 5.36 Knoop hardness profile for the TiB coating produced under thermal cycling between 880-920°C for a total time of 71 hours (50 cycles). In the figure, the hardness of Ti, (~300 kg/mm^2) TiB (~2000 kg/mm^2) and that of the TiB_2 (~3500 kg/mm^2) are indicated for reference.

CHAPTER 6

CONCLUSIONS

The theoretical model developed based on Fick's second law predicted the boride layer growth kinetics well for the diffusion experiments at temperatures away from phase transition temperature in Ti. The specific conclusions that can be drawn are:

1. The predicted layer thicknesses of TiB_2 at 850 and 1050˚C are within 10-20% of the experimental data. But the numerical predictions at 950˚C are slightly higher than the experimental trend.
2. The predicted TiB thicknesses at 850 and 950˚C are in the range of 20-25% of that of the experimental values. However, there is a large discrepancy between the predicted and experimental TiB thicknesses (by a factor of 2) at 1050˚C. This was attributed to the thickening of the TiB whiskers at higher boriding temperature such as 1050˚C.

Solid state diffusion of B at temperatures close to the phase transition temperature resulted in a significantly enhanced boride layer growth kinetics compared to that obtained at temperatures farther from it. The specific conclusions are:

3. The accelerated growth kinetics of TiB coating layer on Ti substrate near the α-β phase transition temperature leads to a significantly increased coating depth of the boride layers. For example, the boride layer thickness obtained at the phase

transition temperature (910˚C) is higher (~70 μm) than that obtained (~50 μm) at 1050˚C

4. The accelerated kinetics near the phase transition temperature is suggested to be caused by the additional, anomalous B diffusion mechanism caused by ω-like structural fluctuations in the Ti phase regions between the TiB whiskers.
5. The coating structures mainly consisted of long, high aspect ratio TiB whiskers and "precipitated TiB" particles in between the whiskers. The thicknesses of these whiskers are in the range of 200 nm to 2 μm. The precipitated TiB particles are ranging in size between approximately 100 nm to about 4 μm.
6. Using a diffusion model that considers the simultaneous diffusion of B in borides phases as well as the B diffusion in the Ti-phase, it is shown that the accelerated coating growth can be well explained by the enhancement of B-diffusion in Ti-phase near the transition temperature.
7. The predictions are subject to the uncertainties in the B diffusivity as well as the relative proportions of the TiB/Ti phases in the coating layer. Nevertheless, it has been shown that using reasonable estimates of B diffusivities near the transition temperature as well as reasonable values for phase area fractions, quite accurate results that explain the phenomenon can be obtained.
8. Knoop hardness measurements also support the existence of TiB phase hardened layer to the depth suggested by SEM micrographs and theoretical predictions.
9. Isothermal B diffusion in Ti at 850 and 1050˚C led to saturating coating thicknesses of about 30 and 50 μm after 24 hours of treatment time.

10. When isothermal B diffusion was performed near the phase transition temperature (900˚C) for 71 hours, the boride layer thickness (>100 μm) achieved was nearly double than that of 24 hours (~60 μm).

The growth kinetics of titanium boride layers under cyclic-phase-change-diffusion (CPCD) process was studied. The key conclusions are:

11. The cyclic-phase-change-diffusion process led to a much deeper (>120 μm) boride coating growth compared to that obtained by the isothermal B diffusion in α or β phase field of Ti.
12. The coating layer was highly enriched with TiB whiskers and precipitates uniformly distributed into the depth of the substrate.
13. By solving the transient heat transport profiles in the substrate due to the cyclic variations of surface temperatures, it was found that a “heat-packet” travels back and forth from the surface to the interior of the material.
14. This heat-packet appears to transport B atoms dissolved in β-Ti into interior causing increased coating depths.
15. Knoop hardness profile also suggested the presence of this hardened zone well over a depth of 120 μm.

REFERENCES

1. Designing with Titanium, (The Institute of Metals, 1986).

2. Ed: Kleefisch, E. *ASTM*, 1981.

3. Berger, M. and Larsson, M. *Surf. Eng.*, 2000, **6**, 122.

4. Liu, B.T. and Hsu, J.P. *Chem. Eng. Sci.*, 2006, **61**, 1748.

5. Williams, S., Tipper, J.L., Ingham, E., Stone, M.H. and Fisher, J. *Proceedings of the Institution of Mechanical Engineers, Part H: J. Eng. Medic.,* 2003, **217**[3], 155.

6. Griesser, Hans,J., Hartley, P.G., McArthur, S.L., McLean, K.M., Meagher, L. and Thissen, H. *Proceedings of SPIE – The International Society for Optical Engineering*, 2001, **4590**, 45.

7. Shilova, O.A., Hashkovsky, S.V. and Kuznetsova, L.A. *J. Sol-Gel Sci. Technol.*, **26**[1-3], 687.

8. Rickerby, D.S. & Matthews, A. *Advanced Surface Coating-A Handbook of Surface Engineering*, 1972, 1.

9. Barry, J. and Byrne, G. *Wear*, 2001, **247**, 152.

10. Jimenez, J.A., Frommeyer, G., Acosta, P. and Ruano, O.A. *Mater. Sci. Eng. A*, 1995, **A202**, 94.

11. Zwirn, B.P. *Carbide and Tool Journal*, 1986, **18**, 28.

12. Cockeram, B. and Rapp, R. *Mater. Sci. Forum*, 1997, **251**, 736.

13. Krupa, D. et al. *Anal. Bioanly. Chem.*, 2005, **381**, 617.

14. Suri, A.K., Nimmagadda, R. and Bunshah, R.F. *Thin Solid Films*, 1979, **64**, 191.

15. Wiedemann, K.E., Sankaran, S.N., Clark, R.K. and Wallace, T.A. *Oxidation of High Temperature Intermetallics, Proceedings of Workshop, Metal and Materials Society*, 1989, 195.

16. Elder, J.E., Thamburaj, R, and Patnaik, P.C. *Surf. Eng*., 1989, **5**, 55.

17. Baeslack, W.A., Krishnamurthy, S. and Froes, F.H. *Rapid Solidification Technology, Annual Meeting (New Orleans)*, 1986, 97.

18. Rebenne, H.E. and Bhat, D.G. *Surf. Coat. Technol.*, 1994, **63**, 1.

19. ASM Handbook, *ASM 3*, 1992, 285.

20. Tikekar, N.M. *PhD. Thesis*, 2007, University of Utah.

21. Le Claire, A.D. *Diffusion in Body-Centered Cubic Metals*, A.S.M., Metals Park, Cleveland, 1965, 3.

22. Seeger, A. *J. Less-Common Met.*, 1972, **28**, 387.

23. Murray, J.L., Liao, P.K. and Spear, K.E. *Bulletin of Alloy Phase Diagrams*, 1989, **7**[6], 550.

24. Boyer, R., Welsch, G. and Collings, E.W. *Materials Properties Handbook: Titanium Alloys*, ASM International, Materials Park, OH, 1994.

25. Molchanova, E.K. *Phase Diagrams of Titanium Alloys* (Transl. of Atlas Diagram Sostoyaniya Titanovyk Splavov), Israel Program for Scientific Translations, Jerusalem, 1965.

26. Zwicker, U. *Titan and Titanlegierungen*, Springer- Verlag, 1974.

27. Jaffee, R.I., Ogden, H.R. and Maykuth, D.J. Trans. AIME, *JOM*, 1950, **188**, 1261.

28. Hoch, M., Birla, N.C., Cole, S.A. and Gegel, H.L. *The Development of Heat-Resistant Titanium Alloys*, Tech. Report AFML-TR-73-297, Air Force Materials Lab., Dec. 1973.

29. Ageev, N.V. and Petrova, L.A. *The Theoritical Basis of the Development of the High-Strength Metastable β-Alloys of Titanium*, 809.

30. Miller, P.D. and Holladay, J.W. *Wear*, 1958/59, **2**, 133.

31. American Society for Testing and Materials, Standard G40-98b, Standard Terminology Relating to Wear and Erosion, *ASTM*, West Conshohocken, PA, USA, 1999.

32. Budinski, K.G., Budinski, M.K. and Kohler M.S. *Wear*, 2003, **255**, 489.

33. Kragelski, I.V. *Friction and Wear*, Butterworths, Washington, DC, 1985.

34. Challen, J.M. and Oxley, P.L.B. *Wear*, 1979, **53**, 229.

35. Avitzur, B., Huang, C.K. and Zhu, Y.D. *Wear*, 1984, **95**, 59.

36. Bhansali, K.J. and Miller, A.E. Role of Stacking Fault Energy on the Galling and Wear of a Cobalt Based Alloy, in: Rhee, S.K., Ruff, W.A. and Ludema, K.C. *Wear of Materials*, ASME, New York, 1981, 179.

37. Budinski, K.G. *Wear*, 1981, **74**, 93.

38. Lancaster, J.K. *Proceedings of the International Mechanical Engineering Conference on Lubrication and Wear*, 1957, 694.

39. Ohriner, K.G. and Whelan, E.P. Wear and Galling Resistance of Inter-Metallic-Strengthened Iron-Base Hard-Facing Alloys, in: Ludema, K.C. *Wear of Materials*, ASME, New York, 1985, 67.

40. Rabinowitz, E. and Foster, R.G. *Trans. ASME*, Ser. D., 1964, **86**, 306.

41. Antler, M. *Wear*, 1964, **7**, 171.

42. Yantio Njankeu, G. R., Paris, Y.J., Denape, J., Pichon, L. and Riviere, J.P. *Tribology International*, 2006, **39**, 1052.

43. Hanzel, R.W. *Met. Prog.*, 1954, 89.

44. Bloyce, A, Morton, P. H. and Bell, T. *Surface Engineering of Nonferrous Metals*, 835.

45. Alloy Phase Diagrams, *ASM Handbook*, ASM International, 1992, *3*, 299.

46. Bloyce, A. *Proc. Instn. Mech. Engrs*., 1998, **212**, 467.

47. Rebenne, H.E. and Bhat, D.G. *Surf. Coat. Technol.*, 1994, **63**, 1.

48. Zhecheva, A., Sha, W., Malinov, S. and Long, A. *Surf. Coat. Technol.*, 2005, **200**, 2192.

49. Bell, T., Bergman, W., Lanagan, J., Morton, P.H. and Staines, A.M. *Surf. Eng*., 1986, **2**, 133.

50. Song, J., Kim, S., Jeon, Y., Kim, K. and J. Kor. *Inst. Met. Mater*., 2002, **40**, 285.

51. Chen, K.C. and Jaung, G.J. *Thin Solid Films*, 1997, **303**[226].

52. Muraleedharan, T.M. and Meletis, E.I. *Thin Solid Films*, 1992, **303**[226].

53. Xue, L., Islam, M.U., Koul, A.K., Wallace, W. and Bibby, M. *Mater. Manuf. Process*., 1997, **12**, 799.

54. Coulon, P.A. *J. Mater. Process. Technol*., 1993, **38**, 247.

55. Mridha, S. and Baker, T.N. *J. Mater. Process. Technol.*, 1998, **77**, 115.

56. Weerasinghe, V.M., West, D.R.F. and de Damborenea, J. *J. Mater. Process. Technol.*, 1996, **58**[76].

57. Rie, K.T. and Lampe, T.H. *Mater. Sci. Eng.*, 1985, **69**, 473.

58. Galliano, F., Galvanetto, E., Mischler, S. and D., L. *Surf. Coat. Technol.*, 2001, **145**[121].

59. Rie, K.T., Stucky, T., Silva, R. and Leitao, E. *Surf. Coat. Technol.*, 1995, **74-75**, 973.

60. Taktak, S. and Akbulut, H. *Vacuum*, 2004, **75**, 247.

61. Borgioli, F. et al. *Mater. Lett.*, 2005, **59**, 2159.

62. Seagle, S.R. and Kessler, H. *Principles of Alloying Titanium*, 1968, 131.

63. Worner, H.W. *Surface Hardening of Titanium*, Australasian Engineer, 1950.

64. Hanzel, R.W. *Met. Prog.*, 1954, 89.

65. Machlin, E.S. and Yankee, W.R. *J. Appl. Phys*., 1954, **25**, 576.

66. Gaucher, A. and Zabinski, B. *Entropie*, 1975, **63**, 36.

67. Mushaiake, M., Asano, K., Miyamura, N. and Nagano, S. *SAE Technical Report Series*, 1991, 910428, 41.

68. Mitchell, L.E. and Botherton, P.J. *J. Instit. Metals*, 1965, 93.

69. Marshall, J., Jacobs, M.H., Armstrong, G.R. and Rickinson, B.A. in *Hot Isostatic Pressing '93* (ed. L.D.a. H.Tas), 1994, 317.

70. Alloy Phase Diagrams, *ASM Handbook*, ASM International, 1992, **3**, 324.

71. Matuschka, A.V.G. *CAV*, 1972, **9**, 93.

72. Hyder, N., Nevelos, A.B. and B, a.T.G. *J. Arthro*., 1996, **11**, 679.

73. Murakami, T., Ohtuski, N. and Higaki, H. *Proceedings of the International Tribology Conference*, Yokohama, 1995, p. 1-69 Japanese Society of Mechanical Engineers.

74. Eyre, T.S. *Wear*, 1995, **34**, 383.

75. Matuschka, A.Gf.V. *Boronizing*, 1.

76. Moissan, H. and Hebdom, C.R. *Seaneces Acad. Sci*., 1895, **120**, 174.

77. Belyaeva, G.I., Plotnikova, A.F., Stotskaya, S.N. and Chernov, Ya. B. *Termicheskaya, Obrabotka Metallov*, 1979, **10**, 40.

78. Lyakhovich, L.S., Protasevich, G.F., Voroshnin, L.G., Suprunovich, A.S. and Shabashova, N.D. *Termicheskaya, Obrabotka Metallov*, 1976, **7**, 67.

79. Newkirk, A.E. *Boron, Metallo-boron Compounds and Borasses*, 1964, 147.

80. Seagle, S.R. and Kessler, H. *Principles of Alloying Ti, ASM Battelle Memorial Institute*, Columbus, OH, 1968, **3**, 131.

81. Minkevic, A.N. *HTM 17*, 1962, **3**, 141.

82. Nicholson, J.W., Wilson, A.D. and Prosser, H.J. *Surface Coatings-1*, 1968, McGraw-Hill, New York, NY.

83. Lachtin, J.M. and Peelkina, M.A. *Metalloved. Obr. Term. Metallov*., 1961, **3**, 27.

84. Blanter, M.E. and Besedin, N.P. *Mettaloved Obr. Term. Metallov*., 1955, **3**, 27.

85. Yu, L.G., Chen, X.J., Khor, K.A. and Sundararajan, G. *Acta Mater.*, 2005, **53**, 2361.

86. Keddam, M. and Chentouf, S.M. *Appl. Surf. Sci.*, 2005, **252**, 393.

87. Ravichandran, K.S. and Aich, S. US Patent 7264682.

88. Tikekar, N.M., Ravichandran, K.S. and Sanders, A. *Scripta Mater.*, 2007, **57** [3], 273.

89. Lee, C., Sanders, A., Tikekar, N.M. and Ravichandran, K.S. *Wear*, 2008, **256**, 375.

90. ASM Handbook, *ASM 5*, 1994, 835.

91. Lundstrom, T. *Boron and Refractory Borides*., Springer-Verlag, 1997.

92. Sahay, S.S., Ravichandran, K.S. and Arti, R. *J. Mater. Res*., 1999, **14**, 4214.

93. Panda, K.B. *M.S. Thesis*, 2001, The University of Utah.

94. Panda, K.B. and Ravichandran, K.S. *Metall. Mater. Trans. A*, 2002, **34A**, 1371.

95. Panda, K.B. and Ravichandran, K.S. *Metall. Mater. Trans. A*, 2002, **34A**, 1993.

96. Hyman, M.E., McCullough, C., Vallencia, J.J., Levi, C.G. and Mehrabian, R. *Metall. Trans*., 1989, **20A**, 1847.

97. Fan, Z., Gua, Z.X. and Cantor, B. *Composites*, Part A, 1997, **28A**, 131.

98. Li, D.X., Ping, D.H., Lu, Y.X. and Ye, H.Q. *Mater. Lett.*, 1993, **16**, 322.

99. Prangnell, P.B., Reeves, A.J., Clyne, T.W. and Stobbs, W.M. *Advanced Structural Materials*, 2, (Eds T.W. Clyne and P.J. Withers) The Institute of Materials, London, 1992.

100. Schmidt, H. et al. *J. Appl. Phys.*, 2003, **93**, 907.

101. Kwangjun et al, *Metall. Mater. Trans. A*, 2000, **31**[11], 2849.

102. Badini, C., Bianco, M., Talentino, S., Guo, X.B. and Gianoglio, C. *Appl. Surf. Sci.*, 1992, **54**, 374.

103. Aich, S, and Ravichandran, K.S. *Metall. Mater. Trans. A*, 2002, **33A**, 3489.

104. Tikekar, N.M. *PhD Thesis*, University of Utah, 2007.

105. Gyulikhandanov, E.L. and Khaidorov, A.D. *Met. Sci. Heat Treat.*, 2001, **43**, 228.

106. Nesbitt, J.A. and Heckel, R.W. *Oxid. Met.*, 1988, **29**, 75.

107. Rolinski, E. *Surf. Eng.*, 1986, **2**[1], 35.

108. Palty, A.E., Margolin, H. and Nielsen, J. *Trans. ASM*, 1954, **46**, 312.

109. Haanappel, V.A.C., Glatz, W, Clemens, H. and Stroosnijder, M.F. *Mater. High Temp.*, 1997, **14**[1], 19.

110. Rao, B.V.N. and Thomas, G. *Metall. Trans. A*., 1980, **11A**, 441.

111. Rao, B.V.N. and Thomas, G. *Mater. Sci. Eng*., 1975, **20**, 195.

112. Thomas, G., Kim, J.K., Manojlovic, D. and Milovic, R. *Proc. Micro. and Properties of HSLA Steels*, de Ardo, A.J. ed., TMS-AIME, Warrendale, PA, 1988, 399.

113. Nakazawa, K, Kawabe, Y. and Muneki, S. *Mater. Sci. Eng.*, 1978, **33**, 49.

114. Ramesh, R, Kim, N.J. and Thomas, G. *Metall. Trans. A*, 1990, **21A**, 683.

115. Wang, J.N., Yang, Jie, Xia, Q. and Wang, Y. *Mater. Sci. Eng.*, 2002, **A329-331**, 118.

116. Sahay, S.S., Malhotra, C.P. and Kolkhede, A.M. *Acta Mater*., 2003, **51**, 339.

117. Schuh, C.A. and Dunand, D.C. *Acta Mater*., 2002, **50**, 1349.

118. Geng, H., He, S. and Lei, T. *Metall. Trans*., 1997, **28A**, 1809.

119. Sista, V., Nash, P. and Sahay, S.S. *J. Mater. Sci*., 2007, **42**, 9112.

120. Hausner, H.H. *Proc. Int. Symposium on Reactivity of Solids*, Gothenburg, Part 2, 1994, 1051.

121. Choi, H.S., Yoon, Y.K. and Park, W.R. *Int. J. Powder Met*., 1973, **9**, 23.

122. Kohara, S. *Metall. Trans. A*, 1976, **7A**, 1239.

123. Misra, P.S. and Upadhyaya, G.S. *Powder Metall.*, 1976, **8**[4], 165.

124. Seeger, A., Wieland, O., Carstanjen, H.D., Frank, W. and Neumann, M. *Proceedings of the International Conference on Solid-Solid Phase Transformations (JIMIC-3)*, 1991, 449.

125. Askill, J. and Gibbs, G.B. *Phys. Stat. Sol*., 1965, **11**, 557.

126. Sanchez, J.M. and De Fontaine, D. *Acta Metall*. 1978, **26**, 1083.

127. Walsoe de Reca, N.E. and Libanati, C.M. *Acta Metall*., 1968, **16**, 1297.

128. Rothman, S.J., Lloyd, L.T., Weil, R. and Harkness, A.L. *Trans. Metall. Soc. AIME*, 1960, **218**, 605.

129. Dupuy, M. and Calais, D. *Trans. Metall. Soc. AIME*, 1968, **242**, 1679.

130. Dariel, M.P., Dayan, R. and Languille, A. *Phys. Rev. (B)*, 1971, **4**, 4348.

131. Fromont, M.A., Languille, A. and Calais, D. *J. Phys. Chem. Solids*, 1974, **35**, 1367.

132. Dariel, M.P. *Phil. Mag*., 1973, **28**, 915.

133. Murdock, J.F. and Lundy, T.S. *Acta Metall*., 1964, **12**, 1033.

134. Federer, J.I. and Lundy, T.S. *Trans. Metall. Soc. AIME*, 1963, **227**, 592.

135. Kidson, G.V. *Diffusion in Body-Centered Cubic Metals*, A.S.M., Metals Park, Cleveland, 1965, 329.

136. De Fontaine, D. and Buck, O. *Phil. Mag*., 1973, **27**, 967.

137. Sass, L.A. *J. Less-Common Met.*, 1972, **28**, 157.

138. Jamieson, J.C. *Science*, 1963, **140**, 72.

139. De Fontaine, D., Paton, N.E. and Williams, J.C. *Acta Metall*., 1971, **19**, 1153.

140. Moss, S.C., Keating, D.T. and Axe, J.D. *Proc. Conf. on Phase Transitions and Their Applications in Materials Science*, University Park, Pennsylvania, Pergamon Press, 1973, 179.

141. Sanchez, J.M. and De Fontaine, D. *Phys. Rev. Lett.*, 1975, **35**, 227.

142. Kikuchi, R. *Phys. Rev*., 1951, **81**, 988.

143. Lampman, S. *ASM Handbook, Properties and selection: Nonferrous Alloys and Special-purpose Materials*, 1995, **2**, 594.

144. Budinsky, K.G. *Wear*, 1991, **151**, 203.

145. Metin, E. and Inal, O.T. *Metall. Trans. A.,* 1989, ***20A***, 1819.

146. Boettcher, C. *Surf. Eng. (UK)*, 2000, **16**, 148.

147. Poggie, R.A. and Kovacs, P. *Mater. Manuf. Processes*, 1996, **11**, 185.

148. Bokshtein, S.Z., Kishkin, S.T. and Osvenskii, V.B. *Metallovedenie I Term*., *Obrabokta Metallov*, 1960, 21.

149. Araki, H., Yamane, T., Minamino, Y., Saji, S., Hana, Y. and Jung, S.B. *Metall. & Mat. Trans. A*, 1994, **25A**, 874.

150. Jin, S., Morris, J.W. and Zackay, V.F. *Metall. Trans*., 1975, **6A**, 141.

151. Crank, J. *The Mathematics of Diffusion*, Clarendon, Oxford, 1975.

152. Jost, W. *Diffusion in Solids, Liquids, Gases*, Academic Press Inc., New York, 1960, 69.

153. Munro, R.G. *J. Res. Natl. Inst. Stand. Technol*., 2000, **105**[5], 709.

154. Madtha, S., Lee, C. and Chandran, R. *J. Am. Ceram. Soc*., 2008, **91**[4], 1319.

155. Nakajima, H. and Koiwa, M. *ISIJ International*, 1991, **31**[8], 757.

156. Kohler, U. and Herzig, CH. *Phys. Stat. Sol. (b)*, 1987, **144**, 243.

157. Bokshteyn, S.Z., Zyulina, N.P. and Markovich, O.V. *Fiz, Metal. Metalloved*., 1989, **68**[1], 104.

158. Bokshteyn, S.Z., Kishkin, S.T., Moroz, L.M. and Chaplygina, V.S. *Academy of Science of the Ukrainian SSR*, 1965, 59.

159. Shenkman, A.L. *Transient Analysis of Electric Power Circuits Handbook*, Springer, 2005, 259.

160. Carslaw, H.S. and Jaeger, J.C. *Conduction of Heat in Solids*, Oxford Science Publishers, Oxford, UK, 1959, 68.